

KAAREL LUMISTE

Phosphogenesis and REE+Y diagenesis
of Recent and Paleozoic phosphorites



DISSERTATIONES GEOLOGICAE UNIVERSITATIS TARTUENSIS

49

KAAREL LUMISTE

Phosphogenesis and REE+Y diagenesis
of Recent and Paleozoic phosphorites



UNIVERSITY OF TARTU
Press

Department of Geology, Institute of Ecology and Earth Sciences, Faculty of Science and Technology, University of Tartu, Estonia.

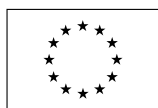
This dissertation is accepted for the commencement of the degree of Doctor of Philosophy in Geology at the University of Tartu on the 26th of August 2021 by the Scientific Council of the Institute of Ecology and Earth Sciences, University of Tartu.

Supervisors: Aivo Lepland, Norwegian Geological Survey, Department of Geology, University of Tartu, Estonia
Liisa Lang, Estonian Department of Geology, University of Tartu, Estonia

Opponent: prof. Graham Shields-Zhou, University College London, United Kingdom

This thesis will be defended at the University of Tartu, Estonia, Chemicum (Ravila 14A), room 1019, on the 12th of November 2021 at 12:15.

Publication of this thesis was granted by the Institute of Ecology and Earth Sciences, University of Tartu and by the Doctoral School of Earth Sciences and Ecology created under the auspices of the European Social Fund.



European Union
European Social Fund



Investing
in your future

ISSN 1406-2658

ISBN 978-9949-03-727-8 (print)

ISBN 978-9949-03-728-5 (pdf)

Copyright: Kaarel Lumiste, 2021

University of Tartu Press

www.tyk.ee

CONTENTS

LIST OF ORIGINAL PUBLICATIONS	6
1. INTRODUCTION.....	7
2. PHOSPHOGENESIS	9
3. REE+Y BEHAVIOUR IN MARINE AND PORE WATER SYSTEMS.	11
4. GEOLOGICAL SETTINGS	13
4.1. Cenozoic phosphorites of the Namibian Shelf	13
4.2. Early Paleozoic shelly phosphorites of the Baltica paleocontinent ...	15
5. MATERIAL AND METHODS	17
6. PHOSPHOGENESIS AND REE+Y UPTAKE IN RECENT NAMIBIAN PHOSPHORITE	21
6.1. Apatite petrography	21
6.2. Major and minor elements.....	27
6.3. Stable isotopes	34
6.4. (Bio)geochemical constraints of phosphogenesis on the Namibian shelf.....	36
6.5. Diagenetic uptake of REE+Y and other trace metals in apatite	40
7. REE+Y DISTRIBUTION IN EARLY PALEOZOIC SHELLY PHOSPHORITES	45
7.1. Petrography.....	45
7.2. REE+Y concentrations and distribution in phosphatic shells.....	47
7.3. REE+Y uptake and variability in Estonian shelly phosphorite	52
8. CONCLUSIONS.....	56
REFERENCES.....	58
SUMMARY IN ESTONIAN	70
ACKNOWLEDGEMENTS	74
PUBLICATIONS	75
CURRICULUM VITAE	170
ELULOOKIRJELDUS.....	171

LIST OF ORIGINAL PUBLICATIONS

This thesis is based on the following published papers, which are referred to in the text by Roman numerals. The papers are reprinted with the kind permission of the publishers.

- I** Mänd, K., Kirsimäe, K., Lepland, A., Crosby, C.H., Bailey, J. V., Konhauser, K.O., Wirth, R., Schreiber, A., **Lumiste, K.**, 2018. Authigenesis of biomorphic apatite particles from Benguela upwelling zone sediments off Namibia: The role of organic matter in sedimentary apatite nucleation and growth. *Geobiology* 16, 640–658. <https://doi.org/10.1111/gbi.12309>
- II** **Lumiste, K.**, Mänd, K., Kirsimäe, K., Bailey, J., Paiste, P., Lang, L., Lepland, A., 2019. REE + Y uptake and diagenesis in Recent sedimentary apatites. *Chemical Geology*, 525, 268–281. <https://doi.org/10.1016/j.chemgeo.2019.07.034>
- III** **Lumiste, K.**, Mänd, K., Bailey, J., Stüeken, E.E., Paiste, K., Lang, L., Sepp, H., Lepland, A., Kirsimäe, K., 2021b. Constraining the conditions of phosphogenesis: Stable isotope and trace element systematics of Recent Namibian phosphatic sediments. *Geochimica et Cosmochimica Acta* 302, 141–159. <https://doi.org/10.1016/j.gca.2021.03.022>
- IV** **Lumiste, K.**, Lang, L., Paiste, P., Lepland, A., Kirsimäe, K., 2021a. Heterogeneous REE+Y distribution in Early Paleozoic shelly phosphorites: implications for enrichment mechanisms. Manuscript submitted to *Chemical Geology*.

Author's contribution:

- Paper I:** The author was responsible for microscopy and mineralogical-geochemical analysis, data collection, and contributed to the writing and editing of the manuscript.
- Paper II:** The author was responsible for planning original research, data collection, analysis, and visualization, as well as the writing of the manuscript.
- Paper III:** The author was responsible for planning original research, microscopy analysis and stable isotope data collection, data visualization, analysis and the writing of the manuscript.
- Paper IV:** The author was responsible for planning original research, performed the data collection and interpretation of analytical results, synthesis of data and the writing of the manuscript.

1. INTRODUCTION

Phosphorus (P) is an essential element for all life on Earth as well as the key limiting nutrient on geological timescales (Tyrrell T., 1999). Although the behaviour of P in Earth systems has been extensively studied, significant aspects of the global P-cycle remain poorly constrained. One of the least understood aspects of the P-cycle is phosphogenesis—the formation of solid phosphate phases. Phosphogenesis, representing the ultimate sink for marine phosphorus (Ruttenberg and Berner, 1993), is a complex phenomenon resulting from the harmonic interplay between a variety of different physical, biological and chemical factors (e.g., Arning et al., 2009a; Brock and Schulz-Vogt, 2011; Föllmi, K.B., 1996; Goldhammer et al., 2010; Krajewski, 1994; Schulz and Schulz, 2005).

The average P concentration in sedimentary rocks is only around 0.09 wt%, whereas in P-rich sedimentary rocks—phosphorites—the concentration of P_2O_5 is typically about 10–20 wt% (Filippelli, G., 2011). However, there is no universally accepted P_2O_5 threshold value for phosphorite rock. Different authors have arbitrarily defined phosphorite as a rock or a sediment containing at least 5 wt% (Gimmelfarb et al., 1959), 18 wt% (Jarvis et al., 1994), or 20 wt% (Filippelli, G., 2011) of P_2O_5 . Rocks/sediments containing a significant degree of P_2O_5 , but not exceeding the threshold, are commonly referred to as phosphatic sediments/rocks. In this thesis, phosphorites are defined as sediments/rocks containing at least 9 wt% P_2O_5 .

The main phosphate-containing phase in sedimentary phosphorites is apatite—a calcium phosphate mineral with the generalized formula of $Ca_5(PO_4)_3(OH,F,Cl)$. Due to its complex crystal structure (e.g., Hughes and Rakovan, 2002), apatite is susceptible to a wide variety of substitutions (e.g., Na, Mn, Sr, Ba, Pb, Cd, REE, Y, AsO_4^{3-} , SO_4^{2-} , CO_3^{2-} , SiO_4^{4-} , VO_4^{3-}) at either the Ca, PO_4 or F site (Pan and Fleet, 2002). While most of these substitutions occur at trace levels (e.g. Mn, REE, Y, Cd), some substitutions may reach concentrations in the range of ~10 wt% (e.g., CO_3^{2-}) (Hughes and Rakovan, 2002), having important geochemical and industrial implications.

Apatite phases in sedimentary phosphorites can be broadly divided into two types: biogenic and authigenic apatite. Biogenic apatite comprises phosphatic brachiopods (e.g., Heinsalu et al., 1994; Lécuyer et al., 2004), bones and teeth of vertebrates, coprolites and other skeletal remains of apatite-secreting animals (e.g., Garnit et al., 2017; Lécuyer et al., 2004). Authigenic apatite, on the other hand, forms as a result of a variety of biological, geological and sedimentological processes (e.g., Föllmi, K.B., 1996; Schulz and Schulz, 2005). Authigenic apatite is found in sediments as either discrete grains of varying dimensions (i.e., nodules, concretions, clast, pellets) or as phosphatic laminae and crusts (e.g., Arning et al., 2009b; Compton and Bergh, 2016; Pufahl and Groat, 2017).

Phosphorus is used for producing fertilizers and food additives, as well as a variety of other products. Global demand for phosphorus is continuously

increasing and the depletion of current reserves is projected to occur in the next 100 to 300 years (Pufahl and Groat, 2017). The importance of these deposits is compounded by the fact that sedimentary apatite can contain significant quantities of Rare Earth Elements (REE), which have a wide range of industrial applications, especially in emerging green energy technologies (Humphries, M., 2011; Long et al., 2012). The fast-paced increase in the demand for REE (~8% per annum; Long et al., 2012) has triggered the exploration of unconventional REE deposits, such as sedimentary phosphorites (Emsbo et al., 2015).

Although numerous studies have been dedicated to the understanding of phosphogenesis (e.g., Álvaro et al., 2016; Berndmeyer et al., 2012; Birski et al., 2019; Bradbury et al., 2015; Daesslé and Carriquiry, 2008; Föllmi, K.B., 1996; Garnit et al., 2017; Jahnke et al., 1983; Joosu et al., 2016, 2015; Lepland et al., 2014; Pufahl and Groat, 2017; Schöllhorn et al., 2020; Wallin, 1989) and the REE+Y uptake in sedimentary phosphorites (e.g., Auer et al., 2017; Emsbo et al., 2015; Joosu et al., 2015; McArthur and Walsh, 1984; Shields and Stille, 2001; Shields and Webb, 2004; Watkins et al., 1995; Zhu et al., 2014), significant gaps remain in the knowledge regarding both these processes.

The overall goal of this thesis is to decipher the environmental conditions during phosphogenesis and the diagenetic evolution of sedimentary phosphorites.

The specific aims of this thesis are (I) to constrain the (bio-)geochemical conditions necessary for the formation of sedimentary apatite and (II) to study the effects of early and late-stage diagenesis on the REE+Y composition of Recent and Palaeozoic authigenic and biogenic apatites.

This thesis forwards hypotheses that, (I) the formation of sedimentary apatite in the pore space near the seawater-sediment interface is biologically induced by the fluctuating redox conditions in the overlying water column; and (II) the uptake of REE+Y occurs during post-depositional absorption-desorption processes, with apatite REE+Y signals reflecting the chemical evolution of pore water.

2. PHOSPHOGENESIS

The earliest known phosphatic sediment deposits are from the Paleoproterozoic following the Great Oxygenation Event (Lepland et al., 2014; Soares et al., 2019), but the first large-scale phosphogenesis and the formation of economically significant phosphorites coincides with the Neoproterozoic Oxygenation Event. Their formation was likely related to evolutionary adaptations (Shields et al., 2000) and enhanced oxidative weathering (Pufahl and Groat, 2017). Throughout the Phanerozoic, the formation of phosphorites concurs with periods of dynamic climate and enhanced weathering (Compton et al., 2002; Compton and Bergh, 2016; Föllmi, K.B., 1996; Föllmi et al., 2019; Pufahl and Groat, 2017; Schöllhorn et al., 2020; Shields et al., 2000). Modern phosphogenesis occurs on the continental margins of Namibia (Baturin, G., 2000; Bremner and Rogers, 1990; Compton et al., 2002; Compton and Bergh, 2016), Peru and Chile (Arning et al., 2009b, 2009a; Burnett, W., 1977), Baja California (Jahnke et al., 1983), the Arabian Sea (Schenau et al., 2000) and Australia (O'Brien and Veeh, 1980).

Except for Western Australia, all modern major sites of phosphogenesis occur on the continental shelves influenced by upwelling. In these settings, the upwelling of nutrient-rich deep waters to the shelf fuels high primary productivity (Carr M.-E., 2001) and, in turn, high rates of carbon loading (Inthorn et al., 2006). The subsequent remineralization of abundant organic matter requires high amounts of oxidants (electron acceptors), leading to their depletion and the development of sharp and shallow redoxclines. However, the redox conditions of shallow sediments on upwelling shelves are not temporally stable, but rather fluctuate on ~ 100 year (Algeo and Li, 2020; Hoetzel et al., 2017) and diurnal scales (Bailey and Chapman, 1991). These dynamic settings, where redox conditions fluctuate from oxic to sulfidic, provide habitat for large sulphur bacteria (LSB), such as *Thiomargarita namibiensis* (Schulz et al., 1999) as well as other polyphosphate-metabolizing organisms (Zoss et al., 2018). LSB prosper under these hectic redox conditions, due to a peculiar auxiliary metabolic pathway. Large sulphur bacteria primarily gain energy from oxidizing pore water sulphides, using oxygen or nitrate as electron acceptors (Schulz and Schulz, 2005). However, due to the limited and fluctuating electron acceptor supply, LSB also accumulate and store nitrate and polyphosphate intracellularly, metabolizing these compounds under reducing conditions. This process has been suggested to boost pore water phosphate concentrations to levels necessary for Ca-phosphate precipitation (Brock and Schulz-Vogt, 2011; Schulz and Schulz, 2005).

Alternatively, Fe-Mn oxyhydroxides have been suggested to mediate the phosphate preconcentration (Noffke et al., 2012). Principally, the Fe-Mn oxyhydroxide shuttle operates by adsorbing phosphate from seawater during the descent of colloidal particles through the water column and releasing the adsorbed P-species into the pore space during their reductive dissolution. Under oscillating redox-conditions, Fe-Mn oxyhydroxides are capable of modifying interstitial phosphate concentrations (Küster-Heins et al., 2010; Noffke et al., 2012). Both

the “bacterial P-pump” and the Fe-Mn shuttle are dependent on dynamic and fluctuating redox conditions. However, the Namibian shelf—one of the main loci of modern phosphogenesis—is somewhat depleted of Fe and strongly depleted of Mn (Borchers et al., 2005), whereas abundant bacterial mats of LSB are found in large amounts on the shelf (Brüchert et al., 2006). Hence, it is unlikely that the Fe-Mn shuttle plays a primary role in controlling the delivery of phosphate to the sediment and phosphogenesis. Instead, LSB seem to control the formation of phosphorites at the Namibian shelf.

3. REE+Y BEHAVIOUR IN MARINE AND PORE WATER SYSTEMS

REE are a group of 15 elements from La to Lu with remarkably similar chemical behaviour under low temperature surface conditions (e.g., in marine and pore water systems). Due to identical charge and similar ionic radii to Ho, Y is often grouped together with REE (collectively referred to as REE+Y). Based on the differences in atomic mass, REE are further divided into light REE (LREE, La-Nd), middle REE (MREE; Sm-Dy) and heavy REE (HREE; Ho-Lu) (Tostevin et al., 2016). The REE+Y are all trivalent, with the exception of Ce⁴⁺ occurring under oxic (de Baar et al., 1985) and Eu²⁺ under high-temperature/reducing conditions (Bau et al., 2010; Michard, 1989). Under oxic conditions, Ce³⁺ is oxidized to the less mobile Ce⁴⁺ and the tetravalent form is scavenged by Fe-Mn oxyhydroxides, resulting in Ce-depleted seawater (Byrne and Sholkovitz, 1996). Similarly, Fe-Mn oxyhydroxides scavenge Ho more efficiently than Y, resulting in relative Y enrichment in seawater (Bau and Dulski, 1996; Minami et al., 1998). The gradual filling of 4f orbital leads to a small-scale increase in the stability of REE+Y complexes across the REE+Y series, resulting in HREE enrichment in seawater (de Baar et al., 2018, 1991). In addition, elements with empty and half-filled 4f orbitals (La and Gd respectively) are more stable in marine settings, being therefore able to become anomalously enriched (Bau, 1999; Masuda and Ikeuchi, 1979). Collectively, these processes lead to marine seawater REE+Y patterns (e.g., Alibo and Nozaki, 1999; de Baar et al., 2018, 1991, 1985; Deng et al., 2017) with characteristic HREE enrichment (LREE depletion), negative Ce-anomalies (de Baar et al., 1985), Y enrichment (Nozaki et al., 1997) and faint positive La and Gd anomalies (Bau, M., 1999).

The input of REE+Y to marine systems is primarily controlled by riverine (Martin et al., 1976; Sholkovitz et al., 1999) and eolian transport (Chen et al., 2015), as well as the mixing of groundwater and seawater (Johannesson et al., 2017, 2011). The distribution of trivalent REE+Y in the water column follows a nutrient-like profile, meaning that trivalent REE+Y concentrations increase in unison with water depth. Particle reactive Fe-Mn oxyhydroxides, organic matter (Abbott et al., 2015; Haley et al., 2004) and clay minerals (Abbott et al., 2019) play an important role in the REE+Y cycle by readily adsorbing dissolved REE+Y from the water column and releasing them into pore water during diagenesis. Because these processes are contemporaneous, REE+Y concentrations peak at or slightly below the sediment-seawater interface (SWI), decreasing further down the sediment column (Abbott et al., 2019, 2015; Deng et al., 2017; Haley et al., 2004). At greater sediment depths, REE+Y concentrations decrease rapidly (e.g., Soyol-Erdene and Huh, 2013) due to (I) the depletion of REE+Y carrying particles, (II) the uptake by authigenic minerals and (III) discharge to the water column (Abbott et al., 2019, 2015).

Large-scale redistribution of REE+Y during late-stage diagenesis and low-grade metamorphism rarely occurs (Chakrabarti et al., 2007; Ohr et al., 1994),

unless host phases are altered/mobilized by hydrothermal fluids (e.g., Chetty and Gutzmer, 2012). The relative stability of REE+Y has led to the extensive usage of these elements and their ratios as paleoenvironmental tracers (e.g., Emsbo et al., 2015; Felitsyn et al., 1998; Lécuyer et al., 2004a, 1998; Sturesson et al., 2005; Wright et al., 1987; Zhao et al., 2013).

An important sink for REE+Y in marine settings is its removal by authigenic minerals (Abbott et al., 2019). One such early-diagenetic mineral that readily takes up REE+Y is apatite (Chen et al., 2015). REE+Y can occur at different locations in the apatite structures, either through (I) a coupled substitution of REE+Y ion and a monovalent ion (e.g., Na⁺), replacing 2 Ca²⁺ ions, or (II) REE³⁺ and Si⁴⁺ replacing Ca²⁺ and P⁵⁺ (Jarvis et al., 1994; Pan and Fleet, 2002). REE uptake can result in concentrations as high as ~2 wt% in some sedimentary apatites (Emsbo et al., 2015). REE+Y concentrations of apatite have been extensively used in paleoredox studies (e.g., Emsbo et al., 2015; Felitsyn et al., 1998; Lécuyer et al., 2004; Reynard et al., 1999; Shields and Webb, 2004; Sturesson et al., 2005; Wright et al., 1987; Zhao et al., 2013). However, biogenic apatite (e.g., shark bones, brachiopod shells) precipitates as a metastable hydroxyapatite and readily recrystallizes to carbonate-fluorapatite (CFAp; Trueman, 2013), which is a thermodynamically stable apatite phase in seawater under early diagenetic pore water conditions (Jahnke, 1984). This transformation is accompanied by the overprinting of primary REE+Y signals, making biogenic apatite an ambiguous carrier of paleoredox information (Chen et al., 2015; Herwartz et al., 2013; Trotter et al., 2016; Zhao et al., 2013). Dissimilarly, authigenic apatite is directly precipitated as stable CFAp (Knudsen and Gunter, 2002) and should *a priori* carry information regarding its formational environment.

4. GEOLOGICAL SETTINGS

4.1. Cenozoic phosphorites of the Namibian Shelf

The Namibian Shelf was formed after the breakup of Gondwana. It is characterized as an unusually deep (Compton and Bergh, 2016) and broad (50 to 150 km; Brüchert et al., 2006; Compton and Bergh, 2016) passive continental margin. The basement of the shelf comprises Precambrian rocks, overlain by Jurassic to Cenozoic sedimentary rocks, which are truncated by an erosional surface (Compton and Bergh, 2016). The patchy sediment cover of the shelf, while poorly documented, varies from Pleistocene to Recent in age (Compton and Bergh, 2016). The Kunene and Orange rivers are the only perennial rivers that carry sediments to the shelf. A significant portion of terrigenous sediments is delivered to the shelf by means of eolian transport (Eckardt and Kuring, 2005).

The Namibian shelf is influenced by the Benguela Upwelling System (BUS), representing one of the strongest upwelling currents in the world. The rising nutrient-rich deep ocean waters fuel the world's most biologically productive eastern boundary marine ecosystem (Carr, M.-E., 2001), which is associated with intense organic carbon burial (Inthorn et al., 2006). Combined with a modest detrital input (Eckardt and Kuring, 2005), the prolific algal production has led to the accumulation of an up to 15 m thick layer of Pleistocene to modern diatomaceous mud near Walvis Bay (Baturin, G., 2000). This mud grades into less diatomaceous organic-rich mud towards the south. The nearshore shelf sediments consist of sand and gravel, while the outer shelf hosts carbonates (Fig. 1; Compton and Bergh, 2016). The remineralization of the high flux of sinking organic matter in the coastal upwelling system off Namibia creates fluctuating shelf anoxia and sulfidic water column conditions, titrating the limited Fe input and further reducing the importance of Fe-Mn oxyhydroxides in P cycling (Brüchert et al., 2006). Organic matter also delivers P to the sediments—a primary factor enabling the formation of phosphorites on the inner shelf—while the fluctuating redox conditions facilitate phosphogenic polyphosphate metabolism.

Principally, two distinctive types of sedimentary apatitic grains can be distinguished on the Namibian shelf: (I) authigenic, concretionary apatitic grains occurring in the pore space of sediments of the inner shelf and (II) reworked and redeposited, pelletal apatitic grains on the middle and outer shelf (Compton and Bergh, 2016). The first appearance of sedimentary apatite enrichments on the Namibian Shelf coincides with the initiation of BUS, following the Late Miocene global cooling phase (Hoetzel et al., 2017). Based on strontium isotope stratigraphy, the oldest redeposited pelletal phosphorites are roughly 5.8 Ma old, with the most intense episodes of phosphogenesis having taken place during Pliocene and Pleistocene (Compton and Bergh, 2016), and the youngest concretionary apatites being late Pleistocene to early Holocene in age (Baturin, G., 2000). During reworking, apatitic concretions are rounded to form pelletal apatitic grains. Variable grain size and intragranular zonation has been described in some

of the pelletal grains suggesting multiple episodes of phosphogenesis (Baturin, G., 2000). Pelletal and concretionary apatitic grains make up 80–90% of phosphorite deposits, while the rest is made up of fish remains, mollusc molds, phosphatized calcareous fossils and recent phosphatic brachiopods (Baturin, G., 2000; Compton and Bergh, 2016).

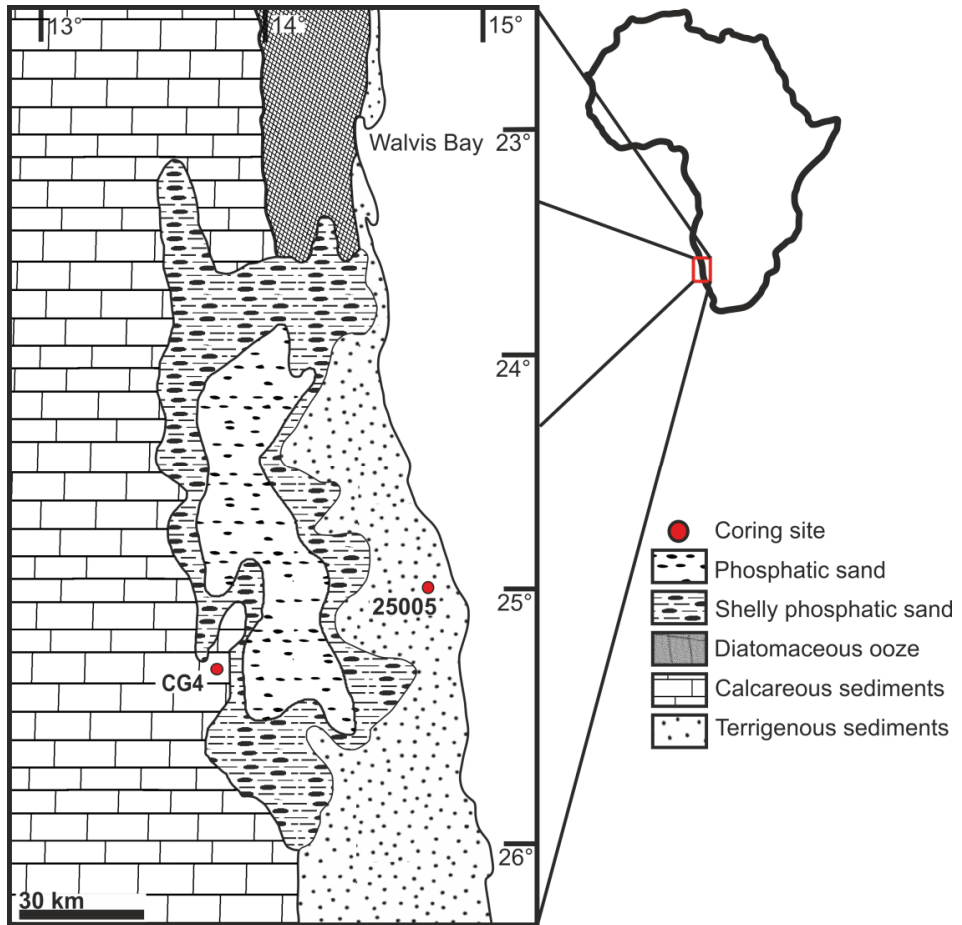


Figure 1. Simplified map of the study area. Modified after Baturin, G. (2000).

4.2. Early Paleozoic shelly phosphorites of the Baltica paleocontinent

The Early Paleozoic Estonian phosphorites were deposited during Cambrian and Ordovician periods on the shallow epicontinental sea of the Baltica paleocontinent. The Cambrian-Ordovician boundary is located in the apatite containing Kallavere Formation (Heinsalu and Viira, 1997). The Kallavere Formation is made up of yellow to grey cross-bedded quartz-rich sandstones with abundant phosphatic bioclasts and carbonaceous shale interbeds (Sturesson et al., 2005), with a maximum thickness of <17 m (Heinsalu and Viira, 1997). The main apatite-containing phases in the Kallavere Formation are lingulate brachiopods, dominantly *Ungula ingraca* (Heinsalu and Viira, 1997). These brachiopods occur as intact shells or fragments of varying sizes, forming lenses and coquinas throughout the formation. Shells contain abundant diagenetic pyrite and hematite (Lang et al., 2016), giving the shells a distinct black-gray or red color, respectively. In addition to biogenic apatite, these rocks contain dark, reworked apatite-cemented clasts, similar to the phosphorite beds of Vassbo, Sweden (Wallin, 1989). These apatite-cemented quartz sand clasts are rounded and flattened, varying in size, ranging from <10 mm to >10 cm. The P₂O₅ concentrations of Kallavere Formation range from 6 to 20% (Baturin and Ilyin, 2013; Raudsep, R., 1997). The phosphorites are usually friable or weakly cemented, although in some localities they are strongly cemented (Soesoo et al., 2020).

During the early Paleozoic, the paleo-continent of Baltica was situated at high to intermediate southern latitudes (Torsvik et al., 2012), analogous to modern day Namibia. The early Paleozoic phosphorites of Baltica were likely deposited under similar conditions to the modern phosphogenic Namibian shelf. On the Namibian shelf, an abundance of shell-rich sediments are found along the coast, with co-occurring organic-rich anoxic sediments on the inner shelf. Similarly, the coquinas and bioclastic lenses in cross-bedded sandstones of the Kallavere Formation were formed as high-energy shoreline/peritidal deposits, whereas the intercalating and overlying graptolitic carbonaceous argillite were accumulated under oxygen-poor deep(er) water conditions (Hiller, N., 1993). A high abundance of apatite-secreting fossils and authigenic apatite concretions, as well as the presence of organic-rich sediments, point towards nutrient-rich conditions and high primary productivity (Baturin and Ilyin, 2013), resulting from an upwelling during the deposition of Kallavere phosphorites (Lécuyer et al., 1998; Parrish et al., 1986).

Peritidal Kallavere phosphorite deposits were redeposited to settings below storm wave base by a rapid transgression during Tremadoc (Artyushkov et al., 2000), leading to the preservation of these erosion-prone deposits (Sturesson et al., 2005). This transgression is evident from the overlying carbonaceous argillite (so-called Dictyonema or graptolite shale) of the Türisalu Formation. The fine-grained carbonaceous shale of Türisalu Formation exhibiting lighter and darker laminae has a maximum thickness of 7 m (Heinsalu and Viira, 1997). In some localities, carbonaceous shale is absent and the Kallavere Formation is unconformably overlain by the glauconitic sand- and siltstones of the Leetse Formation.

In these localities, phosphorites have a distinct red color, likely due to the absence or oxidative remobilization of pyrite.

The post-depositional history of Estonian phosphorites is marked by relative stability and shallow burial. Despite their age, phosphorites are largely unconsolidated and friable, consistent with their shallow burial and little to no thermal maturation. Low conodont alteration indices (CAI = 1–1.5; Heinsalu et al., 2003) further prove that the sediments have not been significantly thermally altered (Kirsimäe et al., 1999). Therefore, these rocks have likely not experienced any significant hydrothermal/late-diagenetic redistribution of REE+Y and other trace metals.

5. MATERIAL AND METHODS

Recent phosphatic sediment samples from the Namibian Shelf were collected during an oceanographic cruise on board R/V *Mirabilis*. Two sediment cores—CG4 and 25005—were retrieved using an Ocean Instruments MC-400 multicorer (Fig. 1). The retrieved cores were sectioned and sampled at a 1 cm interval for the depth of 0–10 cm and at a 2 cm interval below 10 cm. After sectioning, samples were freeze-dried. Core 25005 from the upper shelf (~50 m b.s.l, core length 21 cm) contained concretionary sedimentary apatitic grains. Core CG4 from the middle shelf (~300 m b.s.l, 25 cm core length) contained rounded pelletal apatitic grains.

Cambrian-Ordovician shelly phosphorite samples from Estonia were collected from several different outcrops (Iru, Ülgase, Maardu, Saka localities) and drill cores (in Toolse and Kabala; Fig. 2).

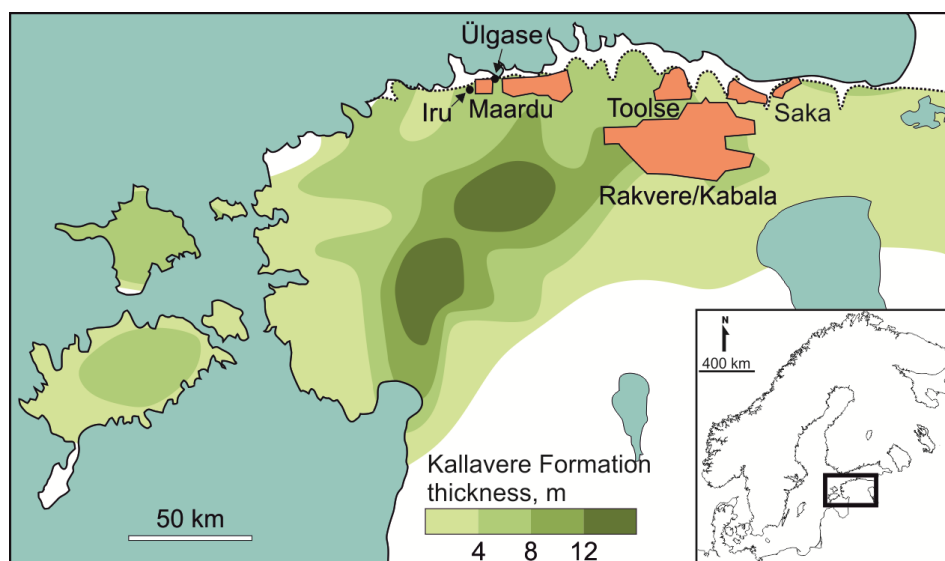


Figure 2. Distribution and thickness of the Kallavere Formation (green) and main Estonian phosphorite localities (pink) sampled in PAPER IV. Modified after Heinsalu and Viira (1997) and Raudsep, R. (1997).

Petrographic, morphological and major elemental analyses were performed using a Zeiss EVO MA15 scanning electron microscope (SEM) coupled to an Oxford X-MAX energy dispersive detector system (EDS) at the University of Tartu. For SEM analysis, phosphorite and phosphatic sediment samples were embedded in Technovit® EPOX. In order to study the internal structure of apatitic grains, some samples were mounted on SEM stubs, ground down and polished to reveal the cross-section of the grains.

Selected cross-sections of recent apatitic grains were further studied using a FEI Tecnai G2F20 X-TWIN transmission electron microscope (TEM) at GeoForschungsZentrum Potsdam, Germany. Sample foils ($15 \times 5 \times 0.15 \mu\text{m}$ in size) for TEM study were cut from embedded and polished samples using a FEI FIB200- TEM. TEM imaging and analysis were performed using Fishione high-angle annular dark-field detector (HAADF), Gatan imaging filter (GIF) Tridiem and EDAX X-ray analyzer with ultra-thin window. Electron energy-loss (EELS) element maps were performed with C-K and S-K edges using the jump-ratio technique

The whole-rock mineralogy of Namibian phosphorites and phosphatic sediments were studied by X-ray diffractometry (XRD) at the University of Tartu. Agate pestle and mortar was used to pulverize the samples. Unoriented samples were measured by a Bruker D8 Advance diffractometer using Cu $K\alpha$ radiation and LynxEye positive sensitive detector in $2-70^\circ 2\Theta$ range. The Rietveld algorithm-based program Topaz was used to interpret the mineralogical composition and apatite lattice parameters of the measured samples.

The trace element composition of phosphorites and phosphatic sediments were measured using inductively coupled plasma mass spectrometry (ICP-MS). The spatial distribution of these elements was studied by means of laser ablation inductively coupled plasma mass spectrometry (LA-ICP-MS). The trace metal concentration of Cambrian-Ordovician shelly phosphorites was studied using Agilent 8800 ICP-MS at the University of Tartu. Apatite samples were hand-picked from bulk samples and washed with milliQ water and 2%_{w/w} ultrapure HNO_3 solution in an ultrasonic bath (1 h for both reagents) to remove terrigenous and other non-apatitic components. After cleaning, the samples were dissolved in concentrated HNO_3 . Indium was used as an internal standard and NIST 1640a, NIST 1643f and POLC-1 as quality control standards. The trace elemental composition of the bulk Namibian phosphatic sediments was measured at Bureau Veritas labs in Vancouver, Canada. A 0.25 g subsample was digested in HNO_3 , HClO_4 and HF, after which it was measured by inductively coupled plasma mass spectrometry (ICP-MS).

LA-ICP-MS analysis were performed on both Recent and Paleozoic phosphorite samples, using Agilent 8800 quadrupole ICP-MS coupled with a Cetac LSX- 213 G2+ laser with HelEx II fast-washout two-volume large-format cell at the University of Tartu. Elemental concentrations were calculated from raw spectrometry using ^{43}Ca as an internal standard, assuming stoichiometric apatite concentration of Ca (39.7%). Certified reference material GSD-1G with values from (Jochum et al., 2011) was used as an external calibration standard for the measurement of Namibian apatitic grains. For the spot measurements of Recent phosphorite samples the following parameters were used: spot size of $50 \mu\text{m}$, a shot count of 40 s, at 10 Hz and a fluence of 1.1 J/cm^2 for the central parts of apatitic grains, whereas the ablation parameters were $25 \mu\text{m}$, 40 s, 10 Hz and 1.65 J/cm^2 for the exterior of the apatites. LA-ICP-MS mapping and line scans were conducted with a spot size of $10 \mu\text{m}$, with a scan speed of $2 \mu\text{m/s}$, at 5 Hz and a fluence of 1.65 J/cm^2 . The LA-ICP-MS parameters during spot analysis of

the Cambrian-Ordovician shelly phosphorites were the following: 25 μm spot size, 10 Hz frequency and fluence of 2 J/cm^2 . LA-ICP-MS mapping parameters for the shelly phosphorites were the following: 20 μm , 10 $\mu\text{m}/\text{s}$, 10 Hz and 1.3 J/cm^2 for spot size, scan speed, frequency and fluence, respectively.

For determining $\delta^{13}\text{C}_{\text{org}}$, $\delta^{15}\text{N}$ and $\delta^{34}\text{S}_{\text{bulk}}$ values, samples were treated with 2 M HCl overnight in order to remove carbonate phases. Decarbonated samples were washed three times with DI water prior to measuring. Total organic carbon (TOC) abundance and $\delta^{13}\text{C}_{\text{org}}$ values were measured using an isotope-ratio mass spectrometer (IRMS) Delta V Plus + Flash HT + Conflo IV at the University of Tartu. Measurements were calibrated using IAEA-CH-3 and IAEA-CH-6 standards. Total nitrogen (TN), total sulphur (TS), $\delta^{15}\text{N}$ and $\delta^{34}\text{S}_{\text{bulk}}$ were measured using MAT253 IRMS + EA IsoLink + Conflo IV at the University of St. Andrews (UK). Calibrations were performed with USGS-40, USGS-41 and USGS-62 for nitrogen and with IAEA-S1, IAEA-S2 and NBS-127 for sulphur.

Phosphate-associated sulphate (PAS) was extracted by applying a modified sample preparation method, as described in Arning et al. (2009) and Canfield et al. (1986). Prior to sulphide and PAS extraction, samples were pre-treated with 1 M NaCl and 1 M ascorbic acid for 24 h to remove easily extractable sulphate (EES). Ascorbic acid was added to inhibit sulphide oxidation. After pre-treatment, the samples were centrifuged and filtered. Around 5 ml of 0.5 M BaCl_2 solution was added to the filtrate to precipitate the EES as BaSO_4 . After 24 h, the EES containing solution was centrifuged and the precipitate was dried.

Chromium reduction was used to extract sulphides from pre-treated sediment samples (Canfield et al., 1986). The samples were transferred to a glass reaction vessel and around 10 ml of ethanol was added. Samples were flushed with N_2 for 15 min, after which 16 ml of 2 M HCl and 16 ml of 1 M CrCl_2 was added to the vessel. The samples were heated on a hotplate for 2 hours. The resulting chromium reducible sulphur (CRS) as H_2S gas was carried by the N_2 into a trapping vessel containing 0.1 M AgNO_3 , where the sulphur precipitated as Ag_2S . The residual mixture of sediment sample, 2 M HCl and 1 M CrCl_2 was centrifuged and filtered. The filtrate was left to react with 0.5 M BaCl_2 for 24 h. The precipitate containing PAS was centrifuged and dried. A separate chromium reduction run was performed where only 2 M HCl was allowed to react with the sample for the first 1 h, prior to adding the CrCl_2 , to separate the acid volatile sulphides (AVS) from CRS. Samples did not contain enough AVS to determine their sulphur isotope composition.

To assess the degree of enrichment or depletion of trace elements, enrichment (EN) was calculated by normalizing the trace element values with Al ($\text{EN}(\text{element X}) = \text{X} (\text{mg}/\text{kg})/\text{Al} (\%)$) (Bennett and Canfield, 2020). The molar ratio of organic carbon to sedimentary phosphorus ($\text{C}_{\text{org}}/\text{P}$; Algeo and Ingall, 2007) was calculated as $\text{C}_{\text{org}}/\text{P} = (\text{TOC} (\text{wt.}\%)/12)/(\text{P} (\text{wt.}\%)/30.97)$. Measured REE+Y concentrations were normalized against Post Archean Average Shale (PAAS; Taylor and McLennan, 1985). REE+Y-based proxies were calculated as: $\text{Eu}/\text{Eu}^* = \text{Eu}_\text{N}/((\text{Sm}_\text{N} + \text{Gd}_\text{N})/2)$, $\text{Ce}/\text{Ce}^* = \text{Ce}_\text{N}/(0.5\text{La}_\text{N} + 0.5\text{Pr}_\text{N})$, $\text{Pr}/\text{Pr}^* = \text{Pr}_\text{N}/(0.5\text{Ce}_\text{N} + 0.5\text{Nd}_\text{N})$, $\text{Y}/\text{Y}^* = \text{Y}_\text{N} ((\text{Dy}_\text{N} + \text{Ho}_\text{N})/2)$ (Bau and Dulski, 1996; Byrne and

Sholkovitz, 1996), $Gd/Gd^* = Gd_N / (Eu_N + Tb_N) / 2$). To assess the degree of MREE-enrichment, bell shape index (BSI) was calculated as: $BSI = (2 * (Sm_N + Gd_N + Dy_N) / 3) / ((La_N + Pr_N + Nd_N) / 3 + (Ho_N + Er_N + Tm_N + Yb_N + Lu_N) / 5)$ (Tostevin et al., 2016). Subscript N denotes PAAS-normalized values for a given element. Stable isotope results are reported as standard delta notations relative to international standards: Vienna PeeDee Belemnite (VPDB) for carbon and Vienna-Canyon Diablo Troilite (VCDT) for sulphur.

6. PHOSPHOGENESIS AND REE+Y UPTAKE IN RECENT NAMIBIAN PHOSPHORITE

6.1. Apatite petrography

The sediment succession in Core 25005 is made up of two distinct types of sediments—apatite-poor, organic-rich and diatom-rich mud in the lower part of the core and apatite-rich sand at the top of the core. Fragile diatom frustules are abundant throughout the core (PAPER III—Lumiste et al., 2021b). The main mineral phases in Core 25005 are quartz, plagioclase, K-feldspar, calcite, glauconite and apatite (PAPER I—Mänd et al., 2018). The terrigenous sediments vary from mud to fine sand, being angular to poorly rounded in shape, occasionally forming fragile ~0.5 mm aggregates with organic matter (Fig. 3a–b). Core CG4 is made up of calcareous phosphatic sand, mostly made up of calcite, quartz, glauconite and abundant apatite (PAPER I—Mänd et al., 2018).

The apatitic grains of Core 25005 and CG4 vary both in abundance, size, and roundedness. The apatite in Core 25005 is typified by dark grey, elongated, subangular to subrounded grains, generally 50–300 μm in size (PAPERS I–III). The surfaces of apatitic grains are irregular and pitted, and, in some cases, covered in a non-phosphatic terrigenous/organic film (Fig. 3c–f). Concretionary grains contain terrigenous mineral grains and fossil debris (Fig. 4a–b). The apatitic grains of Core CG4 are typically 200–500 μm sized, dark grey to black in colour, rounded, and with smooth surfaces. The internal structures of a few rounded grains display concentric layering (Figs 4e), and also diagenetic pyrite and barite are sometime present in the grains.

Scanning electron microscopy reveals the internal structure of Namibian apatitic grains. Micron-scale (2–4 μm wide) particles with radial structures make up the grains, forming either irregular, colloform, globular, dumbbell-shaped or elongated particles (Fig. 5). The most prevalent morphologies are 0.5–4 μm long rod-shaped particles. The rod-shaped particles are, in turn, composed of axial-oriented parallel nanocrystallites, with a diameter of tens of nanometers. The nanocrystals in Core 25005 are elongated and anhedral, whereas in Core CG4 particles are larger, with a distinctly hexagonal morphology. The rod-shaped particles typically co-occur with filamentous or films of organic polymeric macromolecules, which could be the remnants of exopolymeric substances (EPS). In addition, rod-shaped particles often co-occur with diagenetic pyrite framboids. In addition, they frequently intersect or are inter-grown at variable angles. Rod-shaped particles show signs of progressive growth, forming dumbbell-like structures with bulging distal ends, which, in turn, form colloform or spherical microstructures (Fig. 6). TEM analysis shows the heterogeneous internal structures of rod-shaped particles, which are made up of 50–200 nm thick layers of few nanometer diameter apatite crystallites (Fig. 7). The layering might result from variable porosity but could also be due to the varying degrees of sulphur and carbon incorporation into the nanolayers. The apatite crystallites inside the rod-shaped particles often show higher crystallinity than the outer layers.

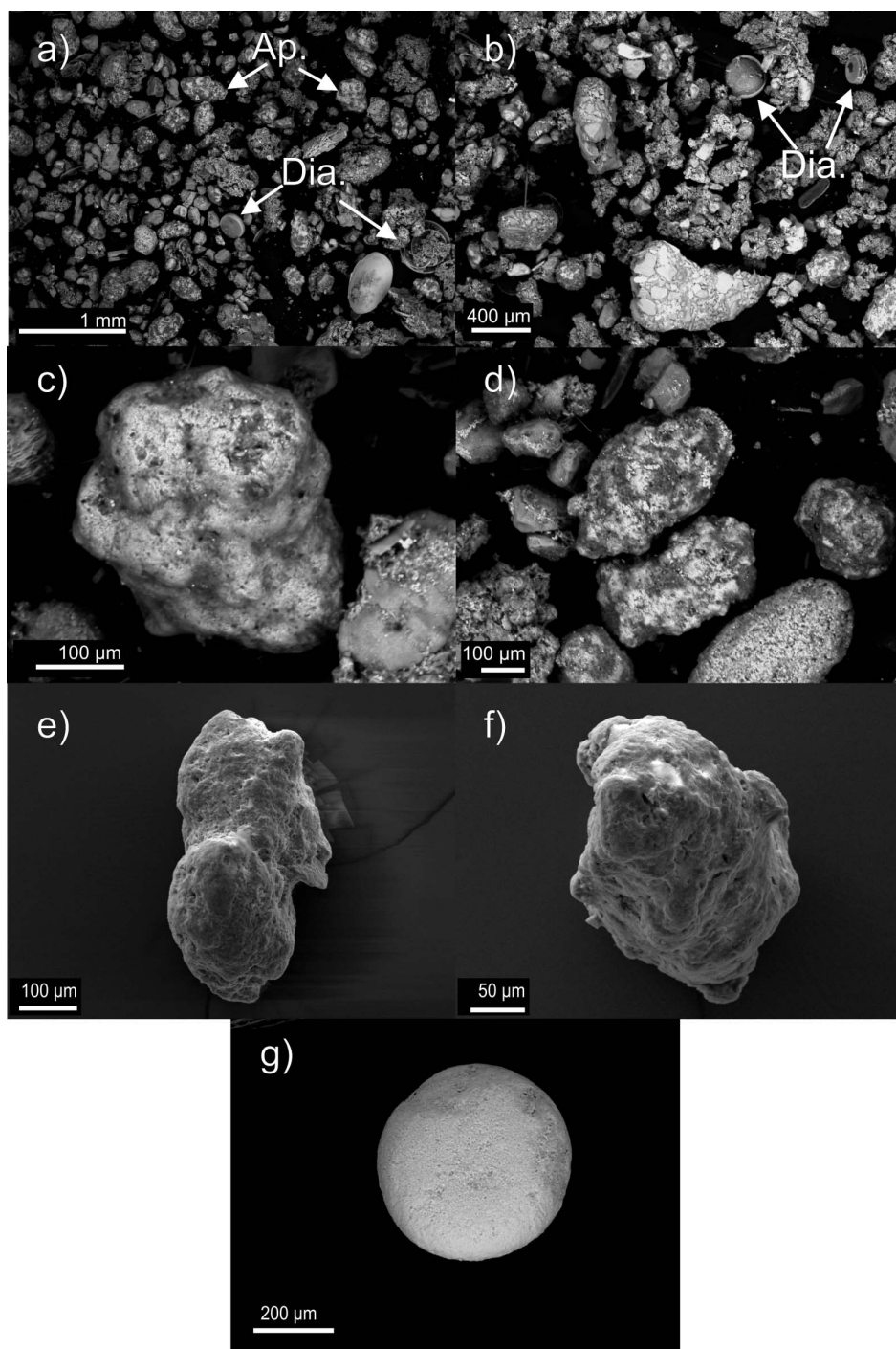


Figure 3. Scanning electron microscope images of: (a–b) bulk sediments, (c–d) apatitic grains with non-phosphatic film coatings, (e–f) apatitic grain morphology showing irregular and pitted surfaces and (g) rounded pelletal apatitic grains with smooth surfaces. Ap.—apatite grains, Dia.—diatom frustules. Figures 3a–f from Core 25005, PAPER III—Lumiste et al. (2021b), 3g from Core CG4, PAPER I—Mänd et al. (2018).

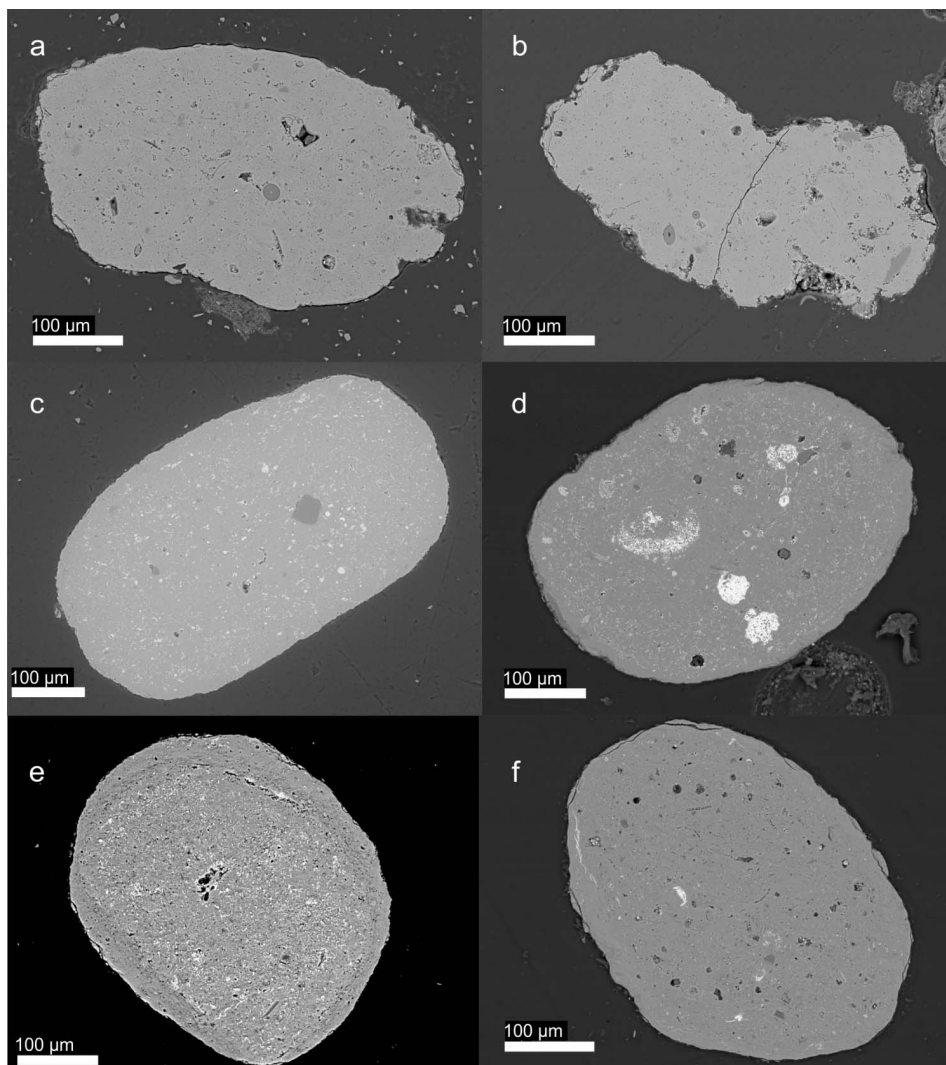


Figure 4. Backscattered and secondary electron scanning electron microscope images of the apatite grains: (a–b) irregular authigenic, concretionary apatitic grains from core 25005, (c,d,f) reworked and rounded pelletal apatitic grains from core CG4 (e) showing concentric layering in some cases (PAPER II—Lumiste et al., 2019).

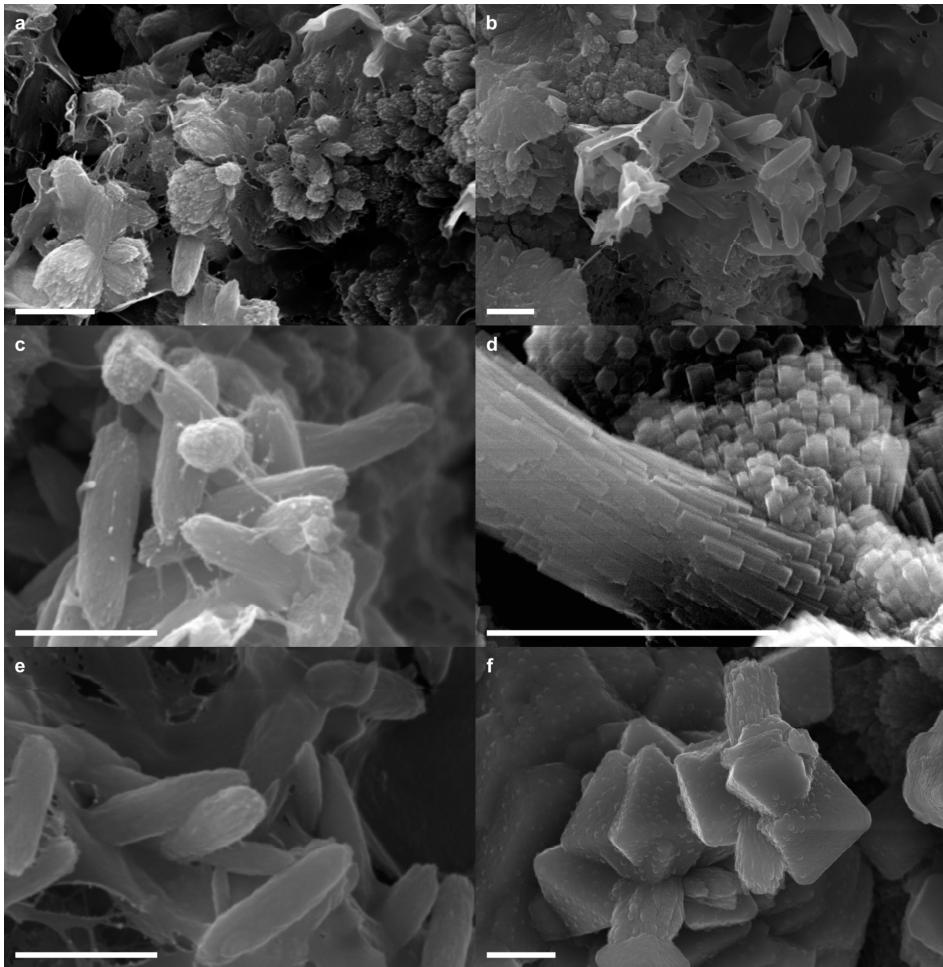


Figure 5. SEM secondary electron (SE) images of apatite particles from broken surface pellets. (a) Diverse forms of apatite microstructures (Core 25005). (b) Abundant apatite rod-shaped particles coat pore walls (Core 25005). (c) Rod-shaped particles in Core 25005 are composed of anhedronal apatite nanocrystallites, oriented parallel to their long axis. Spherical pyrite microaggregate is the lighter structure in the foreground. (d) Apatite particles in Core GC4 are composed of euhedral hexagonal crystallites, oriented in the same manner as in panel c. (e) Rod-shaped particles occur together with a film-like organic substance, seen here filling most of the image (Core 25005). (f) Rod-shaped particles often co-occur with framboidal pyrite (Core GC4). Scale bars represent 1 μm (PAPER I—Mänd et al., 2018).

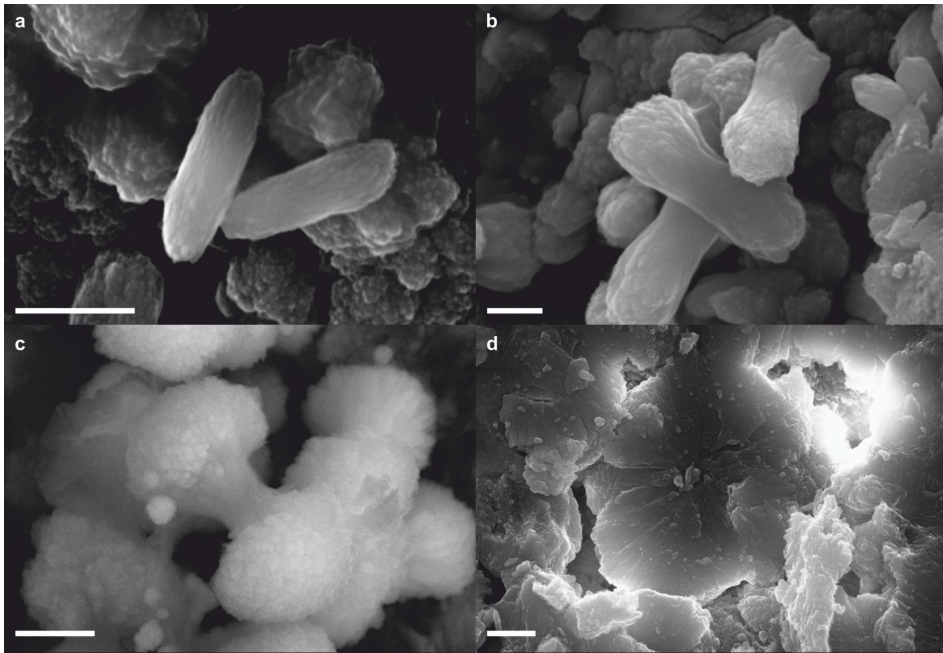


Figure 6. SEM-SE (a,b,d) and SEM-BSE (c) images of progressing apatite growth forms from broken-surface pellets (c from Core GC4, all others from Core 25005). Rod-shaped and other apatite microstructures form a continuum from (a) spindle-shaped elongated rods to (b) rods that start to bulge from their distal ends to (c) dumbbells to (d) spherical particles. Scale bars represent 1 μm (PAPER I—Mänd et al., 2018).

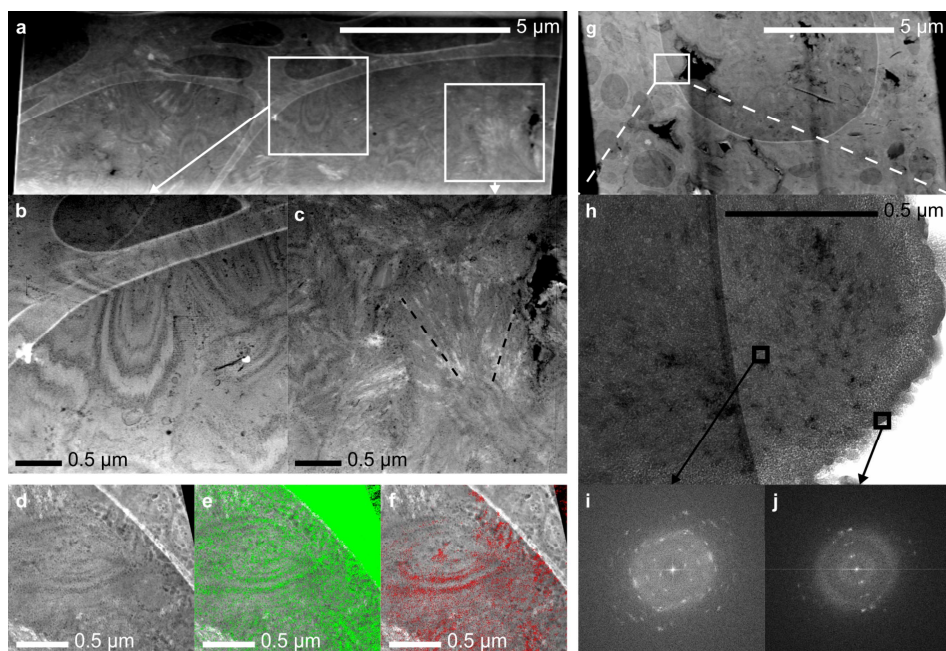


Figure 7. TEM images of inter-grown rod-shaped apatite particles from Core 25005. Large light bands on panels a, b, d–f and g, as well as the dark band covering the left half of panel h, represent carbon filaments, part of the lacy film on which the FIB-cut is mounted. (a, g) High-angle annular dark-field (HAADF) images of entire FIB-foils. (b) HAADF image illustrating the growth of rod-shaped particles in several concentric ~ 50 – 200 nm thick layers, originating from an ellipsoidal ~ 50 – 200 nm wide inner core, alternating between dense and porous. The layers are thickest at the distal ends of the particles. (c) HAADF image showing elongated apatite crystallites radiating along the long axis of the rod-shaped particles (some examples indicated by dashed lines). (d) HAADF image of a rod-shaped particle with layered internal structure; (e–f) overlaid Electron Energy Loss Spectroscopy jump ratio maps of carbon (e) and sulphur (f) of the same area. (h) Bright field image of a rod-shaped particle. (i) Fast Fourier Transformed electron diffraction pattern of the inner layer, showing greater crystallinity (sharp reflections). (j) Fast Fourier Transformed electron diffraction pattern of the outer layer of a rod-shaped particle, showing lower crystallinity (diffuse and smeared-out reflections) (PAPER I—Mänd et al., 2018).

6.2. Major and minor elements

Phosphorus concentrations in Core 25005 increase from 1 wt.% at 0–1 cm depth to a maximum of 1.6–1.9 wt.% at 5–9 cm depth and diminish to values of around 1 wt.% further down the core (Fig. 8). Unlike P, the concentrations of S follow an opposite trend, increasing from 0.6 wt.% at the top of the core, to concentrations of >1 wt.% at 10–11 cm and below (Fig. 8). Al concentrations do not show any significant trends throughout the core, with values ranging from 3.1 to 4.2 wt.%. Based on P-content, Core 25005 can be divided into phosphatic (0–10 cm) and non-phosphatic zones (10–25 cm; PAPER III—Lumiste et al., 2021b).

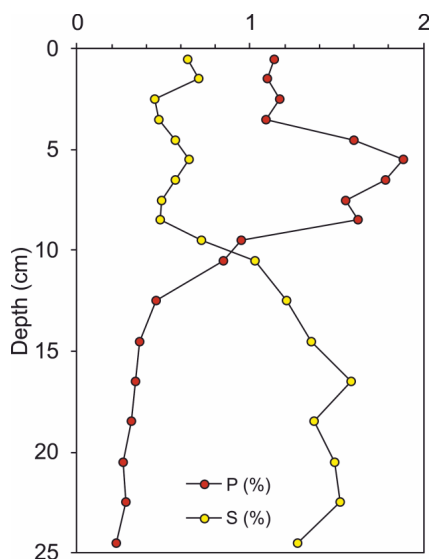


Figure 8. Phosphorus and sulphur content in Core 25005 (wt.%). (PAPER I—Mänd et al., 2018).

The EDS maps of apatitic grains from Core 25005 and CG4 demonstrate its dynamic diagenetic history. Pristine concretionary grains from Core 25005 show abundant fossil and terrigenous inclusions (see Figs. 2a–b, 3 in PAPER II—Lumiste et al., 2019) and little to no diagenetic sulphur species. Reworked pelletal apatitic grains from Core CG4, however, show significant inclusions of pyrite and, in some cases, barite (see Figs. 2c–f, 4 in PAPER II—Lumiste et al., 2019).

Based on the total concentrations and EN values of minor elements, the phosphatic and non-phosphatic zones of the core differ significantly (Fig. 9). The average values of Mo_{EN} , V_{EN} , U_{EN} , Re_{EN} in the upper part are around 1, 35.2, 3.3 and 6.9, respectively, and 2.15, 18.4, 1.5 and 13.2 in the lower part, respectively.

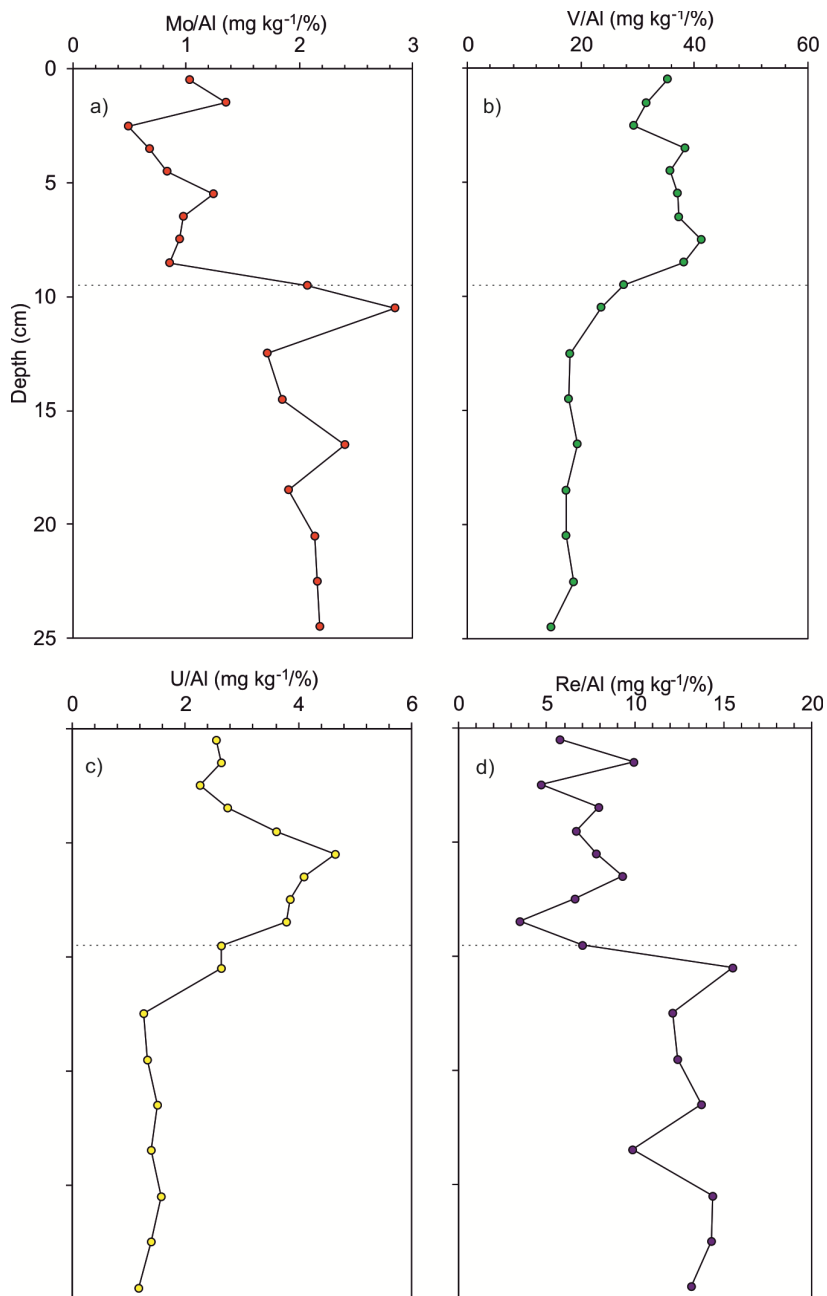


Figure 9. Depth profile of redox-sensitive element concentrations and proxy values: (a) Mo/Al (b) V/Al, (c) U/Al ratios, (d) Re/Al ratios. Dashed lines mark the transition from phosphatic to non-phosphatic sediments. (PAPER III—Lumiste et al., 2021b).

Concretionary apatitic grains from Core 25005 are less enriched in REE+Y and other trace elements than the reworked pelletal apatitic grains in Core CG4. Average \sum REE+Y content in the apatitic grains of Core 25005 is 448 mg/kg, whereas it is 846 mg/kg in the apatitic grains from Core CG4. No correlation between sediment depth and apatite \sum REE+Y content was found in either of the cores (see Fig. 5 in PAPER II—Lumiste et al., 2019). The intragranular distribution of REE+Y is heterogeneous within the apatitic grains. The REE+Y concentrations of the central parts of both type of grains ranges from 3 to 394 mg/kg in the concretionary grains and 1 to 455 mg/kg in pelletal grains, whereas in the exterior layers the average concentrations are 658 and 1621 mg/kg, respectively. All measured grains showed a concentric \sim 20 μ m wide “enrichment zone” of REE+Y in the periphery of the grains (Figs. 10,11).

PAAS-normalized REE+Y patterns measured in the Namibian apatitic grains can be broadly divided into four types: (I) modern seawater-like patterns with negative Ce-anomaly, HREE enrichment and Y/Ho >50, primarily found in the central part of the concretionary grains (Fig. 12b); (II) patterns with slightly negative to no Ce-anomaly, Y/Ho around or slightly below 50 and HREE enrichment found in the central part of pelletal grains (Fig. 12a); (III) patterns with no Ce-anomaly, with Y/Ho typically below seawater ratios and modest HREE enrichment in the enrichment zones of concretionary apatites (Fig. 12d); and (IV) flat shale-like patterns with no or positive Ce-anomalies, near-chondritic Y/Ho ratios and minor HREE enrichment (LREE depletion), typical of the enrichment zones of pelletal apatitic grains (Fig. 12c).

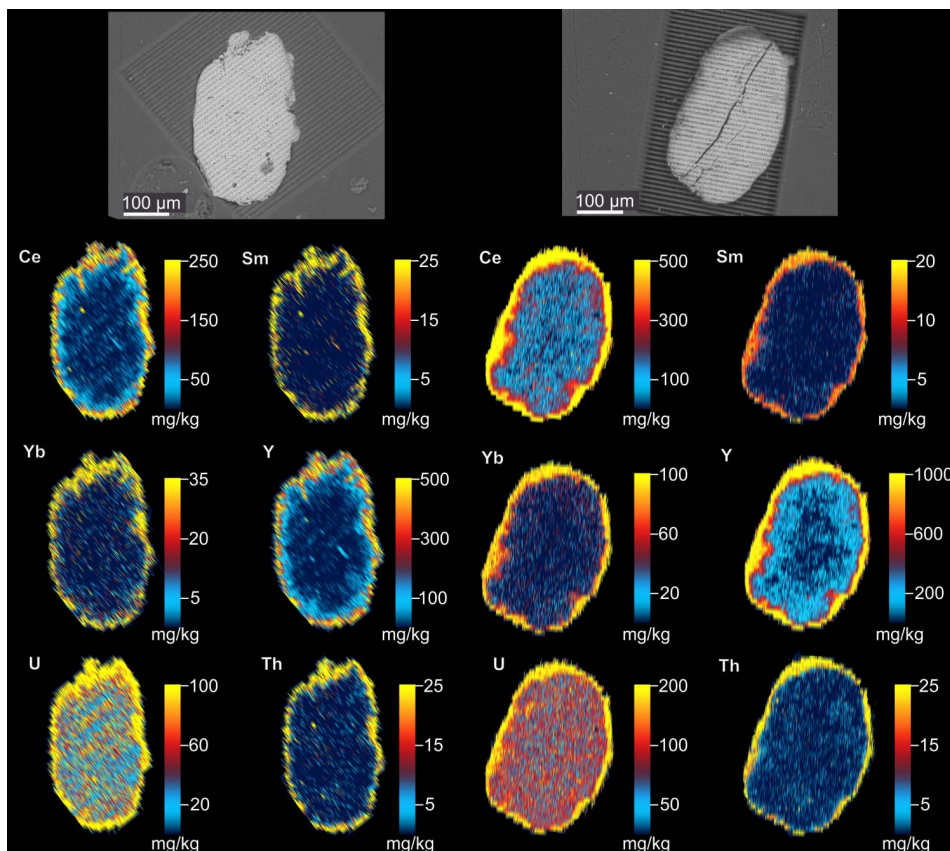


Figure 10. Backscattered scanning electron microscope images of concretionary apatitic grains from core 25005 and LA-ICP-MS elemental distribution maps, showing a clear enrichment of REE+Y in the outer rim of the grains. Scale bars are in mg/kg and show different values for each individual element (PAPER II—Lumiste et al., 2019)

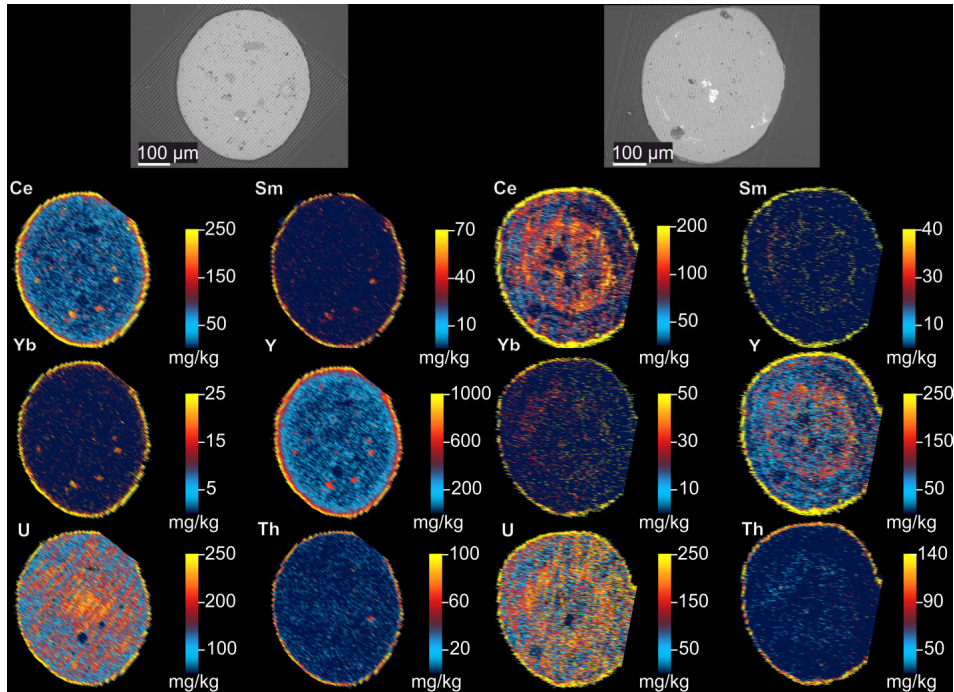


Figure 11. Backscattered scanning electron microscope images of pellet apatitic grains from core CG4 and LA-ICP-MS elemental distribution with enrichment of REE +Y in the outer rim of the grains. Scale bars are in mg/kg and show different values for each individual element. The grain on the right shows concentric layering and several zones of apatite growth. The surface of the internal zone shows enrichment in REE+Y, U and Th, similarly to the enrichment zone of the external layers of the whole grain (PAPER II—Lumiste et al., 2019).

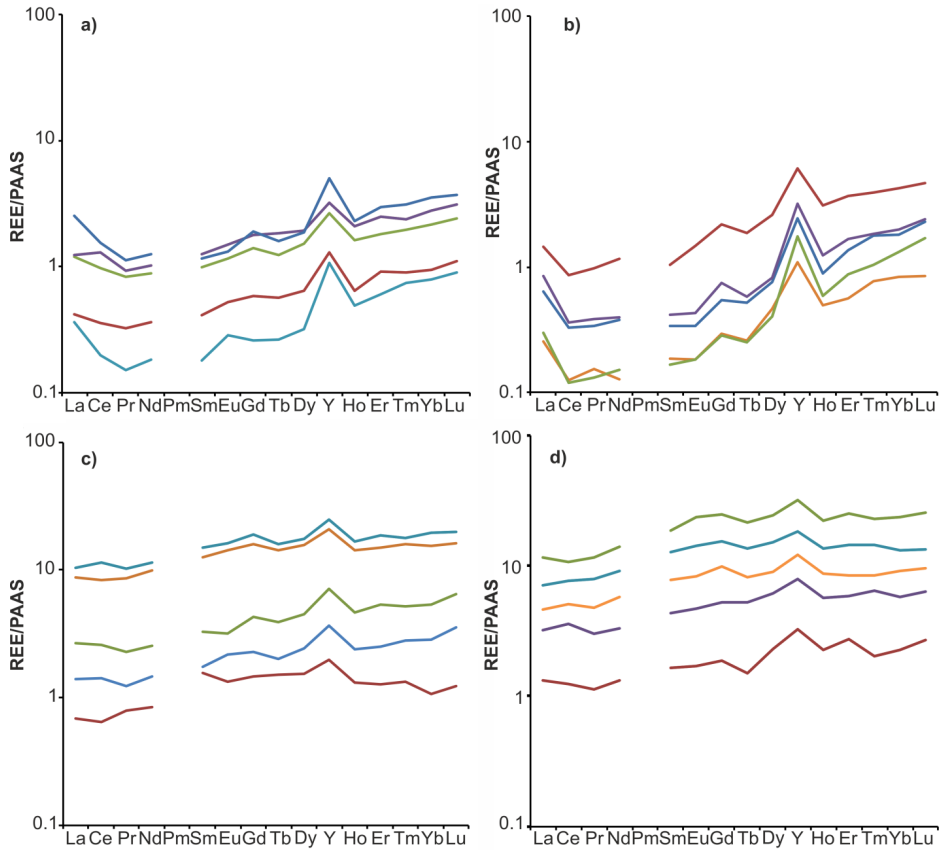


Figure 12. Representative PAAS normalized REE+Y patterns of apatite from: a) Core CG4, grain centre, b) Core 25005, grain centre, c) Core CG4, enrichment zone, d) Core 25005, enrichment zone (PAPER II—Lumiste et al., 2019).

Measured Ce/Ce^* values range from 0.5 to 1.15 (Fig. 13), with negative Ce-anomalies typically associated with the interior of apatitic grains and $Ce/Ce^* \geq 1$ found in the enrichment zones. Y/Ho ratios show a systematic trend, from Y/Ho ratios of >50 in the centre of concretionary grains, to around 30 in the enrichment zone of the pelletal grains (Fig. 14). La_N/Yb_N ratios are higher in the pelletal grains (0.5–0.9 in the centre and 0.4–0.6 in the exterior of the grains), whereas the concretionary grains show less variability with La_N/Yb_N values ranging from 0.2 to 0.4 in both the exterior and interior. La_N/Sm_N are higher and more variable in the centre of both types of apatitic grains, with values ranging from 0.5 to 2.1, whereas in the enrichment zones, the average La_N/Sm_N value is around 0.6. The majority of measured La_N/Yb_N and La_N/Sm_N ratios fall into the range of modern seawater values.

Y/Y^* and La_N/Nd_N ratios display a coherent trend from high Y/Y^* and La_N/Nd_N ratios in the enrichment fronts of both grain types to lower values in the grain interiors of the concretionary grains (PAPER II—Lumiste et al., 2019).

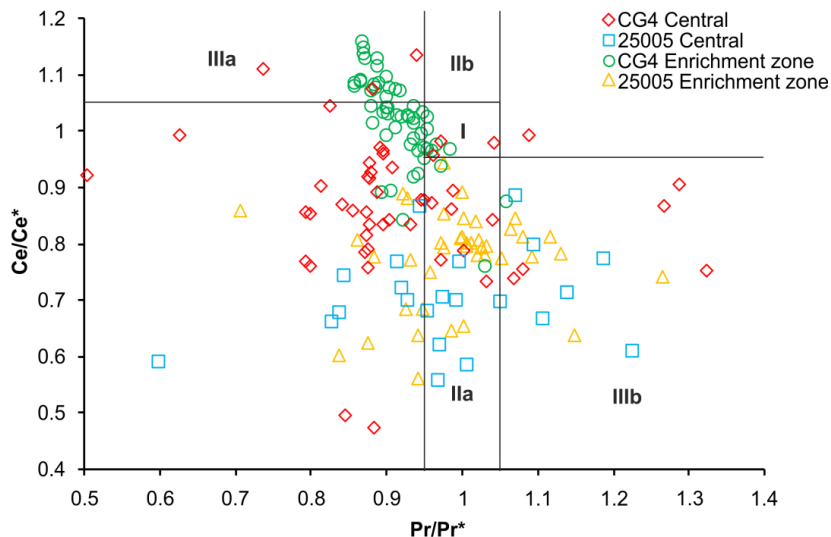


Figure 13. Ce/Ce* vs Pr/Pr* plot. Field I: no La or Ce anomaly. Field IIa: apparent negative Ce anomaly, due to positive La anomaly. Field IIb: apparent positive Ce anomaly, due to negative La anomaly. Field IIIa: true positive Ce anomaly. Field IIIb: true negative Ce anomaly. Modified after Bau and Dulski (1996) (PAPER II—Lumiste et al., 2019).

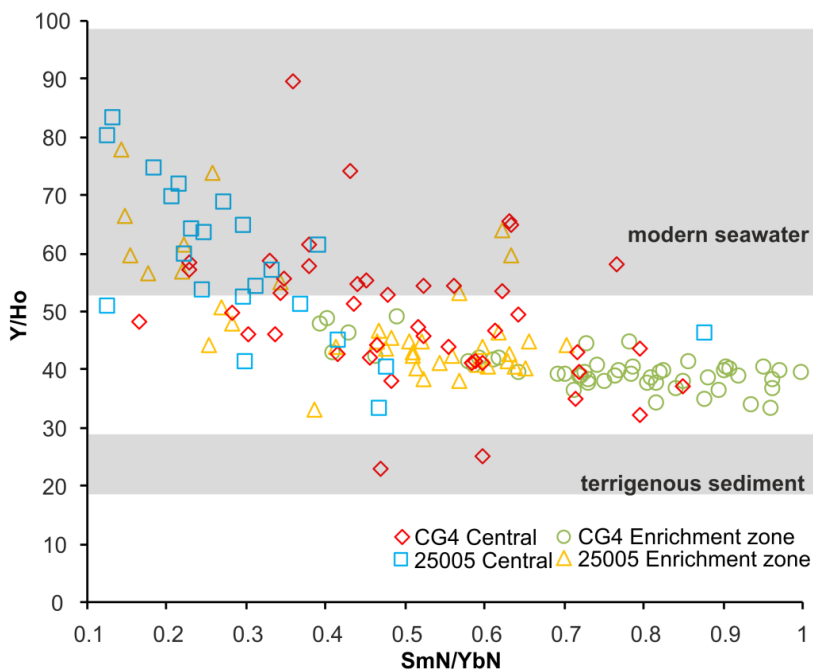


Figure 14. Y/Ho vs Sm_N/Yb_N plot showing a clear decrease in Y/Ho ratios and a growth of Sm_N/Yb_N values with increasing diagenesis. Modified after Kocsis et al. (2016) (PAPER II—Lumiste et al., 2019).

Similar to REE+Y, the distribution of U and Th in apatitic grains is heterogeneous (Figs. 10,11). The exterior of both types of apatitic grains are significantly enriched with U and Th, the width of their enrichment zones being largely the same as that of REE+Y. Reworked pelletal grains contain more U and Th, as well as REE+Y (PAPER II—Lumiste et al., 2019).

6.3. Stable isotopes

The total organic carbon concentrations in Core 25005 vary from 0.71 to 4.78 wt.% (Fig. 15b), with significant differences between the lower and upper sections of the core. Similarly, the $\delta^{13}\text{C}_{\text{org}}$ values differ between the lower and upper parts, from -21.05‰ to -19.68‰ (Fig. 15a).

CRS $\delta^{34}\text{S}$ values increase from -20.25‰ at the top of the core to 2.54‰ at the end of the core (Fig. 15c). Both PAS and EES are lighter than modern seawater sulphate at the top of the core (19.16‰ and 16.48‰ at 0–1 cm depth, respectively), whereas EES $\delta^{34}\text{S}$ values progressively increase with depth, becoming heavier than seawater sulphate at a depth of 10–11. PAS remains lighter than seawater sulphate throughout the core (Fig. 15d). PAS $\delta^{34}\text{S}$ values are also relatively uniform with only 3.7‰ variability between the minimum and maximum values (PAPER III—Lumiste et al., 2021b).

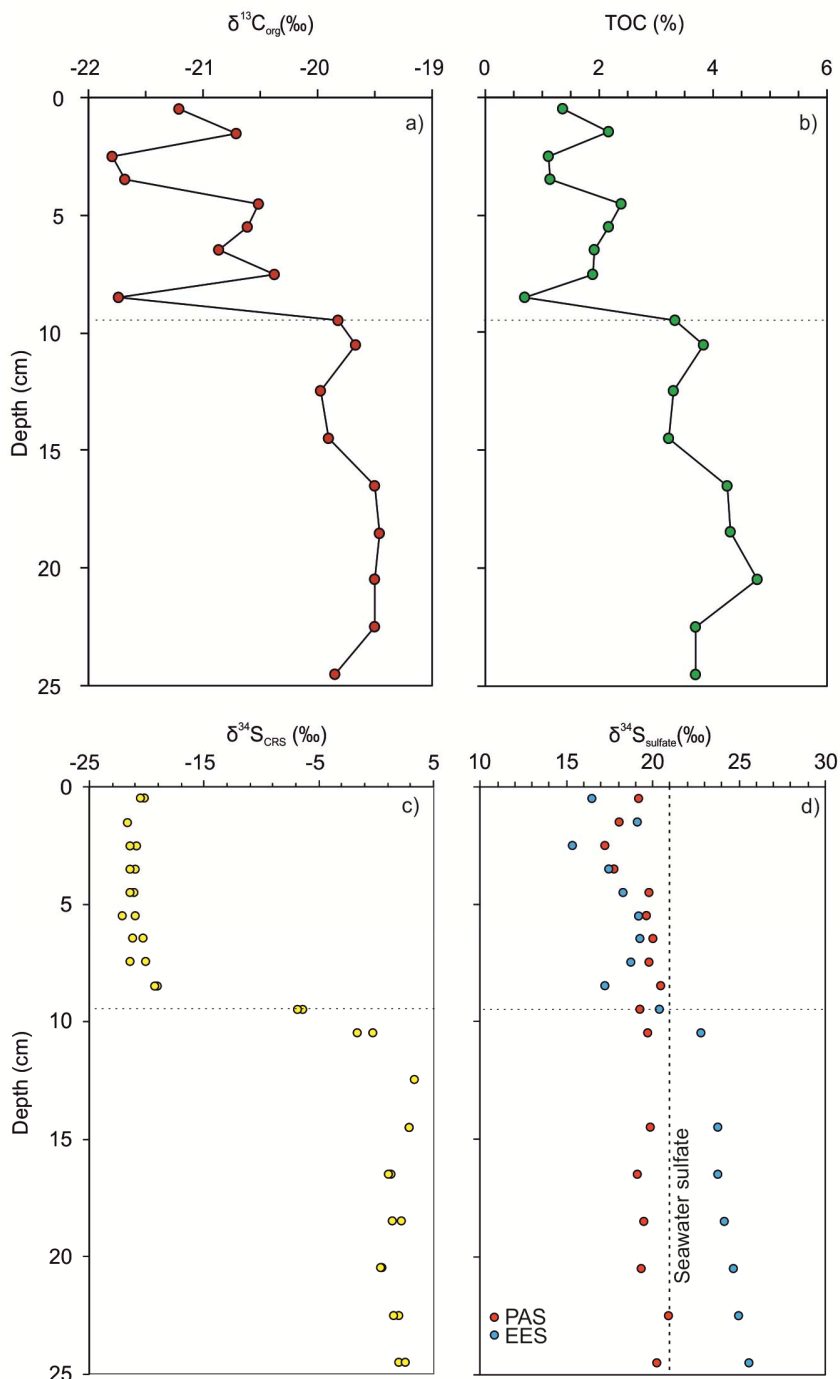


Figure 15. Depth profiles of (a) $\delta^{13}\text{C}_{\text{org}}$, (b) total organic carbon and $\delta^{34}\text{S}$ composition of different sulphur phases, (c) chromium reducible sulphur and (d) phosphate associated sulphate (PAS) and easily extractable sulphate (EES). Modern seawater sulphate value from Paytan et al. (1998) (PAPER III—Lumiste et al., 2021b).

6.4. (Bio)geochemical constraints of phosphogenesis on the Namibian shelf

Phosphorites are formed under dynamic redox and sedimentary settings. Due to the dynamic environment and the high specific gravity of sedimentary apatite (2.9 g/cm^3 ; Föllmi, K.B., 1996), phosphorites and phosphatic sediments are prone to reworking and winnowing on short timescales. Given the relative scarcity of *in-situ* phosphorites and phosphatic sediments, there is little geochemical data on *in-situ* occurrences, meaning that the biological and chemical factors driving phosphogenesis are somewhat poorly understood.

The bulk sediments of Core 25005 are made up of diatomaceous mud and apatite-rich sand in the lower part and upper part of the core, respectively. Diatom frustules are also abundant in the apatite-rich upper portion of the core (Fig. 3a–b). A high abundance of mechanically weak low-density frustules (Miklasz and Denny, 2010), coupled with the angular to, poorly rounded shape of the terrigenous grains, occasionally forming fragile organics-mineral aggregates, point towards these sediments being only slightly reworked, or not at all. Furthermore, the subangular to subrounded apatitic grains with irregular and pitted surfaces from Core 25005 provide further proof for the *in-situ* origin of these sediments.

The apatitic grains of Core 25005 are smaller, more porous and less rounded than the reworked grains of Core CG4, containing little or no pyrite inclusions or secondary apatite growth (Figs. 3c–d, g, 4a–b). The appearance of the apatitic grains, an abundance of diatom frustules and poorly rounded terrigenous minerals all indicate that these sediments are *in-situ*, their composition not having been extensively altered by winnowing (PAPER III—Lumiste et al., 2021b).

The maximum P abundance in Core 25005 is found in a 4–5 cm thick interval directly above TOC- and sulphur-rich sediments (PAPER I—Mänd et al., 2018, PAPER III—Lumiste et al., 2021b). The concentrations of pyrite in the phosphatic interval is around 0.7 wt% increasing rapidly in the organic-rich portion of the core, reaching values as high as 3.2 wt% (PAPER I—Mänd et al., 2018). On the shelf of Namibia, sulphide is effectively oxidized by LSB, with only around 1% of total sulphide being buried in the sediment as pyrite or organic sulphur species (Dale et al., 2009), pointing towards a dynamic sulphur cycle in the Namibian phosphogenic sediments, involving both oxidative and reductive sulphur metabolic pathways. Typically, the sulphide in diagenetic pyrite in marine sediments is derived from either methanotrophic or organoclastic sulphate reduction (Lin et al., 2016). The microbial reduction of sulphate to sulphide favours the lighter ^{32}S isotope, leaving residual SO_4^{2-} enriched in the heavier ^{34}S isotope. The fractionation between these two sulphur species can be as large as 70‰ (Canfield et al., 2010; Sim et al., 2011). Pyrite precipitation utilizing microbially produced sulphide only results in around 1‰ fractionation (Price and Shieh, 1979). Hence, sedimentary pyrite $\delta^{34}\text{S}$ values reflect pore water sulphide isotope ratios during their formation. Pore water sulphide $\delta^{34}\text{S}$ values of modern (non-euxinic) marine sediments follow a gradual, nearly linear downcore trend from -45‰ near the

SWI to higher values at depths where the sulphate pool is depleted with sulphate reduction occurring under closed system conditions (e.g., Lin et al., 2016; Peketi et al., 2012; Pellerin et al., 2018). This is due to the presence of highly reactive iron and/or microbial sulphate reduction rates exceeding the replenishment rate of sulphate (Jorgensen, 1979). The pyrite $\delta^{34}\text{S}$ values measured in Core 25005 follow a similar trend, ranging from -22% to 3% downcore, indicating a shift from a relatively open system to a more closed system with sulphate reduction downcore (PAPER III—Lumiste et al., 2021).

Sulphate is a common substitute for PO_4 in apatite (Pan and Fleet, 2002), with concentrations as high as $2.7\pm 0.3\%$ (McArthur, J., 1985). The $\delta^{34}\text{S}$ phosphate-associated sulphate (PAS) can provide information about the microbial triggers of phosphogenesis. Coupled with the shifts in pyrite $\delta^{34}\text{S}$ caused by microbial sulphate reduction, the residual sulphate pool should become progressively enriched in the heavier ^{34}S isotope as depth increases. However, in Core 25005 the phosphate-associated sulphate (PAS) values of $17\text{--}21\%$ do not increase with depth and remain slightly lower than modern marine sulphate values throughout the core. In the uppermost 4 cm, the PAS $\delta^{34}\text{S}$ values are around $2\text{--}4\%$ lower than seawater sulphate, and around 1% lower in the rest of the core (PAPER III—Lumiste et al., 2021b).

The lighter-than-seawater values of PAS $\delta^{34}\text{S}$ have been interpreted to be caused by bacterial sulphide oxidation (Arning et al., 2009a). If PAS values reflect a mixture of two endmembers—oxidized sedimentary sulphide and seawater sulphate—then in order to explain the low PAS $\delta^{34}\text{S}$ values, a maximum of 8.8% of sulphate taken up by apatite would have been derived from reoxidized sulphide (PAPER III—Lumiste et al., 2021). An important implication of the nearly (but not equal) marine sulphate of PAS $\delta^{34}\text{S}$ is that the primary nucleation and precipitation of apatite occurs in the topmost portion of the sediment, in a relatively open system with good diffusive connection with the overlying water column, but still involves microbially sourced sulphate (PAPER III—Lumiste et al., 2021b).

The Namibian Shelf is typified by the absence of large riverine input, low eolian delivery relative to marine bioproduction and low $\text{C}_{\text{org}}/\text{N}$ ratios (Meisel et al., 2011b, 2011a), indicating that the dominant source for organic carbon in Core 25005 is marine organic matter. The $\delta^{13}\text{C}_{\text{org}}$ values of Core 25005 are rather stable, decreasing from around -19.5 to -20% in the non-phosphatic to -21% in the phosphatic portion of the core (PAPER III—Lumiste et al., 2021), showing a remarkable correlation between TOC and $\delta^{13}\text{C}$ ($r = 0.96$, $p\text{-value} < 0.01$, $n = 18$; PAPER III—Lumiste et al., 2021b). The $\delta^{13}\text{C}_{\text{org}}$ values in the organic-rich muds of the Namibian shelf typically vary from -18 to -20% , but they can drop to values lower than -21% in some instances (Meisel et al., 2011a). The high $\delta^{13}\text{C}_{\text{org}}$ values from Core 25005, compared to the global average of ca -25% for marine biomass, can be caused by high seawater temperatures ($>25\text{ }^\circ\text{C}$) regulating CO_2 dissolution rates in the water column and driving up $\delta^{13}\text{C}_{\text{CO}_2}$ values. Alternatively, these $\delta^{13}\text{C}_{\text{org}}$ values could have been caused by very high rates of primary production under normal lower surface ocean temperatures ($\sim 16\text{ }^\circ\text{C}$). The shift

seen in the $\delta^{13}\text{C}_{\text{org}}$ values of Core 25005 (Fig. 15a) can then be explained by higher rates of primary production in the lower part of the core and declining productivity in the phosphatic sediments (PAPER III—Lumiste et al., 2021b).

The trace elemental composition of Core 25005 shows a direct link between redox conditions and the enhanced sequestering of apatite. Some redox-sensitive elements (e.g., Mo, Ni, V, Re and U) behave (quasi-)conservatively under oxic seawater conditions, but they become enriched in sediments accumulating under reducing conditions (Tribovillard et al., 2006). The relative proportions of these elements, when normalized to a redox-insensitive element (e.g., Al), reflect the dominant redox conditions during the formation and the subsequent diagenesis of authigenic phases (Bennett and Canfield, 2020).

The authigenic enrichment of Mo is closely tied to the presence of free sulphide. Under oxic conditions, dissolved Mo occurs as an inactive MoO_4^{2-} ion, whereas under anoxic (euxinic) conditions, reactive thiomolybdates ($\text{MoO}_x\text{S}4^{2-x}$) are the dominant species (Tribovillard et al., 2012). Particle-reactive Mo species are scavenged and precipitated in sulfidic environments by iron sulphides, Fe-Mo-S phases (Helz and Vorlicek, 2019) and/or organic particles (Dahl et al., 2017). Enrichment factors of Mo change from around 2 in the non-phosphatic zone to around 1 in the phosphatic zone. Mo concentrations also display strong correlation with TOC ($r = +0.92$, $p\text{-value} < 0.01$, $n = 18$) with lower Mo and TOC values in the phosphatic zone, signalling a shift towards less-reducing conditions during the formation of apatite (PAPER III—Lumiste et al., 2021b). Similarly, the enrichment of Re is coupled to the dominant redox conditions. Under anoxic conditions, via diffusion and fixation as solid authigenic phases, Re becomes enriched (Crusius et al., 1996; Morford et al., 2005). Re_{EN} values show a twofold decrease, from 13 to 7, as the sediments become phosphatic. Alternatively, the apparent shift towards suboxia could be caused by the diffusion of oxic seawater into the sediment, enhanced by bioturbation, allowing oxygen to penetrate deeper into the sediment. In this case, the changes in redox elements would not reflect changes in local redox, but reflect the position of “modern” redoxclines instead. Mollenhauer et al. (2007) have estimated the thickness of disturbed sediment layer to be around 10 cm on the Namibian Shelf, coinciding with the shift in Mo and Re accumulation. However, Core 25005 is located in a region characterized by low annual bottom water oxygen ($< 20 \mu\text{M}$) and transient anoxia (Brüchert et al., 2006). Hence, the changes in the redox-sensitive element are more parsimoniously explained by changes in the dominant redox conditions. Furthermore, the co-occurring increase in phosphate accumulation and shift towards suboxic conditions near SWI seem to be causally linked.

Trace metal data from Core 25005 show a link between the shift towards suboxia in the dominant redox conditions and the initiation of phosphogenesis (Figs 8–9). The transition from sulfidic TOC-rich pore water conditions to TOC-poor suboxic conditions was likely caused by changes in organic matter delivery under dynamic upwelling conditions. While suboxia likely dominated during the formation of phosphatic sediments, the presence of diagenetic pyrite in the phosphatic zone (PAPER I—Mänd et al., 2018) indicates that transient sulfidic

conditions still existed. Modern phosphogenesis occurs in the periphery of organic-rich muds (Burnett et al., 1983), typified by dynamic redox conditions (“poikiloxia”). Redox conditions near the SWI on upwelling shelves can fluctuate between sulfidic-suboxic-oxic on both long-term (>100 years; Algeo and Li, 2020; Hoetzel et al., 2017) and short-term scales (monthly/daily, Bailey and Chapman, 1991; Brüchert et al., 2006, 2003). This type of redox dynamics would promote the bacterial P-pump (*sensu* Brock and Schulz-Vogt, 2011), by allowing LSB to accumulate phosphate during suboxic conditions and release it during short-term shifts towards sulfidic conditions.

Redox conditions also exert additional constraints on phosphogenesis by regulating the alkalinity of pore water. Organic matter degradation through sulphate reductions leads to increased pore water alkalinity (Berner et al., 1970). Apatite precipitation is, however, inhibited by high alkalinity (Briggs and Wilby, 1996; Föllmi, K.B., 1996; Glenn and Arthur, 1988), due to a decrease in free calcium ions caused by competing Ca-carbonate precipitation (Glenn and Arthur, 1988; Nathan and Sass, 1981; Song et al., 2002). In shallow sediments influenced by upwelling, there is a continuous increase in alkalinity with sediment depth (Noffke et al., 2012), limiting apatite precipitation to the topmost few centimeters (Krajewski, 1994). Similarly, during the deposition of organic-rich diatomaceous mud in Core 25005, a higher flux of organic matter could lead to higher pore water alkalinity near the SWI, inhibiting phosphogenesis.

In addition to the canonical interpretation of bacterial P-pump as the controlling mechanism for phosphogenesis, preconcentration of P via organic matter degradation and the Fe-Mn oxyhydroxide “redox pump” could also modify interstitial phosphate concentrations through the release of particle-bound phosphate (Jarvis et al., 1994; Küster-Heins et al., 2010; Noffke et al., 2012; Pufahl and Grimm, 2003). Both the Fe-Mn “redox pump” (Tribovillard et al., 2006) and the LSB P-pump would operate efficiently under similar redox conditions—accumulation during (sub)oxic conditions and rapid release of P during reducing conditions. Both processes occur at similar depths of around 2–4 cm below the SWI on the Namibian Shelf (Küster-Heins et al., 2010; Schulz and Schulz, 2005), making it difficult to distinguish between the relative roles of these two mechanisms. However, the REE+Y composition of concretionary apatite grain centres is more similar to oxic seawater than to pore water influenced by dissolved Fe-Mn oxyhydroxides (PAPER II—Lumiste et al., 2019), suggesting that primary nucleation likely occurred prior to the dissolution of Fe-Mn particles. Moreover, the dynamic redox conditions on the Namibian Shelf (e.g., Brüchert et al., 2006) would significantly inhibit the Fe-Mn redox pump during periods of low oxygen in the water column. The sediments of the main locus of phosphogenesis—the diatomaceous ooze belt—is also somewhat depleted in Fe and strongly depleted in Mn (Borchers et al., 2005), making it unlikely that the Fe-Mn redox pump exerts primary control on interstitial phosphate concentrations. Furthermore, the measured PAS $\delta^{34}\text{S}$ values (PAPER III—Lumiste et al., 2021b) are more in line with the microbial origin of the apatitic grains than the Fe-Mn redox pump.

In addition to dynamic redox conditions, bacterial P-pump and pore water alkalinity, the presence of organic substrates seems to exert additional control on phosphogenesis as well. The close association between rod-shaped particles—the primary shape of apatite nuclei making up the apatitic grains—and organic macromolecules point towards primary precipitation being controlled by organic substrate (PAPER I—Mänd et al., 2018). Sedimentary apatite is thought to precipitate via metastable amorphous precursor phases (Gunnars et al., 2004; Krajewski, 1994). This precipitation occurs as a fast-paced supersaturation-nucleation-depletion cycles in the topmost centimeter of the sediment column (Krajewski, 1994). In addition to organic polymers, apatite precursor phases have been considered as templates for primary apatite precipitation (Cappellen and Berner, 1991; Gunnars et al., 2004; Krajewski, 1994). Apatite has been shown to nucleate homogeneously in experimental studies (Ross et al., 2017) using highly variable nucleation surfaces (Krajewski, 1994), coupled with the high density of apatite growth sites (PAPER I—Mänd et al., 2018). This would indicate that primary nucleation and phosphogenesis are not strongly dependent on specific nucleation conditions. However, in the apatitic grains of Core 25005 and CG4, organic matter appears in association with apatite particles almost without exception, while the carbon- and sulphur-enriched porous layers within the rod-shaped particles possibly represent remnants of organic-rich lamellas. Furthermore, the microstructures of apatitic grains bear close resemblance to laboratory grown fluorapatite-gelatin nanocomposites, in which organic macromolecules play a central role in controlling the apatite precipitation (*sensu* Kniep and Busch, 1996), providing nucleation surfaces for apatite and directing the aggregates' growth patterns. Hence, LSB exert twofold control on phosphogenesis by providing both the phosphorus needed for precipitation as well as suitable nucleation surfaces (PAPER I—Mänd et al., 2018).

6.5. Diagenetic uptake of REE+Y and other trace metals in apatite

The REE(+Y) patterns of biogenic apatite have repeatedly been shown to provide unreliable records for interpreting secular seawater trends and paleoredox conditions (Chen et al., 2015; Herwartz et al., 2013; Trotter et al., 2016; Zhao et al., 2013). Unlike biogenic apatite, which is primarily made up of metastable hydroxyapatite, which is readily recrystallized to a more stable carbonate-rich fluorapatite apatite phase (Trueman, 2013), authigenic sedimentary apatite precipitates already as carbonate-rich fluorapatite (CFAp), which is thermodynamically stable under seawater and early diagenetic pore water conditions (Jahnke, 1984). Therefore, sedimentary CFAp has been used to study the ambient seawater conditions in ancient (Emsbo et al., 2015; Shields and Stille, 2001) and modern phosphorites (Piper and Bau, 2013). However, during precipitation, sedimentary apatites contain very low concentrations of REE as the majority of

these elements are only taken up during subsequent water-mineral interactions (McArthur and Walsh, 1984), either from seawater or diagenetic pore water with distinctive and dissimilar REE+Y budgets (e.g., Abbott et al., 2015; de Baar et al., 1985; Deng et al., 2017; Elderfield and Greaves, 1982; Haley et al., 2004; Wang and Yamada, 2007).

The distribution of REE+Y in Namibian apatitic grains is highly variable. The exteriors of both concretionary and pelletal apatitic grains contain significantly more REE+Y (on average 658 and 1621 mg/kg, respectively) than the grain centres, with concentrations varying from 3–394 mg/kg and 1–455 mg/kg in concretionary and pelletal grains centres, respectively (PAPER II—Lumiste et al., 2019). The REE+Y are typically enriched in zones only a couple of tens of μm wide. However, the REE+Y patterns in grain centres and in the outer REE+Y-rich layer are distinctively different. The most pristine apatites from the interior of concretionary grains are characterized by seawater-like REE+Y patterns with a negative Ce-anomaly, high Y/Ho ratios, HREE enrichment. The REE+Y patterns of the centre of pelletal grains are somewhat altered, displaying slightly higher ΣREE , weak negative to positive Ce-anomalies, and reduced HREE enrichment, when compared with concretionary grain centres. However, Y-enrichment is still present. The outermost zones of both types of apatite grains are characterized by significant LREE-enrichment, low Y/Ho ratios, and an absence of negative Ce-anomalies, which are, in some cases, replaced by positive Ce anomalies. Given that the increase in REE+Y concentrations is coupled a gradual loss of primary seawater signatures, the source for the REE+Y is most probably suboxic-sulfidic pore water (Abbott et al., 2015; Deng et al., 2017; Haley et al., 2004). Interestingly, the older reworked pelletal grains show the highest REE+Y concentrations, but do not exhibit wider enrichment zones, indicating that the zones seem to take up REE+Y continuously, causing a higher degree of enrichment. However, the grain centres are not significantly affected, likely due to inhibited diffusion and ion exchange between grain interiors and pore water. However, the loss of true negative Ce-anomalies, lowering of Y/Ho ratios, LREE-enrichment and slightly higher REE+Y concentrations in the centre of pelletal grains, when compared with concretionary grain interiors, suggests (limited) diagenetic influence even in the centre of apatitic grains.

The REE+Y patterns of apatitic grains from Core 25005 from the active phosphogenetic belt on the Namibian shelf further support the interpretation of dynamic redox conditions during phosphogenesis. Y and Ho are geochemical twins due to their identical charge and similar ionic radii. In most geological processes, Y and Ho are coupled, their relative concentrations are reflected by a stable (chondritic) Y/Ho ratio of around 28 (Bau and Dulski, 1996; Minami et al., 1998). However, in marine settings, Fe-Mn oxyhydroxides preferentially scavenge Ho, leading to Y-enriched seawater and superchondritic Y/Ho ratios of >50 (Nozaki et al., 1997). During the reductive dissolution of Fe-Mn oxyhydroxides, particle-bound Ho is released into pore water, lowering its Y/Ho ratio (Bau et al., 1997).

Similarly, the behaviour of Ce is governed by the redox cycling of Fe and Mn. Under oxic conditions, trivalent Ce is oxidized to Ce⁴⁺ (McArthur and Walsh, 1984) and scavenged by Fe-Mn Oxyhydroxides, leaving seawater depleted in Ce, compared with neighbouring REEs (Bau and Koschinsky, 2009; Byrne and Sholkovitz, 1996). This negative Ce-anomaly is, however, gradually erased and subsequently replaced by a positive anomaly in suboxic-sulfidic pore water, where particle-bound Ce is released during the reductive dissolution of Fe and Mn particles (Takahashi et al., 2015).

The LA-ICP-MS measurements of apatitic grains from Core 25005 show seawater-like Y/Ho ratios and, in some cases, true negative Ce-anomalies (*sensu* Bau and Dulski, 1996) in the central part of the grains. This suggests that primary nucleation and precipitation must occur in a seawater-controlled environment. However, in the outer margins of the grains, Y/Ho ratios are already below seawater threshold, true negative Ce anomalies being largely absent (Fig. 16; PAPER II—Lumiste et al., 2019), which is indicative of REE+Y uptake from suboxic pore water (Deng et al., 2017; Haley et al., 2004; Kim et al., 2012). Interestingly, these types of enrichment fronts with characteristic Y/Ho ratios of <50 and positive Ce-anomalies, if any, are even present in the apatitic grains at the SWI (0–1 cm depth). These enrichment fronts, coupled with the presence of ~1 wt% of pyrite in the upper part of the core, indicates that suboxic-sulfidic pore water dominates the REE+Y budget and redox conditions of pore water even at the SWI, at least periodically (PAPER II—Lumiste et al., 2019).

The Namibian phosphatic sediments are young on a geological timescale, their age ranging from Miocene to Recent (Baturin, G, 2000; Compton and Bergh, 2016). The REE+Y patterns of these relatively young phosphorites are, however, already significantly altered (PAPER II—Lumiste et al., 2019). The overprinting of primary seawater REE+Y signal seems to occur relatively early, making sedimentary apatites ambiguous carriers of information regarding past secular trends in seawater (PAPER II—Lumiste et al., 2019).

In addition to REE+Y, phosphatic sediments of Core 25005 are anomalously enriched in several other redox-sensitive elements that are widely used in geochemical studies. Enrichment factors of U and V change from ~3 to <2 and >30 to <20, in the phosphatic and non-phosphatic zone, respectively. These trends are directly opposite to those of Mo_{EN} and Re_{EN} (PAPER III—Lumiste et al., 2021), which would suggest anoxic conditions (Bennett and Canfield, 2020; Tribovillard et al., 2012, 2006) during phosphogenesis.

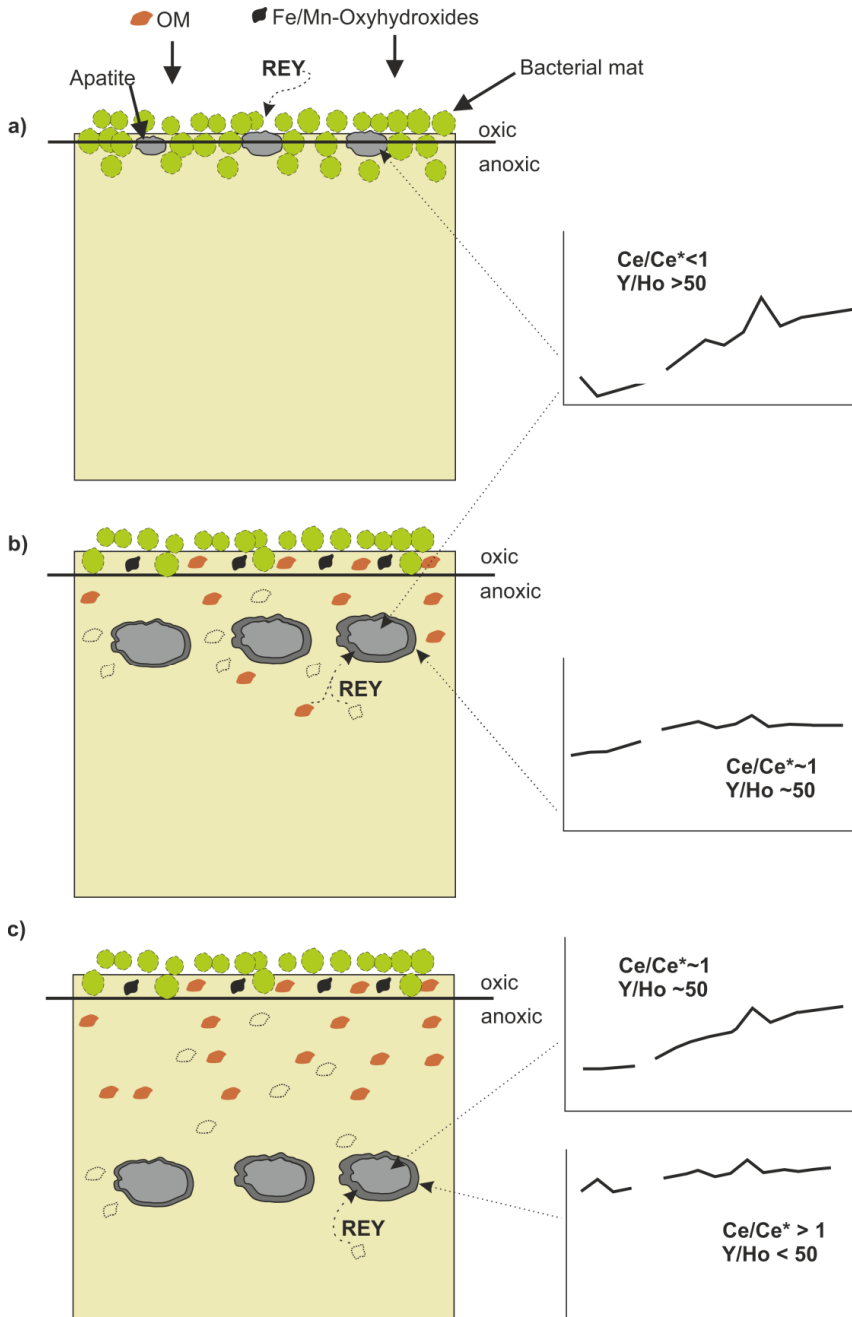


Figure 16. Conceptual model of changes in apatitic grain REE+Y composition during diagenesis. (a) During initial precipitation, REE+Y are incorporated from oxic sea water or very shallow pore water; (b) under suboxic-sulfidic conditions, REE+Y are incorporated to the exterior layers of the grain from suboxic-sulfidic pore water while still displaying some seawaterlike features (HREE enrichment and high Y/Ho ratios); (c) after longer periods of exposure to suboxic-sulfidic pore water, the enrichment zone develops a shale-like pattern with a positive Ce anomaly, while the interior acquires a higher LREE/HREE ratio and lower Y/Ho values (PAPER II—Lumiste et al., 2019).

The authigenic enrichment of V occurs via a two-step process in the sediments—under suboxic conditions, V^{5+} is reduced to V^{4+} (Wu et al., 2019), which is further reduced to highly insoluble V^{3+} under sulphidic conditions (Wanty and Goldhaber, 1992). Similarly, U enrichment occurs via the reduction of soluble U(VI) to insoluble U(IV), as well as its subsequent uptake under reducing conditions (e.g., Barnes and Cochran, 1990). However, the peculiar mismatch between the enrichment trends of Mo_{EN} , Re_{EN} , V_{EN} and U_{EN} suggests an alternative enrichment pathway for some of the trace elements. Both U and V are common structural substitutes in apatite. U^{4+} replaces Ca^{2+} in the apatite structure, whereas V is incorporated via isomorphous substitution of tetrahedrally coordinated trivalent orthovanadate (VO_4^{3-}) for PO_4^{3-} (Pan and Fleet, 2002). Both V and U are highly correlated with P concentrations (PAPER III—Lumiste et al., 2021; $r = +0.94$, p -value < 0.01 , $n = 18$; $r = +0.97$, p -value < 0.01 , $n = 18$ for V_{EN} -P and U_{EN} -P, respectively). Hence, the enrichment in V and U is caused by the enhanced sequestering of these elements by apatite, and not the changes in redox conditions. Furthermore, geochemical proxies related to U and V (e.g., $V/(V+NI)$, V/Cr , Th/U) can lead to erroneous conclusions when utilized in studies of phosphatic sediments (PAPER III—Lumiste et al., 2021b).

In addition to V and U, Mn enrichment does not reflect the sedimentary redox conditions of Core 25005 either. The redox cycle of Mn is dissimilar to typical RSE—under oxic conditions, manganese forms solid Mn-oxhydroxides (Tribovillard et al., 2006), but it is converted to mobile Mn^{2+} when reaching the redox-cline. Due to the high solubility of reduced Mn^{2+} , sulfidic-suboxic sediments tend to be depleted in Mn (Tribovillard et al., 2006), Mn/Al ratios significantly lower than 0.01 being indicative of reducing conditions (Osborne et al., 2017). In Core 25005, Mn/Al ratios are around 0.01–0.02 and 0.006 for the phosphatic and non-phosphatic parts of the core, respectively, which are in line with the interpreted redox history of the core. However, similarly to U and V, Mn is a common substitute in apatite, replacing Ca in the structure (Pan and Fleet, 2002). In addition, P and Mn show a strong correlation with each other ($r = +0.88$, p -value < 0.01 , $n = 18$). The enrichment of Mn seems to be primarily controlled by the presence of apatite. Similarly to V- and U-based proxies, proxies utilizing Mn can lead to inaccurate conclusions regarding the redox conditions of the sediment as well (PAPER III—Lumiste et al., 2021).

7. REE+Y DISTRIBUTION IN EARLY PALEOZOIC SHELLY PHOSPHORITES

7.1. Petrography

The apatitic phases in the Early Paleozoic phosphorites of Estonia are represented by, in order of relative abundance: (I) complete or fragmented phosphatic brachiopod shells, (II) allochthonous phosphatic clasts and (III) *in-situ* grain coatings (Fig. 17a–c). The brachiopod shells vary in size, ranging from ~100 μm fragments to nearly intact valves >1 cm in size (Fig. 17). Some shells show signs of plastic deformation (Fig. 17f).

The internal structure of shells is made up of two types of apatite—compact laminae composed of tightly packed crystallites and baculate laminae composed of trellised apatitic rods (bacula; Fig. 17e) (PAPER IV—Lumiste et al., 2021a). Alternating fossilized compact and baculate laminae represent the inner structure of the extant lingulate brachiopod shells that were deposited as highly mineralized laminae alternating with laminae rich in organic matrix (Williams and Cusack, 2007, 1999). The compact laminae are composed of apatite nanocrystals secreted by the animals. During the lifetime of the brachiopod, the apatitic rods of baculate laminae were enmeshed into an organic matrix (Williams and Cusack, 1999; Lang et al., 2011; Lang et al., 2016).

Shells also contain diagenetic pyrite or hematite (Fig. 17g–h). The baculate layers of brachiopods are typically intergrown with diagenetic pyrite (Fig. 17g), giving the shells a distinct dark hue. Shells from Kabala locality contain hematite instead of pyrite (Fig. 17h), giving them a distinct pale to reddish colour. Phosphatic clasts consist of angular to sub-angular silt, to fine sand-sized quartz grains embedded in phosphatic/calcitic cement (Fig. 17c). Additionally, some clasts contain remnants of brachiopod shells (Fig. 17d). In addition to shells and clasts, some sand grains are overgrown by *in-situ* phosphatic grain coatings (Fig. 17c).

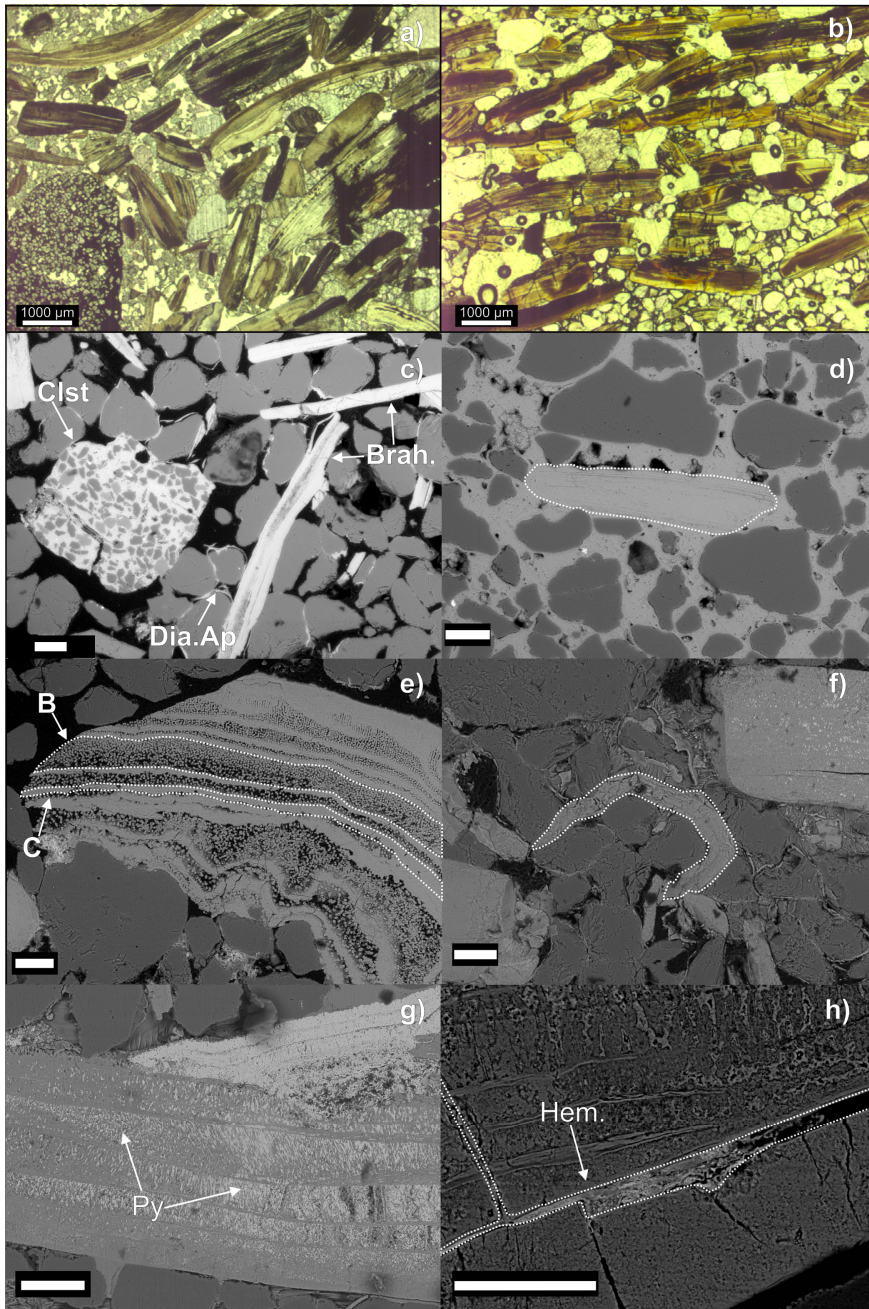


Figure 17. Optical and backscattered scanning electron microscope images: (a) complete shells and a phosphatic clast, (b) fragmented shells, (c) different apatite phases in phosphorite (Clst—phosphatic clast, Brah—brachiopod shells. Dia.AP—diagenetic apatite grain coatings), (d) the remnant of a brachiopod shell inside a phosphatic clast, (e) two distinct apatite laminae present in brachiopod shells (B—mostly authigenic baculate laminae, C—diagenetically altered compact lamina), (f) brachiopod shell showing signs of plastic deformation, (g) brachiopod shell intergrown with diagenetic pyrite (Py), (h) secondary hematite (Hem) inside a fractured shell. Scale bars represent 100 μm for SEM images, 1000 μm for optical microscopy images (PAPER IV—Lumiste et al., 2021a)

7.2. REE+Y concentrations and distribution in phosphatic shells

Measured REE concentrations in the Paleozoic shelly phosphorites of Estonia vary from 162.7 to 2415.3 mg/kg. Similarly to Namibian apatitic grains, the distribution of REE+Y within the phosphatic shells is variable, with the highest REE+Y found in the outer surfaces and margins of the shells (Fig. 18). In addition to the spatial variability within shells, significant differences in REE+Y concentrations between the compact and baculate laminae are present, with compact laminae showing up to tenfold higher concentrations (Fig. 19). In contrast to REE+Y, U is more enriched in the baculate layers (see Fig. 6 in PAPER IV—Lumiste et al., 2021a).

Considerable variation in REE+Y concentrations is also evident in samples from different localities as the samples from the Saka locality show about tenfold enrichment in REE+Y relative to PAAS, compared to the near-PAAS values in the Kabala locality (Fig. 20). In most cases, PAAS-normalized patterns of the phosphatic shells show clear MREE-enrichment, with an average BSI of 1.55, but less so in the shells from Maardu and Kabala locations. BSI and $\sum\text{REE}$ show moderate correlation ($r = 0.61$), with the highest BSI values corresponding to the highest REE concentrations (see Fig. 8 in PAPER IV—Lumiste et al., 2021a). At the same time, Eu/Eu^* values are remarkably stable in all samples, ranging from 0.79 to 1.05. Ce/Ce^* ratios range from 0.72 to 1.04, but there is only one instance of a negative Ce-anomaly that could be classified as a “true anomaly” (Fig. 21a). Y/Ho ratios range significantly from 31.6 to 50.5 (Fig. 21b) and average $\text{La}_\text{N}/\text{Yb}_\text{N}$, $\text{Sm}_\text{N}/\text{Yb}_\text{N}$ and $\text{La}_\text{N}/\text{Nd}_\text{N}$ ratios are 1.02, 1.43, 0.85, respectively (PAPER IV—Lumiste et al., 2021a). A significant difference between Estonian phosphorites and Namibian grains is that the principal shape of PAAS-normalized patterns does not substantially change with increasing or decreasing REE+Y concentrations in the Estonian phosphorites (Fig. 20).

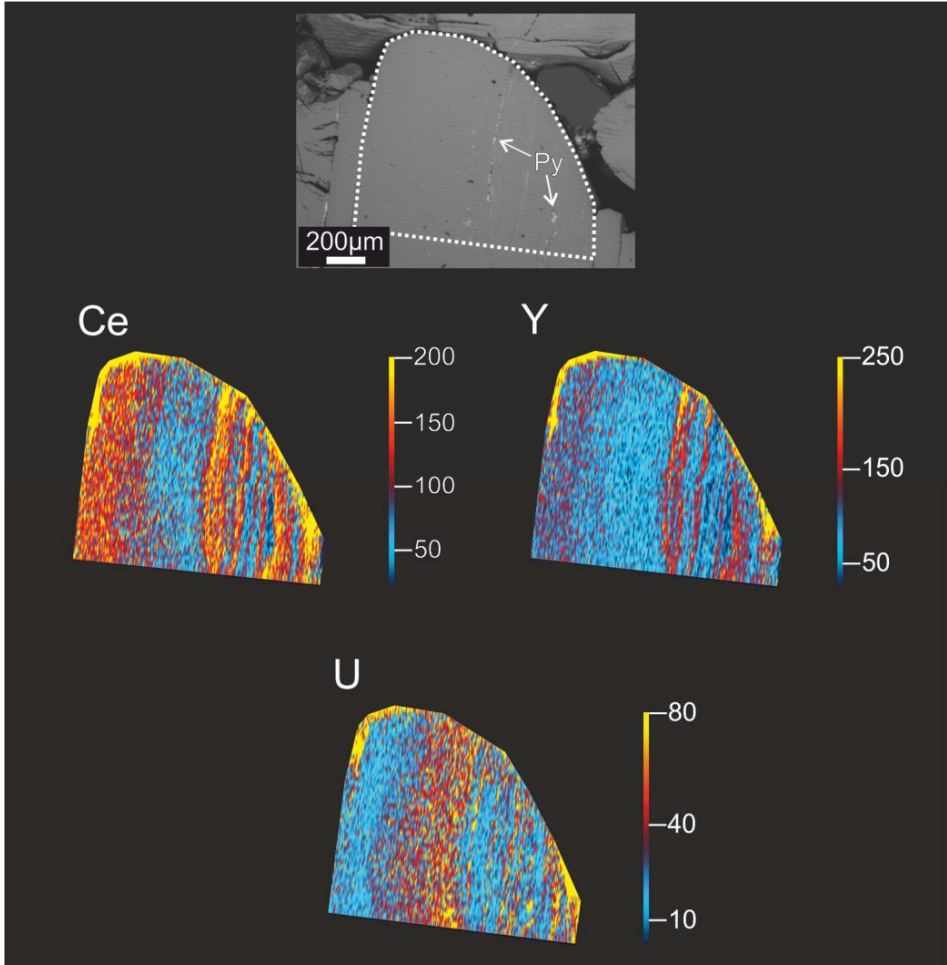


Figure 18. Backscattered scanning electron microscopy image (top) of a brachiopod shell and element distribution maps measured by LA-ICP-MS from the area indicated by a dashed line on the BSE image. The concentrations are semi-quantitative. All scale bars are in mg/kg (PAPER IV—Lumiste et al., 2021a).

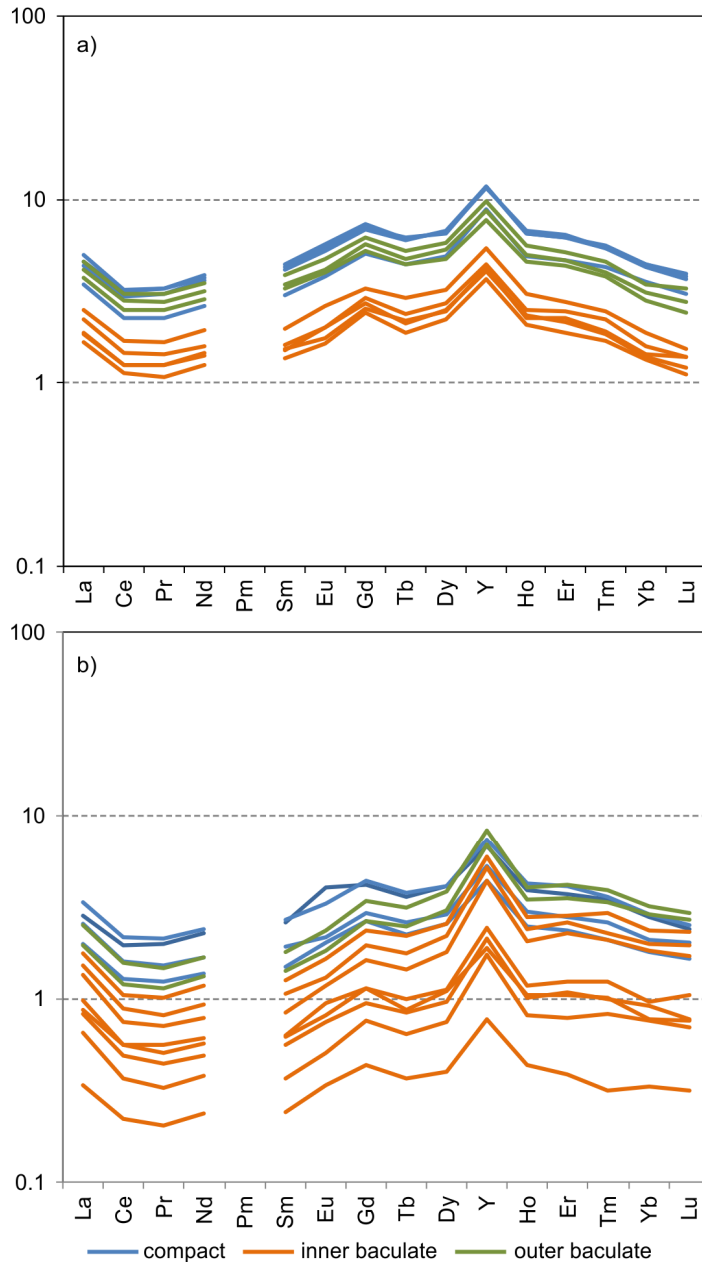


Figure 19. PAAS-normalized REE+Y patterns measured from a single (a) *Ungula inornata* and (b) *Ungula ingrlica* shell. Both shells are from the Maardu locality (PAPER IV—Lumiste et al., 2021a).

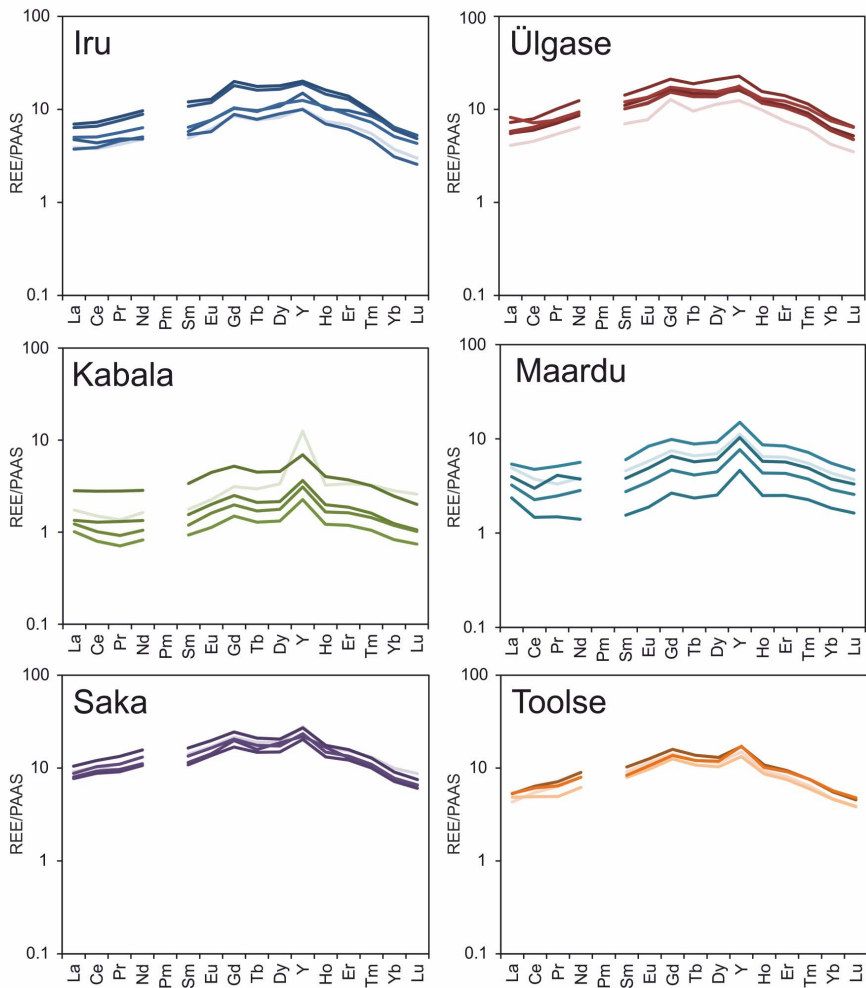


Figure 20. PAAS-normalized REE+Y patterns of phosphorite samples from different localities measured by ICP-MS (PAPER IV—Lumiste et al., 2021a).

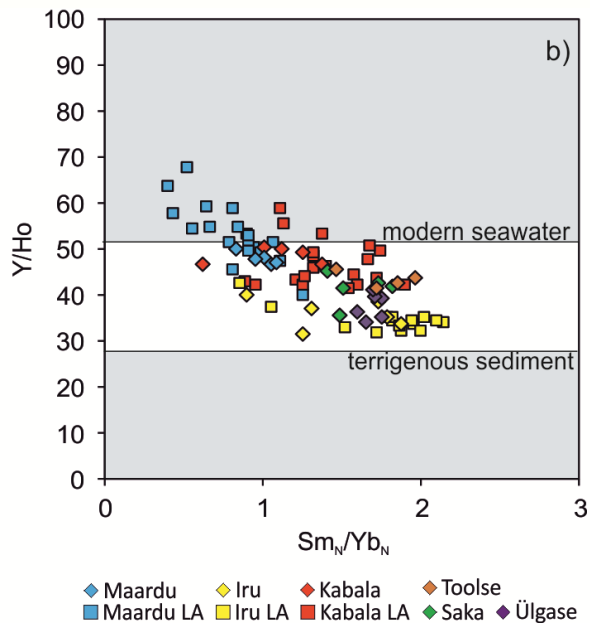
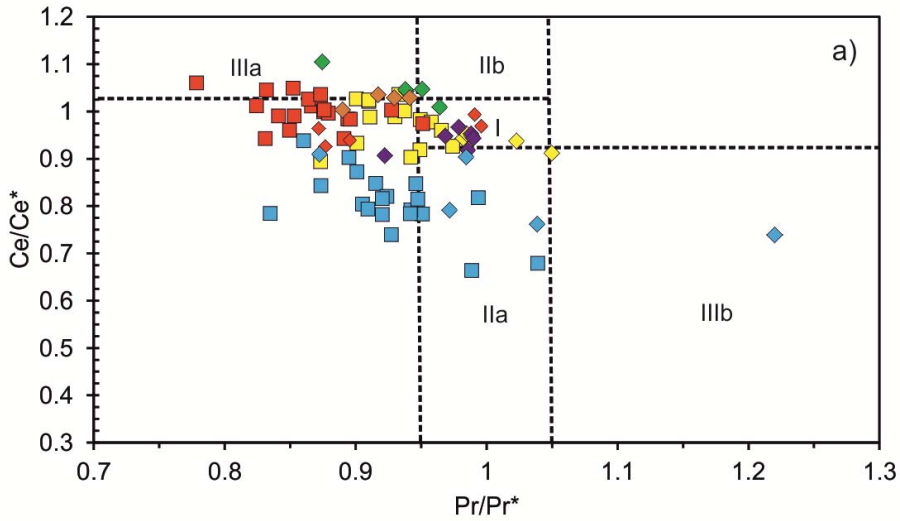


Figure 21. Ce-anomalies (a) and Y/Ho (b) ratios in studied samples. Figure A is modified after Bau and Dulski (1996). Field I—no La or Ce anomalies. Fields IIa and IIb—apparent negative and positive Ce-anomaly, respectively, Fields IIIa and IIIb—true positive and true negative Ce anomaly, respectively. Figure B is modified after Kocsis et al. (2016). “Locality LA” denotes laser ablation measurements, “locality” are ICP-MS measurements (PAPER IV—Lumiste et al., 2021a).

7.3. REE+Y uptake and variability in Estonian shelly phosphorite

The REE content in extant linguliform brachiopods is very low with $\sum\text{REE}$, typically being around 1 mg/kg and rarely as high as 10 mg/kg (Lécuyer et al., 1998; Shaw and Wasserburg, 1985). The $\sum\text{REE}$ concentration in Estonian shelly phosphorites reaches values of >2000 mg/kg. It is well established that such vast enrichment with factors of more than 10^7 compared to seawater is driven by diagenetic processes (Shields and Webb, 2004).

Seawater is considered to be a common source of REEs for bioapatites (e.g., Girard and Lécuyer, 2002; Herwartz et al., 2013; Reynard et al., 1999). Numerous studies have shown that the composition of bioapatite is already significantly modified after shallow burial and most of the REE+Y is taken up during early diagenetic open-system processes where elevated pore water REE+Y concentrations are sourced from clays, organic matter mineralization and Fe-Mn oxyhydroxide reduction (Chen et al., 2015; Herwartz et al., 2013; Zhao et al., 2013; Zhang et al. 2016; Deng et al., 2017; Abbott et al., 2019). Interestingly, while enrichments that do not exceed the 10^7 threshold compared to seawater concentrations tend to take up REE+Y from seawater without significant fractionation (i.e., the shape of the typical seawater pattern is preserved), a distinct bell-shaped MREE-enrichment typically evolves in apatites with higher REE values, controlled by apatite bulk crystal-chemical properties, which cause preferential uptake of MREE during extensive diagenetic alteration (Reynard et al., 1999).

In Estonian shelly phosphorite, shells' compact laminae tend to show higher REE+Y concentration than the baculate laminae (Fig. 19; PAPER IV—Lumiste et al., 2021a), which could stem from a more effective uptake of REE+Y due to the higher surface area of the nanometer-sized apatite crystallites in the compact laminae (PAPER IV—Lumiste et al., 2021a). However, the highest concentrations of REE+Y are located in the exterior of the shells, regardless of the structural type of apatite (Figs. 18–19).

In contrast, U content is remarkably higher in the baculate laminae of phosphatic shells. U is mostly taken up into apatite structure as U^{4+} , via substitution with Ca^{2+} (Pan and Fleet, 2002). As U^{4+} is the dominant species in reduced depositional environments (Barnes and Cochran, 1990), and the phosphatization of baculate laminae is possibly tied to the mineralization of organic matter and the establishment of (at least) locally reduced environments required for the stabilization of pyrite, U in Estonian shelly phosphorite was fixed in the baculate laminae of shell structure during early diagenesis.

Similar spatial heterogeneity in REE+Y distribution in the Recent apatitic grains of Namibia (PAPER II—Lumiste et al., 2019) and Early Palaeozoic shelly phosphorites (PAPER IV—Lumiste et al., 2021a) point towards similar REE+Y enrichment processes—the uptake from pore water is more efficient at the exterior of the shells/grains and the extent of enriched zones is limited by inhibited diffusion between shell/grain centres and pore water. However, dissimilarly to

the variable REE+Y patterns of Namibian Recent apatitic grains (PAPER II—Lumiste et al., 2019), the PAAS-normalized REE+Y patterns of Early Paleozoic phosphorites show remarkable uniformity within a single phosphatic shell (Fig. 19) as well as within a single locality (Fig. 20), suggesting that a (quasi)-equilibrium has been attained between the diagenetic environment and the shells.

Whereas REE+Y patterns are remarkably similar within a locality, they vary significantly between Estonian shelly phosphorite localities (Fig. 20). Phosphorites of the Saka locality contain up to 14 times more REE+Y than those of Kabala, despite similar host rock and diagenetic history (PAPER IV—Lumiste et al., 2021a).

The REE+Y patterns of sedimentary phosphorites can be broadly divided into three distinct types: (I) seawater-like patterns with negative Ce anomalies, high Y/Ho ratios and HREE-enrichment (Emsbo et al., 2015; Shields and Stille, 2001), (II) shale-like patterns with small or absent Ce-anomalies, near-chondritic Y/Ho ratios and little to no HREE-enrichment (Emsbo et al., 2015; PAPER II—Lumiste et al., 2019; McArthur and Walsh, 1984) and (III) bell-shaped patterns, with significant MREE enrichment and no Ce anomaly. The REE concentrations are typically the lowest in seawater-like patterns and the highest in bell-shaped patterns. Development of the bell shape is controlled by preferential uptake of MREE by apatite due to its crystal-chemical properties, typically indicative of extensive diagenetic alteration (Reynard et al., 1999).

PAAS-normalized patterns of REE+Y enriched Saka phosphorites are characterized by MREE-enrichment (with an average BSI of 1.6), whereas in the Kabala samples, BSI is around 1.36 while REE+Y patterns are the most shale-like (Figs. 20). BSI and $\sum\text{REE}$ show moderate correlations ($r = 0.61$), with the highest BSI values corresponding to the highest REE concentrations, pointing towards a diagenetic source for the REE+Y (PAPER IV—Lumiste et al., 2021a).

The up to tenfold difference in REE concentrations of shells from different localities, located just around 20 km apart, could have been caused both by syn-depositional and early diagenetic processes (e.g., input of REE+Y carrying phases, sedimentary environment), and/or post-depositional processes (e.g., metamorphism, weathering, hydrothermal alteration) (Bau, M., 1991; Bonnand et al., 2020). The large-scale redistribution of REE+Y is rare, mainly dependent on the stability of the host phases during late-stage diagenesis and metamorphism (Chakrabarti et al., 2007; Ohr et al., 1994). Given that the northern Baltica Paleobasin has experienced only limited hydrothermal activity (Eensaar et al., 2017; Gaškov et al., 2017; Somelar et al., 2010) and that the conodonts from the Kallavere Formation are very well preserved ($\text{CAI} < 1.5$; Heinsalu et al., 2003), as well as that there is no $\text{Eu}^{2+}/\text{REE}^{3+}$ decoupling (average $\text{Eu}/\text{Eu}^* = 0.94$; PAPER IV—Lumiste et al., 2021a), the variability of REE+Y concentrations likely result from syn-depositional and/or early diagenetic processes (PAPER IV—Lumiste et al., 2021a).

There is a difference in the appearance of shells with different REE+Y content—dark brown to black shells are higher in $\sum\text{REE}$ while light brown pale to reddish shells are characteristic of localities with lower $\sum\text{REEs}$. The colouring

of the shells is due to the presence of secondary pyrite or hematite in black and pale-reddish shells, respectively. Diagenetic pyrite impregnating shell structures is a common secondary phase in phosphorites' northern and western facies, whereas in the Kabala area the pyrite is largely absent while hematite is the dominant Fe-containing phase (Puura and Nemliher, 2001). The Fe speciation in shells likely reflects the redox state of pore water during early diagenesis—pyrite inter-grown brachiopods were deposited under reducing SWI conditions, whereas the presence of hematite is indicative of oxic to suboxic pore water conditions. Alternatively, hematite could be the result of the oxidation of primary diagenetic pyrite by percolating meteoric water.

On one hand, the remobilization of REE by meteoric water could explain the much lower $\sum\text{REE}$ values in the “hematitic” shells from Kabala phosphorites. Deep ground-waters are characterized by REE+Y concentrations in the range of ng/L, even if they are influenced by REE-rich lithologies, (Munemoto et al., 2015). These low concentrations would likely allow at least some of the REE+Y to be leached out of the apatite, resulting in REE+Y depletion from the surfaces of shells and phosphatic pebbles. On the other hand, the elemental distributions in the shells from Kabala phosphorite locality show that the highest REE+Y concentrations are found in the outer margin of the shells instead (Fig. 18). This is more in line with diagenetic REE+Y uptake (e.g., PAPER II—Lumiste et al., 2019) rather than the leaching and removal of these elements. It can therefore be suggested that lower $\sum\text{REE}$ values in Kabala do not result from the secondary mobilization and depletion of these elements, but from limited REE+Y uptake/availability during diagenesis at or near the SWI instead.

It is interesting that the REE+Y content is particularly low in the shells of the southernmost part of the phosphorite deposit, where overlying black shale (“graptolite shale”) of the Türisalu Formation is missing in the stratigraphy and the Kallavere Formation is directly overlain by the glauconitic sand- and siltstones of the Leetse Formation. It is possible that post-depositional remobilization of REE from overlying black shales, documented in other basins (e.g., Lev and Filer, 2004), could be the potential REE+Y source for phosphatic shells. This would explain the substantial heterogeneity of REE+Y concentrations of different localities. The shell-bearing quartz sandstones of the Kallavere Formation themselves were deposited in a hydrodynamically active setting and do not contain significant clay/mud material. Hence, they constitute a poor (internal) source for REE+Y. However, the REE+Y in the lenses of black shales intercalating the sandstones of Kallavere Formation and particularly in the organic-rich mudstones of the overlying Türisalu Formation could have been mobilized during early diagenesis and taken up by phosphatic shells.

Alternatively, the highly location-specific variability of REE+Y concentrations in Estonian shelly phosphorite could have been controlled by the availability of these elements in the surrounding contemporary seawater and/or pore fluids right after deposition. The REE+Y concentrations in modern marine settings differ between near-shore margins, slope and basin settings (Deng et al., 2017). Furthermore, pore water REE+Y conditions also vary significantly, depending on

sediment depth and redox (Abbott et al., 2015; Deng et al., 2017; Haley et al., 2004). Both the processes controlling the increase (i.e., Fe-Mn oxyhydroxide and organic matter dissolution) and decrease (e.g., authigenic apatite formation) of pore water REE+Y concentrations are redox-dependent and the highest flux of REE+Y are related to anoxia (Deng et al., 2017).

During the Early Paleozoic, the northern part of the Baltica paleocontinent was a meridionally oriented shallow epicontinental sea, influenced by upwelling (Hiller, N., 1993; Lécuyer et al., 1998; Parrish et al., 1986), situated at high to intermediate southern latitudes (Torsvik et al., 2012), analogous to modern day Namibian Shelf. Poikiloxia, which is prevalent on the modern Namibian shelf (Algeo and Li, 2020; Bailey and Chapman, 1991; Brüchert et al., 2006), could have played a key role in the variability of REE+Y in phosphorites. The mosaic REE+Y distribution in phosphorites could be the result of variable sedimentary redox conditions during their formation, with high REE+Y concentrations related to phosphorites deposited under anoxic conditions and REE+Y poor phosphorites deposited under (sub)oxic conditions.

8. CONCLUSIONS

This thesis characterized Recent and Early Paleozoic sedimentary phosphorites, studying their geochemical fingerprints by tracking the mechanisms and environmental conditions of their formation and subsequent diagenesis.

The aims of the thesis were to (I) constrain the (bio)geochemical conditions controlling the phosphogenesis on the modern Namibian Shelf and (II) to study the diagenetic effects on REE+Y composition in biogenic Early Palaeozoic shelly and Recent sedimentary apatites. Although phosphorus is a key building block for life on Earth, many aspects of the phosphorus cycle have remained poorly understood. Modern phosphorites are formed on continental shelves influenced by the upwelling of nutrient-rich deep waters. The upwelling leads to a high rate of primary production, which, in turn, leads to the development of sharp and shallow redoxcline in the sediments of the shelf. However, gradients are not temporally stable, but rather fluctuate rapidly both spatially and stratigraphically. Conditions near the SWI can alternate between (sub)oxic and sulfidic. Such dynamic conditions allow for the large sulphur bacteria (LSB) and other polyphosphate metabolizing microorganisms to increase the interstitial phosphate concentrations to levels necessary for Ca-phosphate minerals' precipitation.

However, even if the conditions for Ca-phosphate supersaturation and suitable nucleation templates for phosphogenesis are present, precipitation may not occur as phosphate can diffuse to the overlying water column. Close association between organic polymeric macromolecules and apatite in Namibian phosphatic sediments suggests that biofilm and bioorganic matter are important drivers of the primary nucleation of apatite. Still, phosphogenesis is closely tied to the fluctuating redox conditions.

The behaviour of redox proxies within the Recent Namibian phosphatic sediment succession indicates a shift from anoxic/sulfidic conditions towards suboxia, coinciding with intense apatite precipitation. The presence of small amounts of pyrite in the phosphatic sediments point towards transient sulfidic conditions in predominantly suboxic pore system. This type of fluctuating redox allows efficient operation of the bacterial P-pump by providing all the necessary chemical reactants for sulphide oxidation and polyphosphate metabolization. The involvement of LSB is implied by slightly lower than seawater sulphate PAS $\delta^{34}\text{S}$ values. However, only a small quantity of sulphate in the apatite structure is of bacterial origin, whereas the dominant source was likely seawater. The near-seawater PAS $\delta^{34}\text{S}$ values, coupled with high Y/Ho ratios and negative Ce-anomalies in the centre of concretionary apatite grains suggest that the primary precipitation of apatite must occur in an environment carrying an oxic seawater signal. Collectively, (I) dominantly suboxic conditions, (II) punctuated by short-term sulfidic conditions, and (III) organic matter derived nucleation surfaces control both the depth and spatial distribution of phosphogenesis. Apatite efficiently sequesters U, V and Mn, leading to anomalous values in the concentrations of these elements in the phosphatic zone of the core. Caution is advised when utilizing redox proxies

based on U, V and Mn while studying sediments containing substantial amounts of apatite.

The REE+Y concentrations in sedimentary apatite display systematic behaviour during precipitation and subsequent diagenesis. The primary seawater-like composition of REE+Y in apatitic grains is readily overprinted by the uptake from suboxic-sulfidic pore water on very short timescales through water-rock interactions. The REE+Y form ~20 µm wide enrichment zones in the periphery of the grains, although small amounts of REE+Y are also diffused to the grain centres, altering the REE+Y composition of the whole grain. Reworked pelletal apatitic grains show distinctly different REE+Y patterns and ratios from the *in-situ* concretionary grains, indicating continuous uptake of these elements. Hence, the usefulness of REE+Y patterns of sedimentary apatites as proxies for past seawater and redox conditions is questionable.

While the REE+Y composition of Recent sedimentary apatite is highly dependent on the sedimentological and geochemical history of apatitic grains, the REE+Y composition of Early Paleozoic Estonian shelly phosphorites display systematic REE+Y differences both within a single lingulate brachiopod shell and between different localities. The shells, which are the dominant apatite-carrying constituents in the Estonian phosphorite, are primarily composed of alternating phosphatic compact and baculate laminae. Compact laminae representing skeletal apatite secreted by an animal contain more REE+Y, possibly due to the larger surface area of the nanocrystalline apatite aggregate composing the compact lamina. Baculate laminae, which are mostly composed of authigenic apatite formed by the transformation of apatite-organic matrix, contain significantly less REE+Y. However, regardless of the shells' lamina type, the most enriched regions of the shells are in their outer surfaces, analogous to the Namibian apatitic grains to diagenetic up-take of REE+Y. However, the principal shape of the PAAS-normalized REE+Y patterns measured in different regions of a single shell are similar, suggesting that a (quasi-)equilibrium has been achieved. Similarly, different shells from the same locality show remarkably coherent REE+Y patterns. Dissimilarly, stark differences between different localities exists, with up to tenfold REE+Y abundance variability between localities only around 20 kilometres apart.

The Early Paleozoic Baltica paleocontinent was analogous to modern day Namibian Shelf, where poikiloxia is prevalent. The significant differences in REE+Y concentrations between localities could have stemmed from different redox conditions during early diagenesis, with anoxia leading to a higher degree of enrichment, compared to REE+Y-poor shells deposited under oxic conditions.

REFERENCES

- Abbott, A.N., Haley, B.A., McManus, J., Reimers, C.E., 2015. The sedimentary flux of dissolved rare earth elements to the ocean. *Geochim. Cosmochim. Acta* 154, 186–200. <https://doi.org/10.1016/j.gca.2015.01.010>
- Abbott, A.N., Löhner, S., Trethewey, M., 2019. Are Clay Minerals the Primary Control on the Oceanic Rare Earth Element Budget? *Front. Mar. Sci.* 6, 1–19. <https://doi.org/10.3389/fmars.2019.00504>
- Algeo, T.J., Ingall, E., 2007. Sedimentary Corg:P ratios, paleocean ventilation, and Phanerozoic atmospheric pO₂. *Palaeogeogr. Palaeoclimatol. Palaeoecol.* 256, 130–155. <https://doi.org/10.1016/j.palaeo.2007.02.029>
- Algeo, T.J., Li, C., 2020. Redox classification and calibration of redox thresholds in sedimentary systems. *Geochim. Cosmochim. Acta*. <https://doi.org/10.1016/j.gca.2020.01.055>
- Alibo, D.S., Nozaki, Y., 1999. Rare earth elements in seawater: Particle association, shale-normalization, and Ce oxidation. *Geochim. Cosmochim. Acta* 63, 363–372. [https://doi.org/10.1016/S0016-7037\(98\)00279-8](https://doi.org/10.1016/S0016-7037(98)00279-8)
- Álvaro, J.J., Shields-Zhou, G.A., Ahlberg, P., Jensen, S., Palacios, T., 2016. Ediacaran–Cambrian phosphorites from the western margins of Gondwana and Baltica. *Sedimentology* 63, 350–377. <https://doi.org/10.1111/sed.12217>
- Arning, E.T., Birgel, D., Brunner, B., Peckmann, J., 2009a. Bacterial formation of phosphatic laminites off Peru. *Geobiology* 7, 295–307. <https://doi.org/10.1111/j.1472-4669.2009.00197.x>
- Arning, E.T., Lückge, A., Breuer, C., Gussone, N., Birgel, D., Peckmann, J., 2009b. Genesis of phosphorite crusts off Peru. *Mar. Geol.* 262, 68–81. <https://doi.org/10.1016/j.margeo.2009.03.006>
- Artyushkov, E.A., Lindström, M., Popov, L.E., 2000. Relative sea-level changes in Baltoscandia in the Cambrian and early Ordovician: The predominance of tectonic factors and the absence of large scale eustatic fluctuations. *Tectonophysics* 320, 375–407. [https://doi.org/10.1016/S0040-1951\(00\)00038-X](https://doi.org/10.1016/S0040-1951(00)00038-X)
- Auer, G., Reuter, M., Hauzenberger, C.A., Piller, W.E., 2017. The impact of transport processes on rare earth element patterns in marine authigenic and biogenic phosphates. *Geochim. Cosmochim. Acta* 203, 140–156. <https://doi.org/10.1016/j.gca.2017.01.001>
- Bailey, G.W., Chapman, P., 1991. Short-term variability during an anchor station study in the southern Benguela upwelling system: Chemical and physical oceanography. *Prog. Oceanogr.* 28, 9–37. [https://doi.org/10.1016/0079-6611\(91\)90019-I](https://doi.org/10.1016/0079-6611(91)90019-I)
- Barnes, C.E., Cochran, J.K., 1990. Uranium removal in oceanic sediments and the oceanic U balance. *Earth Planet. Sci. Lett.* 97, 94–101. [https://doi.org/10.1016/0012-821X\(90\)90101-3](https://doi.org/10.1016/0012-821X(90)90101-3)
- Baturin, G.N., 2000. Formation and Evolution of Phosphorite Grains and Nodules on the Namibian Shelf, from Recent to Pleistocene, in: Glenn, C.R., Prévôt-Lucas, L., Lucas, J. (Eds.), *Marine Authigenesis: From Global to Microbial*. SEPM Society for Sedimentary Geology.
- Baturin, G.N., Ilyin, A. V., 2013. Comparative geochemistry of shell phosphorites and dictyonema shales of the Baltic. *Geochemistry Int.* 51, 23–32. <https://doi.org/10.1134/S0016702913010023>

- Bau, M., 1999. Scavenging of dissolved yttrium and rare earths by precipitating iron oxyhydroxide: Experimental evidence for Ce oxidation, Y-Ho fractionation, and lanthanide tetrad effect. *Geochim. Cosmochim. Acta* 63, 67–77.
[https://doi.org/10.1016/S0016-7037\(99\)00014-9](https://doi.org/10.1016/S0016-7037(99)00014-9)
- Bau, M., 1991. Rare-earth element mobility during hydrothermal and metamorphic fluid-rock interaction and the significance of the oxidation state of europium. *Chem. Geol.* 93, 219–230. [https://doi.org/10.1016/0009-2541\(91\)90115-8](https://doi.org/10.1016/0009-2541(91)90115-8)
- Bau, M., Balan, S., Schmidt, K., Koschinsky, A., 2010. Rare earth elements in mussel shells of the Mytilidae family as tracers for hidden and fossil high-temperature hydrothermal systems. *Earth Planet. Sci. Lett.* 299, 310–316.
<https://doi.org/10.1016/j.epsl.2010.09.011>
- Bau, M., Dulski, P., 1996. Distribution of yttrium and rare-earth elements in the Penge and Kuruman iron-formations, Transvaal Supergroup, South Africa. *Precambrian Res.* 79, 37–55. [https://doi.org/10.1016/0301-9268\(95\)00087-9](https://doi.org/10.1016/0301-9268(95)00087-9)
- Bau, M., Koschinsky, A., 2009. Oxidative scavenging of cerium on hydrous Fe oxide: Evidence from the distribution of rare earth elements and yttrium between Fe oxides and Mn oxides in hydrogenetic ferromanganese crusts. *Geochem. J.*
<https://doi.org/10.2343/geochemj.1.0005>
- Bau, M., Möller, P., Dulski, P., 1997. Yttrium and lanthanides in eastern Mediterranean seawater and their fractionation during redox-cycling. *Mar. Chem.* 56, 123–131.
[https://doi.org/10.1016/S0304-4203\(96\)00091-6](https://doi.org/10.1016/S0304-4203(96)00091-6)
- Bennett, W.W., Canfield, D.E., 2020. Redox-sensitive trace metals as paleoredox proxies: A review and analysis of data from modern sediments. *Earth-Science Rev.* 204, 103175.
<https://doi.org/10.1016/j.earscirev.2020.103175>
- Berndmeyer, C., Birgel, D., Brunner, B., Wehrmann, L.M., Jöns, N., Bach, W., Arning, E.T., Föllmi, K.B., Peckmann, J., 2012. The influence of bacterial activity on phosphorite formation in the Miocene Monterey Formation, California. *Palaeogeogr. Palaeoclimatol. Palaeoecol.* 317–318, 171–181.
<https://doi.org/10.1016/j.palaeo.2012.01.004>
- Berner, R.A., Scott, M.R., Thomlinson, C., 1970. Carbonate alkalinity in the pore waters of anoxic marine sediments. *Limnol. Oceanogr.* 15, 544–549.
<https://doi.org/10.4319/lo.1970.15.4.0544>
- Birski, Ł., Słaby, E., Wirth, R., Koch-Müller, M., Simon, K., Wudarska, A., Götze, J., Lepland, A., Hofmann, A., Kuras, A., 2019. Archaean phosphates: a case study of transformation processes in apatite from the Barberton greenstone belt. *Contrib. to Mineral. Petrol.* 174, 1–23. <https://doi.org/10.1007/s00410-019-1560-z>
- Bonnand, P., Lalonde, S. V., Boyet, M., Heubeck, C., Homann, M., Nonnotte, P., Foster, I., Konhauser, K.O., Köhler, I., 2020. Post-depositional REE mobility in a Paleoproterozoic banded iron formation revealed by La-Ce geochronology: A cautionary tale for signals of ancient oxygenation. *Earth Planet. Sci. Lett.* 547, 116452.
<https://doi.org/10.1016/j.epsl.2020.116452>
- Borchers, S.L., Schnetger, B., Böning, P., Brumsack, H.J., 2005. Geochemical signatures of the Namibian diatom belt: Perennial upwelling and intermittent anoxia. *Geochemistry, Geophys. Geosystems* 6. <https://doi.org/10.1029/2004GC000886>
- Bradbury, H.J., Vandeginste, V., John, C.M., 2015. Diagenesis of phosphatic hardgrounds in the Monterey Formation: A perspective from bulk and clumped isotope geochemistry. *Bull. Geol. Soc. Am.* 127, 1453–1463.
<https://doi.org/10.1130/B31160.1>

- Bremner, J.M., Rogers, J., 1990. Phosphorite deposits on the Namibian continental shelf, Phosphate deposits of the world, vol. 3. Neogene to Modern phosphorites. Cambridge University Press; IGCP project 156, phosphorites.
- Briggs, D.E.G., Wilby, P.R., 1996. The role of the calcium carbonate-calcium phosphate switch in the mineralization of soft-bodied fossils. *J. Geol. Soc. London.* 153, 665–668. <https://doi.org/10.1144/gsjgs.153.5.0665>
- Brock, J., Schulz-Vogt, H.N., 2011. Sulfide induces phosphate release from polyphosphate in cultures of a marine *Beggiatoa* strain. *ISME J.* 5, 497–506. <https://doi.org/10.1038/ismej.2010.135>
- Brüchert, V., Currie, B., Peard, K.R., Lass, U., Endler, R., Dübecke, A., Julies, E., Leipe, T., Zitzmann, S., 2006. Biogeochemical and physical control on shelf anoxia and water column hydrogen sulphide in the Benguela coastal upwelling system off Namibia., in: Neretin, L.N. (Ed.), *Past and Present Water Column Anoxia*. Kluwer Academic Publishers, Dordrecht, pp. 161–193. https://doi.org/10.1007/1-4020-4297-3_07
- Brüchert, V., Jørgensen, B.B., Neumann, K., Riechmann, D., Schlösser, M., Schulz, H., 2003. Regulation of bacterial sulfate reduction and hydrogen sulfide fluxes in the central Namibian coastal upwelling zone. *Geochim. Cosmochim. Acta* 67, 4505–4518. [https://doi.org/10.1016/S0016-7037\(03\)00275-8](https://doi.org/10.1016/S0016-7037(03)00275-8)
- Burnett, W.C., 1977. Geochemistry and origin of phosphorite deposits from off Peru and Chile. *Bull. Geol. Soc. Am.* 88, 813–823.
- Burnett, W.C., Roe, K.K., Piper, D.Z., 1983. Upwelling and Phosphorite Formation in the Ocean, in: Suess, E., Thiede, J. (Eds.), *Coastal Upwelling Its Sediment Record: Part A: Responses of the Sedimentary Regime to Present Coastal Upwelling*. Springer US, Boston, MA, pp. 377–397. https://doi.org/10.1007/978-1-4615-6651-9_18
- Byrne, R.H., Sholkovitz, E.R., 1996. Chapter 158 Marine chemistry and geochemistry of the lanthanides. *Handb. Phys. Chem. Rare Earths*. [https://doi.org/10.1016/S0168-1273\(96\)23009-0](https://doi.org/10.1016/S0168-1273(96)23009-0)
- Canfield, D.E., Farquhar, J., Zerkle, A.L., 2010. High isotope fractionations during sulfate reduction in a low-sulfate euxinic ocean analog. *Geology* 38, 415–418. <https://doi.org/10.1130/G30723.1>
- Canfield, D.E., Raiswell, R., Westrich, J.T., Reaves, C.M., Berner, R.A., 1986. The use of chromium reduction in the analysis of reduced inorganic sulfur in sediments and shales. *Chem. Geol.* 54, 149–155. [https://doi.org/10.1016/0009-2541\(86\)90078-1](https://doi.org/10.1016/0009-2541(86)90078-1)
- Cappellen, P. Van, Berner, R.A., 1991. Fluorapatite crystal growth from modified seawater solutions. *Geochim. Cosmochim. Acta* 55, 1219–1234. [https://doi.org/10.1016/0016-7037\(91\)90302-L](https://doi.org/10.1016/0016-7037(91)90302-L)
- Carr, M.-E., 2001. Estimation of potential productivity in Eastern Boundary Currents using remote sensing. *Deep Sea Res. Part II Top. Stud. Oceanogr.* 49, 59–80. [https://doi.org/10.1016/S0967-0645\(01\)00094-7](https://doi.org/10.1016/S0967-0645(01)00094-7)
- Chakrabarti, R., Abanda, P.A., Hannigan, R.E., Basu, A.R., 2007. Effects of diagenesis on the Nd-isotopic composition of black shales from the 420 Ma Utica Shale Magnafacies. *Chem. Geol.* 244, 221–231. <https://doi.org/10.1016/j.chemgeo.2007.06.017>
- Chen, J., Algeo, T.J., Zhao, L., Chen, Z.Q., Cao, L., Zhang, L., Li, Y., 2015. Diagenetic uptake of rare earth elements by bioapatite, with an example from Lower Triassic conodonts of South China. *Earth-Science Rev.* 149, 181–202. <https://doi.org/10.1016/j.earscirev.2015.01.013>

- Chetty, D., Gutzmer, J., 2012. REE redistribution during hydrothermal alteration of ores of the Kalahari Manganese Deposit. *Ore Geol. Rev.* 47, 126–135. <https://doi.org/10.1016/j.oregeorev.2011.06.001>
- Compton, J.S., Bergh, E.W., 2016. Phosphorite deposits on the Namibian shelf. *Mar. Geol.* 380, 290–314. <https://doi.org/10.1016/j.margeo.2016.04.006>
- Compton, J.S., Mulabisana, J., McMillan, I.K., 2002. Origin and age of phosphorite from the Last Glacial Maximum to Holocene transgressive succession off the Orange ... Origin and age of phosphorite from the Last Glacial Maximum to Holocene transgressive succession on the Orange River, South Africa. *Mar. Geol.* 186, 243–261. [https://doi.org/10.1016/S0025-3227\(02\)00211-6](https://doi.org/10.1016/S0025-3227(02)00211-6)
- Crusius, J., Calvert, S., Pedersen, T., Sage, D., 1996. Rhenium and molybdenum enrichments in sediments as indicators of oxic, suboxic and sulfidic conditions of deposition. *Earth Planet. Sci. Lett.* 145, 65–78. [https://doi.org/10.1016/s0012-821x\(96\)00204-x](https://doi.org/10.1016/s0012-821x(96)00204-x)
- Daesslé, L.W., Carriquiry, J.D., 2008. Rare earth and metal geochemistry of land and submarine phosphorites in the Baja California Peninsula, Mexico. *Mar. Georesources Geotechnol.* 26, 340–349. <https://doi.org/10.1080/10641190802382633>
- Dahl, T.W., Chappaz, A., Hoek, J., McKenzie, C.J., Svane, S., Canfield, D.E., 2017. Evidence of molybdenum association with particulate organic matter under sulfidic conditions. *Geobiology* 15, 311–323. <https://doi.org/10.1111/gbi.12220>
- Dale, A.W., Brüchert, V., Alperin, M., Regnier, P., 2009. An integrated sulfur isotope model for Namibian shelf sediments. *Geochim. Cosmochim. Acta* 73, 1924–1944. <https://doi.org/10.1016/j.gca.2008.12.015>
- de Baar, H.J.W., Bacon, M.P., Brewer, P.G., Bruland, K.W., 1985. Rare earth elements in the Pacific and Atlantic Oceans. *Geochim. Cosmochim. Acta* 49, 1943–1959. [https://doi.org/10.1016/0016-7037\(85\)90089-4](https://doi.org/10.1016/0016-7037(85)90089-4)
- de Baar, H.J.W., Bruland, K.W., Schijf, J., van Heuven, S.M.A.C., Behrens, M.K., 2018. Low cerium among the dissolved rare earth elements in the central North Pacific Ocean. *Geochim. Cosmochim. Acta* 236, 5–40. <https://doi.org/10.1016/j.gca.2018.03.003>
- de Baar, H.J.W., Schijf, J., Byrne, R.H., 1991. Solution chemistry of the rare earth elements in seawater. *Eur. J. Solid State Inorg. Chem.* 28, 357–373.
- Deng, Y., Ren, J., Guo, Q., Cao, J., Wang, H., Liu, C., 2017. Rare earth element geochemistry characteristics of seawater and porewater from deep sea in western Pacific. *Sci. Rep.* 7, 1–13. <https://doi.org/10.1038/s41598-017-16379-1>
- Eckardt, F.D., Kuring, N., 2005. SeaWiFS identifies dust sources in the Namib Desert. *Int. J. Remote Sens.* 26, 4159–4167. <https://doi.org/10.1080/01431160500113112>
- Eensaar, J., Gaškov, M., Pani, T., Sepp, H., Somelar, P., Kirsimäe, K., 2017. Hydrothermal fracture mineralization in the stable cratonic northern part of the Baltic Paleobasin: sphalerite fluid inclusion evidence. *Gff* 139, 52–62. <https://doi.org/10.1080/11035897.2016.1196499>
- Elderfield, H., Greaves, M.J., 1982. The rare earth elements in seawater. *Nature* 296, 214–219. <https://doi.org/10.1038/296214a0>
- Emsbo, P., McLaughlin, P.I., Breit, G.N., du Bray, E.A., Koenig, A.E., 2015a. Rare earth elements in sedimentary phosphate deposits: Solution to the global REE crisis? *Gondwana Res.* 27, 776–785. <https://doi.org/10.1016/j.gr.2014.10.008>
- Felitsyn, S., Sturesson, U., Popov, L., Holmer, L., 1998. Nd isotope composition and rare earth element distribution in early Paleozoic biogenic apatite from Baltoscandia: A signature of Iapetus ocean water. *Geology* 26, 1083–1086.

- Filippelli, G.M., 2011. Phosphate rock formation and marine phosphorus geochemistry: The deep time perspective. *Chemosphere* 84, 759–766.
<https://doi.org/10.1016/j.chemosphere.2011.02.019>
- Föllmi, K.B., 1996. The phosphorus cycle, phosphogenesis phosphate-rich deposits 40, 55–124. [https://doi.org/10.1016/0012-8252\(95\)00049-6](https://doi.org/10.1016/0012-8252(95)00049-6)
- Föllmi, K.B., Schöllhorn, I., Ulianov, A., Adatte, T., Spangenberg, J.E., de Kaenel, E., Gertsch, B., Schwennicke, T., Ledesma, M.C., Grimm, K.A., Garrison, R.E., 2019. Phosphogenesis during the Cenozoic transition from greenhouse to icehouse conditions: Upper Oligocene to lower Miocene siliceous, phosphate, and organic-rich sediments near La Purísima, Baja California Sur, Mexico. *Depos. Rec.* 5, 23–52.
<https://doi.org/10.1002/dep2.52>
- Garnit, H., Bouhlel, S., Jarvis, I., 2017. Geochemistry and depositional environments of Paleocene–Eocene phosphorites: Metlaoui Group, Tunisia. *J. African Earth Sci.* 134, 704–736. <https://doi.org/10.1016/j.jafrearsci.2017.07.021>
- Gaškov, M., Sepp, H., Paiste, P., Kirsimäe, K., Pani, T., 2017. Barite mineralization in Kalana speleothems. *Est. J. Earth Sci.* 66, 12.
- Gimmelfarb, B.M., Krasilnikova, N.A., Tushina, A.M., 1959. Classification of phosphorites.
- Glenn, C.R., Arthur, M.A., 1988. Petrology and major element geochemistry of Peru margin phosphorites and associated diagenetic minerals: Authigenesis in modern organic-rich sediments. *Mar. Geol.* 80, 231–267.
[https://doi.org/10.1016/0025-3227\(88\)90092-8](https://doi.org/10.1016/0025-3227(88)90092-8)
- Goldhammer, T., Brüchert, V., Ferdelman, T.G., Zabel, M., 2010. Microbial sequestration of phosphorus in anoxic upwelling sediments. *Nat. Geosci.* 3, 557–561.
<https://doi.org/10.1038/ngeo913>
- Goldstein, S.J., Jacobsen, S.B., 1988. Rare earth elements in river waters. *Earth Planet. Sci. Lett.* 89, 35–47. [https://doi.org/10.1016/0012-821X\(88\)90031-3](https://doi.org/10.1016/0012-821X(88)90031-3)
- Gunnars, A., Blomqvist, S., Martinsson, C., 2004. Inorganic formation of apatite in brackish seawater from the Baltic Sea: An experimental approach. *Mar. Chem.* 91, 15–26.
<https://doi.org/10.1016/j.marchem.2004.01.008>
- Haley, B.A., Klinkhammer, G.P., McManus, J., 2004. Rare earth elements in pore waters of marine sediments. *Geochim. Cosmochim. Acta* 68, 1265–1279.
<https://doi.org/10.1016/j.gca.2003.09.012>
- Heinsalu, H., Kaljo, D., Kurvits, T., Viira, V., 2003. The stratotype of the Orasoja member (Tremadocian, Northeast Estonia): Lithology, mineralogy, and biostratigraphy. *Proc. Est. Acad. Sci. Geol.* 52, 135–154.
- Heinsalu, H., Viira, V., 1997. Pakerort Stage, in: Raukas, A., Teedumäe, A. (Eds.), *Geology and Mineral Resources of Estonia*. Estonian Academy Publishers, Tallinn, pp. 331–336.
- Heinsalu, H., Viira, V., Raudsep, R., 1994. Environmental conditions of shelly phosphorite accumulation in the Rakvere Phosphorite region, Northern Estonia. *Proc. Est. Acad. Sci. Geol.* 43, 109–121.
- Helz, G.R., Vorliceck, T.P., 2019. Precipitation of molybdenum from euxinic waters and the role of organic matter. *Chem. Geol.* 509, 178–193.
<https://doi.org/10.1016/j.chemgeo.2019.02.001>
- Herwartz, D., Tütken, T., Jochum, K.P., Sander, P.M., 2013. Rare earth element systematics of fossil bone revealed by LA-ICPMS analysis. *Geochim. Cosmochim. Acta* 103, 161–183. <https://doi.org/10.1016/j.gca.2012.10.038>

- Hiller, N., 1993. A modern analogue for the Lower Ordovician *Obolus* conglomerate of Estonia. *Geol. Mag.* 130, 265–267. <https://doi.org/10.1017/S0016756800009912>
- Hoetzel, S., Dupont, L.M., Marret, F., Jung, G., Wefer, G., 2017. Steps in the intensification of Benguela upwelling over the Walvis Ridge during Miocene and Pliocene. *Int. J. Earth Sci.* 106, 171–183. <https://doi.org/10.1007/s00531-016-1309-0>
- Hughes, J.M., Rakovan, J., 2002. The Crystal Structure of Apatite, $\text{Ca}_5(\text{PO}_4)_3(\text{F}, \text{OH}, \text{Cl})$. *Rev. Mineral. Geochemistry* 48, 1–12. <https://doi.org/10.2138/rmg.2002.48.1>
- Humphries, M., 2011. Rare earth elements: The global supply chain. *Rare Earth Miner. Policies Issues* 1–20.
- Inthorn, M., Mohrholz, V., Zabel, M., 2006. Nepheloid layer distribution in the Benguela upwelling area offshore Namibia. *Deep. Res. Part I Oceanogr. Res. Pap.* 53, 1423–1438. <https://doi.org/10.1016/j.dsr.2006.06.004>
- Jahnke, R.A., 1984. The synthesis and solubility of carbonate fluorapatite. *Am. J. Sci.* 284, 58–78. <https://doi.org/10.2475/ajs.284.1.58>
- Jahnke, R.A., Emerson, S.R., Roe, K.K., Burnett, W.C., 1983. The present day formation of apatite in Mexican continental margin sediments. *Geochim. Cosmochim. Acta* 47, 259–266. [https://doi.org/10.1016/0016-7037\(83\)90138-2](https://doi.org/10.1016/0016-7037(83)90138-2)
- Jarvis, I., Burnett, W., Nathan, Y., Almbaydin, F., Attia, A.K.M., Castro, L., Flicoteaux, R., Hilmy, M., Yin, V.Q.A.S.A.Z., 1994. Phosphorite geochemistry state-of-the-art and environmental concerns.
- Jochum, K.P., Wilson, S.A., Abouchami, W., Amini, M., Chmeleff, J., Eisenh Bailey, A., Hegner, E., Iaccheri, L.M., Kieffer, B., Krause, J., McDonough, W.F., Mertz-Kraus, R., Raczek, I., Rudnick, R.L., Scholz, D., Steinhöfel, G., Stoll, B., Stracke, A., Tonarini, S., Weis, D., Weis, U., Woodhead, J.D., 2011. GSD-1G and MPI-DING Reference Glasses for In Situ and Bulk Isotopic Determination. *Geostand. Geo-analytical Res.* 35, 193–226. <https://doi.org/10.1111/j.1751-908X.2010.00114.x>
- Johannesson, K.H., Chevis, D.A., Burdige, D.J., Cable, J.E., Martin, J.B., Roy, M., 2011. Submarine groundwater discharge is an important net source of light and middle REEs to coastal waters of the Indian River Lagoon, Florida, USA. *Geochim. Cosmochim. Acta* 75, 825–843. <https://doi.org/10.1016/j.gca.2010.11.005>
- Johannesson, K.H., Palmore, C.D., Fackrell, J., Prouty, N.G., Swarzenski, P.W., Chevis, D.A., Telfeyan, K., White, C.D., Burdige, D.J., 2017. Rare earth element behavior during groundwater–seawater mixing along the Kona Coast of Hawaii. *Geochim. Cosmochim. Acta* 198, 229–258. <https://doi.org/10.1016/j.gca.2016.11.009>
- Joosu, L., Lepland, A., Kirsimäe, K., Romashkin, A.E., Roberts, N.M.W., Martin, A.P., Črne, A.E., 2015. The REE-composition and petrography of apatite in 2Ga Zaonega Formation, Russia: The environmental setting for phosphogenesis. *Chem. Geol.* 395, 88–107. <https://doi.org/10.1016/j.chemgeo.2014.11.013>
- Joosu, L., Lepland, A., Kreitsmann, T., Üpraus, K., Roberts, N.M.W., Paiste, P., Martin, A.P., Kirsimäe, K., 2016. Petrography and the REE-composition of apatite in the Paleoproterozoic Pilgijärvi Sedimentary Formation, Pechenga Greenstone Belt, Russia. *Geochim. Cosmochim. Acta* 186, 135–153. <https://doi.org/10.1016/j.gca.2016.04.043>
- Jorgensen, B.B., 1979. A theoretical model of the stable sulfur isotope distribution in marine sediments. *Geochim. Cosmochim. Acta* 43, 363–374. [https://doi.org/10.1016/0016-7037\(79\)90201-1](https://doi.org/10.1016/0016-7037(79)90201-1)
- Kim, J.-H., Torres, M.E., Haley, B.A., Kastner, M., Pohlman, J.W., Riedel, M., Lee, Y.-J., 2012. The effect of diagenesis and fluid migration on rare earth element distribution

- in pore fluids of the northern Cascadia accretionary margin. *Chem. Geol.* 291, 152–165. <https://doi.org/10.1016/j.chemgeo.2011.10.010>
- Kirsimäe, K., Jorgensen, P., Kalm, V., 1999. Low-temperature diagenetic illite-smectite in Lower Cambrian clays in North Estonia. *Clay Miner.* 34, 151–163. [https://doi.org/DOI 10.1180/claymin.1999.034.1.16](https://doi.org/DOI%2010.1180/claymin.1999.034.1.16)
- Kniep, R., Busch, S., 1996. Biomimetic Growth and Self-Assembly of Fluorapatite Aggregates by Diffusion into Denatured Collagen Matrices. *Angew. Chemie Int. Ed. English* 35, 2624–2626. <https://doi.org/https://doi.org/10.1002/anie.199626241>
- Knudsen, A.C., Gunter, M.E., 2002. Sedimentary Phosphorites – An Example: Phosphoria Formation, Southeastern Idaho, U.S.A. *Rev. Mineral. Geochemistry* 48, 363–389. <https://doi.org/10.2138/rmg.2002.48.9>
- Krajewski, K.P., 1994. Biological processes and apatite formation in sedimentary environments. *Ecol. Geol. Helvet.* 87, 701–745.
- Küster-Heins, K., Steinmetz, E., De Lange, G.J., Zabel, M., 2010. Phosphorus cycling in marine sediments from the continental margin off Namibia. *Mar. Geol.* 274, 95–106. <https://doi.org/10.1016/j.margeo.2010.03.008>
- Lang, L., Kirsimäe, K., Vahur, S., 2016. Diagenetic fate of bioapatite in linguliform brachiopods: multiple apatite phases in shells of Cambrian lingulate brachiopod *Ungula ingraca* (Eichwald). *Lethaia* 49, 13–27. <https://doi.org/10.1111/let.12127>
- Lang, L., Puura, I., 2013. Phosphatized organic nanostructures in the Cambrian linguloid brachiopod *Ungula inornata* (Mickwitz). *Est. J. Earth Sci.* 62, 121–130. <https://doi.org/10.3176/earth.2013.10>
- Lécuyer, C., Grandjean, P., Barrat, J.A., Nolvak, J., Emig, C., Paris, F., Robardet, M., 1998. $\delta^{18}\text{O}$ and REE contents of phosphatic brachiopods: A comparison between modern and lower Paleozoic populations. *Geochim. Cosmochim. Acta* 62, 2429–2436. [https://doi.org/10.1016/S0016-7037\(98\)00170-7](https://doi.org/10.1016/S0016-7037(98)00170-7)
- Lécuyer, C., Reynard, B., Grandjean, P., 2004a. Rare earth element evolution of Phanerozoic seawater recorded in biogenic apatites. *Chem. Geol.* 204, 63–102. <https://doi.org/10.1016/j.chemgeo.2003.11.003>
- Lepland, A., Joosu, L., Kirsimäe, K., Prave, A.R., Romashkin, A.E., Črne, A.E., Martin, A.P., Fallick, A.E., Somelar, P., Üpraus, K., Mänd, K., Roberts, N.M.W., Van Zuilen, M.A., Wirth, R., Schreiber, A., 2014. Potential influence of sulphur bacteria on Palaeoproterozoic phosphogenesis. *Nat. Geosci.* 7, 20–24. <https://doi.org/10.1038/ngeo2005>
- Lin, Z., Sun, X., Peckmann, J., Lu, Y., Xu, L., Strauss, H., Zhou, H., Gong, J., Lu, H., Teichert, B.M.A., 2016. How sulfate-driven anaerobic oxidation of methane affects the sulfur isotopic composition of pyrite: A SIMS study from the South China Sea. *Chem. Geol.* 440, 26–41. <https://doi.org/10.1016/j.chemgeo.2016.07.007>
- Long, K.R., Van Gosen, B.S., Foley, N.K., Cordier, D., 2012. The Principal Rare Earth Elements Deposits of the United States: A Summary of Domestic Deposits and a Global Perspective, in: *Non-Renewable Resource Issues*. Springer Netherlands, Dordrecht, pp. 131–155. https://doi.org/10.1007/978-90-481-8679-2_7
- Lumiste, K., Lang, L., Paiste, P., Lepland, A., Kirsimäe, K., 2021a. Heterogeneous REE+Y distribution in Early Paleozoic shelly phosphorites: implications for enrichment mechanisms Manuscript submitted to *Chemical Geology*.
- Lumiste, K., Mänd, K., Bailey, J., Stüeken, E.E., Paiste, K., Lang, L., Sepp, H., Lepland, A., Kirsimäe, K., 2021b. Constraining the conditions of phosphogenesis: Stable isotope and trace element systematics of Recent Namibian phosphatic sediments. *Geochim. Cosmochim. Acta* 302, 141–159. <https://doi.org/10.1016/j.gca.2021.03.022>

- Lumiste, K., Mänd, K., Kirsimäe, K., Bailey, J., Paiste, P., Lang, L., Lepland, A., 2019. REE + Y uptake and diagenesis in Recent sedimentary apatites. *Chem. Geol.* 525, 268–281. <https://doi.org/10.1016/j.chemgeo.2019.07.034>
- Mänd, K., Kirsimäe, K., Lepland, A., Crosby, C.H., Bailey, J. V., Konhauser, K.O., Wirth, R., Schreiber, A., Lumiste, K., 2018. Authigenesis of biomorphic apatite particles from Benguela upwelling zone sediments off Namibia: The role of organic matter in sedimentary apatite nucleation and growth. *Geobiology* 1–19. <https://doi.org/10.1111/gbi.12309>
- Martin, J.-M., Høgdahl, O., Philippot, J.C., 1976. Rare earth element supply to the Ocean. *J. Geophys. Res.* 81, 3119–3124. <https://doi.org/10.1029/jc081i018p03119>
- Masuda, A., Ikeuchi, Y., 1979. Lanthanide tetrad effect observed in marine environment. *Geochem. J.* 13, 19–22. <https://doi.org/10.2343/geochemj.13.19>
- McArthur, J.M., 1985. Francolite geochemistry—compositional controls during formation, diagenesis, metamorphism and weathering. *Geochim. Cosmochim. Acta* 49, 23–35. [https://doi.org/10.1016/0016-7037\(85\)90188-7](https://doi.org/10.1016/0016-7037(85)90188-7)
- McArthur, J.M., Walsh, J.N., 1984. Rare-earth geochemistry of phosphorites. *Chem. Geol.* 47, 191–220. [https://doi.org/10.1016/0009-2541\(84\)90126-8](https://doi.org/10.1016/0009-2541(84)90126-8)
- Meisel, S., Emeis, K.C., Struck, U., Kristen, I., 2011a. Nutrient regime and upwelling in the northern Benguela since the middle Holocene in a global context – A multi-proxy approach. *Foss. Rec.* 14, 171–193. <https://doi.org/10.1002/mmng.201100006>
- Meisel, S., Struck, U., Emeis, K.C., 2011b. Nutrient dynamics and oceanographic features in the central Namibian upwelling region as reflected in $\delta^{15}\text{N}$ -signals of suspended matter and surface sediments. *Foss. Rec.* 14, 153–169. <https://doi.org/10.1002/mmng.201100005>
- Michard, A., 1989. Rare earth element systematics in hydrothermal fluids. *Geochim. Cosmochim. Acta* 53, 745–750. [https://doi.org/10.1016/0016-7037\(89\)90017-3](https://doi.org/10.1016/0016-7037(89)90017-3)
- Miklasz, K.A., Denny, M.W., 2010. Diatom sinking speeds: Improved predictions and insight from a modified Stoke’s law. *Limnol. Oceanogr.* 55, 2513–2525. <https://doi.org/10.4319/lo.2010.55.6.2513>
- Minami, M., Masuda, A., Takahashi, K., Adachi, M., Shimizu, H., 1998. Y-Ho fractionation and lanthanide tetrad effect observed in cherts. *Geochem. J.* 32, 405–419. <https://doi.org/10.2343/geochemj.32.405>
- Mollenhauer, G., Inthorn, M., Vogt, T., Zabel, M., Sinninghe Damsté, J.S., Eglinton, T.I., 2007. Aging of marine organic matter during cross-shelf lateral transport in the Benguela upwelling system revealed by compound-specific radiocarbon dating. *Geochemistry, Geophys. Geosystems* 8. <https://doi.org/10.1029/2007GC001603>
- Morford, J.L., Emerson, S.R., Breckel, E.J., Kim, S.H., 2005. Diagenesis of oxyanions (V, U, Re, and Mo) in pore waters and sediments from a continental margin. *Geochim. Cosmochim. Acta* 69, 5021–5032. <https://doi.org/10.1016/j.gca.2005.05.015>
- Nathan, Y., Sass, E., 1981. Stability relations of apatites and calcium carbonates. *Chem. Geol.* 34, 103–111. [https://doi.org/https://doi.org/10.1016/0009-2541\(81\)90075-9](https://doi.org/https://doi.org/10.1016/0009-2541(81)90075-9)
- Noffke, A., Hensen, C., Sommer, S., Scholz, F., Bohlen, L., Mosch, T., Graco, M., Wallmann, K., 2012. Benthic iron and phosphorus fluxes across the Peruvian oxygen minimum zone. *Limnol. Oceanogr.* 57, 851–867. <https://doi.org/10.4319/lo.2012.57.3.0851>
- Nozaki, Y., Zhang, J., Amakawa, H., 1997. The fractionation between Y and Ho in the marine environment. *Earth Planet. Sci. Lett.* 148, 329–340. [https://doi.org/10.1016/s0012-821x\(97\)00034-4](https://doi.org/10.1016/s0012-821x(97)00034-4)

- O'Brien, G.W., Veeh, H.H., 1980. Holocene phosphorite on the East Australian continental margin. *Nature* 288, 690–692. <https://doi.org/10.1038/288690a0>
- Ohr, M., Halliday, A.N., Peacor, D.R., 1994. Mobility and fractionation of rare earth elements in argillaceous sediments: Implications for dating diagenesis and low-grade metamorphism. *Geochim. Cosmochim. Acta* 58, 289–312. [https://doi.org/10.1016/0016-7037\(94\)90465-0](https://doi.org/10.1016/0016-7037(94)90465-0)
- Osborne, A.H., Hathorne, E.C., Schijf, J., Plancherel, Y., Böning, P., Frank, M., 2017. The potential of sedimentary foraminiferal rare earth element patterns to trace water masses in the past. *Geochemistry, Geophys. Geosystems* 18, 1550–1568. <https://doi.org/10.1002/2016GC006782>
- Pan, Y., Fleet, M.E., 2002. Compositions of the Apatite-Group Minerals: Substitution Mechanisms and Controlling Factors. *Rev. Mineral. Geochemistry* 48, 13–49. <https://doi.org/10.2138/rmg.2002.48.2>
- Parrish, J.T., Ziegler, A.M., Scotese, C.R., Humphreys, R.G., Kirschvink, J.L., Cook, P.J., Shergold, J.H., 1986. *Phosphate deposits of the World, Volume 1, Proterozoic and Cambrian Phosphorites*.
- Paytan, A., Kastner, M., Campbell, D., Thiemens, M.H., 1998. Sulfur isotopic composition of Cenozoic seawater sulfate. *Science* (80-.). 282, 1459–1462. <https://doi.org/10.1126/science.282.5393.1459>
- Peketi, A., Mazumdar, A., Joshi, R.K., Patil, D.J., Srinivas, P.L., Dayal, A.M., 2012. Tracing the Paleo sulfate-methane transition zones and H₂S seepage events in marine sediments: An application of C-S-Mo systematics. *Geochemistry, Geophys. Geosystems* 13, 1–11. <https://doi.org/10.1029/2012GC004288>
- Pellerin, A., Antler, G., Røy, H., Findlay, A., Beulig, F., Scholze, C., Turchyn, A. V., Jørgensen, B.B., 2018. The sulfur cycle below the sulfate-methane transition of marine sediments. *Geochim. Cosmochim. Acta* 239, 74–89. <https://doi.org/10.1016/j.gca.2018.07.027>
- Piper, D.Z., Bau, M., 2013. Normalized Rare Earth Elements in Water, Sediments, and Wine: Identifying Sources and Environmental Redox Conditions. *Am. J. Anal. Chem.* 04, 69–83. <https://doi.org/10.4236/ajac.2013.410A1009>
- Price, F.T., Shieh, Y.N., 1979. Fractionation of sulfur isotopes during laboratory synthesis of pyrite at low temperatures. *Chem. Geol.* 27, 245–253. [https://doi.org/10.1016/0009-2541\(79\)90042-1](https://doi.org/10.1016/0009-2541(79)90042-1)
- Pufahl, P.K., Grimm, K.A., 2003. Coated phosphate grains: Proxy for physical, chemical, and ecological changes in seawater. *Geology* 31, 801–804. <https://doi.org/10.1130/G19658.1>
- Pufahl, P.K., Groat, L.A., 2017. Sedimentary and igneous phosphate deposits: Formation and exploration: An invited paper. *Econ. Geol.* 112, 483–516. <https://doi.org/10.2113/econgeo.112.3.483>
- Raudsep, R., 1997. Phosphorite, in: Raukas, A., Teedumäe, A. (Eds.), *Geology and Mineral Resources of Estonia*. Estonian Academy Publishers, Tallinn, pp. 331–336.
- Reynard, B., Lécuyer, C., Grandjean, P., 1999. Crystal-chemical controls on rare-earth element concentrations in fossil biogenic apatites and implications for paleoenvironmental reconstructions. *Chem. Geol.* 155, 233–241. [https://doi.org/10.1016/S0009-2541\(98\)00169-7](https://doi.org/10.1016/S0009-2541(98)00169-7)
- Ross, J., Gao, L., Meouch, O., Anthony, E., Sutarwala, D., Mamo, H., Omelon, S., 2017. Carbonate apatite precipitation from synthetic municipal wastewater. *Minerals* 7. <https://doi.org/10.3390/min7080129>

- Ruttenberg, K.C., Berner, R.A., 1993. Authigenic apatite formation and burial in sediments from non-upwelling, continental margin environments. *Geochim. Cosmochim. Acta* 57, 991–1007. [https://doi.org/10.1016/0016-7037\(93\)90035-U](https://doi.org/10.1016/0016-7037(93)90035-U)
- Schenau, S.J., Slomp, C.P., De Lange, G.J., 2000. Phosphogenesis and active phosphorite formation in sediments from the Arabian Sea oxygen minimum zone. *Mar. Geol.* 169, 1–20. [https://doi.org/10.1016/S0025-3227\(00\)00083-9](https://doi.org/10.1016/S0025-3227(00)00083-9)
- Schöllhorn, I., Houben, A., Gertsch, B., Adatte, T., Alexey, U., de Kaenel, E., Spangenberg, J.E., Janssen, N., Schwennicke, T., Föllmi, K.B., 2020a. Enhanced upwelling and phosphorite formation in the northeastern Pacific during the late Oligocene: Depositional mechanisms, environmental conditions, and the impact of glacio-eustasy. *Bull. Geol. Soc. Am.* 132, 687–709. <https://doi.org/10.1130/B32061.1>
- Schulz, H., Brinkhoff, T., Ferdelman, T., Hernandez Marine, M., Teske, A., Jorgensen, B.B., 1999. Dense Populations of a Giant Sulfur Bacterium in Namibian Shelf Sediments. *Science* (80-.). 284, 493–495. <https://doi.org/10.1126/science.284.5413.493>
- Schulz, H., Schulz, H.N., 2005. Large Sulfur Bacteria and the Formation of Phosphorite. *Science* (80-.). 307, 416–418. <https://doi.org/10.1126/science.1103096>
- Shields, G., Stille, P., 2001. Diagenetic constraints on the use of cerium anomalies as palaeoseawater redox proxies: An isotopic and REE study of Cambrian phosphorites. *Chem. Geol.* 175, 29–48. [https://doi.org/10.1016/S0009-2541\(00\)00362-4](https://doi.org/10.1016/S0009-2541(00)00362-4)
- Shields, G., Webb, G.E., 2004. Has the REE composition of seawater changed over geological time? *Chem. Geol.* 204, 103–107. <https://doi.org/10.1016/j.chemgeo.2003.09.010>
- Shields, G.A., Stille, P., Brasier, M.D., 2000. Isotopic Records Across Two Phosphorite Giant Episodes Compared: the Precambrian-Cambrian and the Late Cretaceous-Recent. *Mar. Authigenes. From Glob. to Microb.* 103–115. <https://doi.org/10.2110/pec.00.66.0103>
- Sholkovitz, E.R., Elderfield, H., Szymczak, R., Casey, K., 1999. Island weathering: River sources of rare earth elements to the Western Pacific Ocean. *Mar. Chem.* 68, 39–57. [https://doi.org/10.1016/S0304-4203\(99\)00064-X](https://doi.org/10.1016/S0304-4203(99)00064-X)
- Sim, M.S., Bosak, T., Ono, S., 2011. Large Sulfur Isotope Fractionation Does Not Require Disproportionation. *Science* (80-.). 333, 74–77. <https://doi.org/10.1126/science.1205103>
- Soares, G.G., Van Kranendonk, M.J., Belousova, E., Thomson, S., 2019. Phosphogenesis in the immediate aftermath of the Great Oxidation Event: Evidence from the Turee Creek Group, Western Australia. *Precambrian Res.* 320, 193–212. <https://doi.org/10.1016/j.precamres.2018.10.017>
- Soesoo, A., Vind, J., Hade, S., 2020. Uranium and Thorium Resources of Estonia. *Minerals* 10, 798. <https://doi.org/10.3390/min10090798>
- Somelar, P., Kirsimäe, K., Hints, R., Kirs, J., 2010. Illitization of early paleozoic k-bentonites in the baltic basin: Decoupling of burial- and fluid-driven processes. *Clays Clay Miner.* 58, 388–398. <https://doi.org/10.1346/CCMN.2010.0580309>
- Song, Y., Hahn, H.H., Hoffmann, E., 2002. The Effect of Carbonate on the Precipitation of Calcium Phosphate. *Environ. Technol.* 23, 207–215. <https://doi.org/10.1080/09593332508618427>
- Soyol-Erdene, T.O., Huh, Y., 2013. Rare earth element cycling in the pore waters of the Bering Sea Slope (IODP Exp. 323). *Chem. Geol.* 358, 75–89. <https://doi.org/10.1016/j.chemgeo.2013.08.047>

- Sturesson, U., Popov, L.E., Holmer, L.E., Bassett, M.G., Felitsyn, S., Belyatsky, B., 2005. Neodymium isotopic composition of Cambrian-Ordovician biogenic apatite in the Baltoscandian Basin: Implications for palaeogeographical evolution and patterns of biodiversity. *Geol. Mag.* 142, 419–439. <https://doi.org/10.1017/S0016756805000877>
- Takahashi, Y., Hayasaka, Y., Morita, K., Kashiwabara, T., Nakada, R., Marcus, M.A., Kato, K., Tanaka, K., Shimizu, H., 2015. Transfer of rare earth elements (REE) from manganese oxides to phosphates during early diagenesis in pelagic sediments inferred from REE patterns, X-ray absorption spectroscopy, and chemical leaching method. *Geochem. J.* 49, 653–674. <https://doi.org/10.2343/geochemj.2.0393>
- Taylor, S.R., McLennan, S.M., 1985. *The Continental Crust: Its Composition and Evolution. An Examination of the Geochemical Record Preserved in Sedimentary Rocks. Cont. Crust Its Compos. Evol. An Exam. Geochemical Rec. Preserv. Sediment. Rocks.* <https://doi.org/10.1017/S0016756800032167>
- Torsvik, T.H., Voo, R. Van Der, Preeden, U., Mac, C., Steinberger, B., Doubrovine, P. V., Hinsbergen, D.J.J. Van, Domeier, M., Gaina, C., Tohver, E., Meert, J.G., Mccausland, P.J.A., Cocks, L.R.M., 2012. Earth-Science Reviews Phanerozoic polar wander , palaeogeography and dynamics. *Earth Sci. Rev.* 114, 325–368. <https://doi.org/10.1016/j.earscirev.2012.06.007>
- Tostevin, R., Shields, G.A., Tarbuck, G.M., He, T., Clarkson, M.O., Wood, R.A., 2016. Effective use of cerium anomalies as a redox proxy in carbonate-dominated marine settings. *Chem. Geol.* 438, 146–162. <https://doi.org/10.1016/j.chemgeo.2016.06.027>
- Tribouillard, N., Algeo, T.J., Baudin, F., Riboulleau, A., 2012. Analysis of marine environmental conditions based on molybdenum-uranium covariation-Applications to Mesozoic paleoceanography. *Chem. Geol.* 324–325, 46–58. <https://doi.org/10.1016/j.chemgeo.2011.09.009>
- Tribouillard, N., Algeo, T.J., Lyons, T., Riboulleau, A., 2006. Trace metals as paleoredox and paleoproductivity proxies: An update. *Chem. Geol.* 232, 12–32. <https://doi.org/10.1016/j.chemgeo.2006.02.012>
- Trotter, J.A., Barnes, C.R., McCracken, A.D., 2016. Rare earth elements in conodont apatite: Seawater or pore-water signatures? *Palaeogeogr. Palaeoclimatol. Palaeoecol.* 462, 92–100. <https://doi.org/10.1016/j.palaeo.2016.09.007>
- Trueman, C.N., 2013. Chemical taphonomy of biomineralized tissues. *Palaeontology* 56, 475–486. <https://doi.org/10.1111/pala.12041>
- Tyrrell T., 1999. The relative influences of nitrogen and phosphorus on oceanic primary production. *Nature* 400, 525–531.
- Wallin, B., 1989. Origin of the Lower Cambrian phosphatic bed at Vassbo, Sweden. *Terra Nov.* 1, 274–279. <https://doi.org/10.1111/j.1365-3121.1989.tb00369.x>
- Wang, Z.L., Yamada, M., 2007. Geochemistry of dissolved rare earth elements in the Equatorial Pacific Ocean. *Environ. Geol.* 52, 779–787. <https://doi.org/10.1007/s00254-006-0515-7>
- Wanty, R.B., Goldhaber, M.B., 1992. Thermodynamics and kinetics of reactions involving vanadium in natural systems: Accumulation of vanadium in sedimentary rocks. *Geochim. Cosmochim. Acta* 56, 1471–1483. [https://doi.org/10.1016/0016-7037\(92\)90217-7](https://doi.org/10.1016/0016-7037(92)90217-7)
- Watkins, R.T., Nathan, Y., Bremner, J.M., 1995. Rare earth elements in phosphorite and associated sediment from the Namibian and South African continental shelves. *Mar. Geol.* 129, 111–128. [https://doi.org/10.1016/0025-3227\(95\)00107-7](https://doi.org/10.1016/0025-3227(95)00107-7)

- Williams, A., Cusack, M., 1999. Evolution of a rhythmic lamination in the organo-phosphatic shells of brachiopods. *J. Struct. Biol.* 126, 227–240. <https://doi.org/10.1006/jsbi.1999.4117>
- Wright, J., Der, H.H., Iam, W.I., Er, H.O., Geology, Q., Trom, L., 1987. Paleoredox variations in ancient oceans recorded by rare earth elements in fossil apatite 5.
- Wu, F., Owens, J.D., Tang, L., Dong, Y., Huang, F., 2019. Vanadium isotopic fractionation during the formation of marine ferromanganese crusts and nodules. *Geochim. Cosmochim. Acta.* <https://doi.org/10.1016/j.gca.2019.09.007>
- Zhao, L., Chen, Z.Q., Algeo, T.J., Chen, J., Chen, Y., Tong, J., Gao, S., Zhou, L., Hu, Z., Liu, Y., 2013. Rare-earth element patterns in conodont albid crowns: Evidence for massive inputs of volcanic ash during the latest Permian biocrisis? *Glob. Planet. Change* 105, 135–151. <https://doi.org/10.1016/j.gloplacha.2012.09.001>
- Zhu, B., Jiang, S.Y., Yang, J.H., Pi, D., Ling, H.F., Chen, Y.Q., 2014. Rare earth element and SrNd isotope geochemistry of phosphate nodules from the lower Cambrian Niutitang Formation, NW Hunan Province, South China. *Palaeogeogr. Palaeoclimatol. Palaeoecol.* 398, 132–143. <https://doi.org/10.1016/j.palaeo.2013.10.002>
- Zoss, R., Medina Ferrer, F., Flood, B.E., Jones, D.S., Louw, D.C., Bailey, J., 2018. Microbial communities associated with phosphogenic sediments and phosphoclast-associated DNA of the Benguela upwelling system. *Geobiology* 17, 76–90. <https://doi.org/10.1111/gbi.12318>

SUMMARY IN ESTONIAN

Fosfogenees ja haruldaste muldmetallide diogenees tänapäevastes ja Paleosoilistes fosforiitides

Fosfor on eluslooduse jaoks kandva tähtsusega keemiline element, kuuludes DNA, RNA, ATP ja paljude teiste biomolekulide struktuuri. Samuti on fosfor primaarproduktiooni kontrolliv toitaine. Kuigi nii fosforiringet kui ka selle erinevaid etappe on läbi aastakümnete põhjalikult uuritud, on fosfori sidumine settesse ehk autigeensete fosforit sisaldavate mineraalide teke siiani paljuski ebaselge. See protsess, fosfogenees, toimub mitmete erinevate füüsikaliste, bioloogiliste ja (geo)keemiliste protsesside koosmõjul. Tänapäeval toimub fosfogenees peamiselt passiivsete mandrilavade rannikumeredes, kus süvavee kerke hoovustega transporditakse šelfile suures koguses lämmastikku ja fosforit. Toitainete küllus põhjustab nendes piirkondades autotroofide vohamise ning ulatusliku orgaaniliste setendite akumulierumise. Šelfil kuhjunud orgaanilise ainese lagundamiseks kasutavad heterotroofid ära sette pooriruumis, aga ka veesamba alumises osas sisalduva hapniku, nitraadi ning sulfaadi, põhjustades setetes suboksiliste-anoksiliste keskkonnatingimuste ja teravate, ajas muutuvate, redokskliinide tekkimise. Selline muutlik redokskeskond on sobilikuks elupaigaks väävlit oksüdeerivatele bakteritele (nt. *Thiomargarita namibiensis*). Need kemolitotroofsed bakterid saavad eluks vajalikku energiat peamiselt sulfiidi oksüdeerimise teel, kasutades oksüdandina hapnikku või nitraati. Et aga setete redokstingimused on ajas kiiresti muutuvad, siis on nendel bakteritel evolutsioneerunud alternatiivne metabolismiprotsess. Hapnikurikkas keskkonnas akumuleerivad väävlibakterid pooriveest fosfaati ja nitraati ning talletavad seda raku-siseselt. Redokskeskonna muutumisel anoksiliseks ammutavad bakterid energiat talletatud varudest, salvestatud polüfosfaadi lagundamisel fosfaadiks. Sellise metabolismi tulemusena vabastavad bakterid lühikeste impulssidena pooriruumi lahustunud fosfaati ja võib tekkida üleküllastus Ca-fosfaadi suhtes, mis käivitab autigeense P-faasi väljasettimise.

Peamine setetes moodustuv fosforit sisaldav mineraal on apatiit— $\text{Ca}_5(\text{PO}_4)_3(\text{OH},\text{F},\text{Cl})$. Setted ja settekivimid, mis sisaldavad vähemalt 9% P_2O_5 , klassifitseeritakse fosforiitideks. Sõltuvalt geneesist saab settelistes fosforiitides esinevate apatiitide hulgas eristada peamiselt kaht tüüpi: (I) biogeenne apatiit, mis koosneb peamiselt fosfaatsetest skeletijäänustest (brahhiopoodid, selgroogsete luud, hambad) ning koproliididest; ja (II) autigeenne apatiit, mis koosneb erineva suurusega mineraalsetest keemiliselt sadestatud fosfaatsetest teradest.

Vanimad teadaolevad fosfaatsed setted tekkisid Paleoproterosoikumis. Esi-mesed suuremahulised fosforiidilasundid, mis pakuvad ka tööstuslikku huvi, ilmuvad geoloogilistes läbilõigetel aga alles Neoproterosoikumis ning intensiiv-seim fosforiitide moodustumine on valdavalt seotud Fanerosoikumiga. Täna-päeval moodustuvad fosforirikad setted peamiselt ookeanide tõusuhoovuste

piirkonnas Namiibia, Peruu ja Tšiili, California rannikutel, Araabia meres ning ka Lääne-Austraalias.

Tulenevalt apatiidi komplekssest kristallstruktuurist on apatiidis võimalikud laiaulatuslikud struktuursed asendused ning Ca, fosfaatioon ja lisaanioonid võivad asenduda paljude teiste ioonide või molekulidega, nagu näiteks Na, Mn, Sr, Ba, Pb, Cd, REE+Y, AsO_4^{3-} , SO_4^{2-} , CO_3^{2-} , SiO_4^{4-} ja VO_4^{3-} .

Nii geokeemilisest kui ka maavaralisest aspektist lähtudes on üks olulisemaid asenduvaid elementide rühmasid haruldased muldmetallid ja ütrium (ehk REE+Y). REE+Y gruppi kuulub 15 keemiliselt väga sarnaste omadustega elementi lantaanist luteetsiumini ning nendega geokeemiliselt sarnane ütrium. REE+Y elemendid on tüüpiliselt kolmevalentsed ning nende käitumine geokeemilistes protsessides on tavaliselt ühesugune. Erandiks on Ce, mis on hapnikurikastes tingimustes nelja-valentne, ja Eu, mis on redutseerivas-kõrgetemperatuurilises keskkonnas kahe-valentne. Seepärast näitavad juba väikesed nihked setete ja kivimite REE+Y muustrites ning REE+Y omavahelistes suhetes (nt Ce/Ce*, Y/Ho, La/Sm) infot mineviku veemasside keemiliste keskkondade kohta.

Haruldaste muldmetallide sisaldused tänapäevastes fosforiitides jäävad üldiselt alla mg/kg taseme ja REE+Y seotakse apatiidi struktuuri valdavalt pärast settimist, mere- ja/või pooriveest diagenetiliste protsesside tulemusena. Tugevalt muutunud fosforiitides võivad haruldaste muldmetallide sisaldused küündida kuni $\geq 2\%$ -ni.

Käesolevas doktoritöös uuriti Miotseeni-Holotseeni autigeenseid settelisi fosforiite ja fosfaatseid setteid Namiibia šelfil ning Paleosoilisi Eesti biogeenseid fosforiite. Töö põhieesmärkideks oli selgitada: (I) fosfogeneesiks vajalikud (bio)-geokeemilised tingimused ning (II) haruldaste muldmetallide sidustamise mehhanismid ja diagenetiline ümberjaotumine. Töö fookuses olid REE+Y süsteemaatika Kainosoilistes ja Paleosoilistes fosforiitides, stabiilsete isotoopide ($\delta^{13}\text{C}$ ja $\delta^{34}\text{S}$) ja redoks-tundlike jälgelementide käitumine ning apatiidi nukleerumine kaasaegse fosfogeneesi protsessides.

Käesoleva töö tulemused näitavad, et apatiidi nukleatsiooni ja algsete apatiitsete mikroosakeste kasvu kontrollivad setete pooriruumis biokiled/kompleksed biomolekulid. Apatiidi mikroosakeste kontsentiline tsonaalsus viitab apatiidi tsükli- lisele kasvule, mida võib seostada fosfaadi pulseeriva vabanemisega väävli- bakterites muutuvates redokstingimustes.

Fosfaatsete setete akumuldeerumise maksimum Namiibia šelfi läbilõikes langeb kokku setete Mo ja Re kontsentratsioonide langusega, mis viitab sellele, et pooriruumis domineerisid suboksilised tingimused. Fosfaatidega koos esinev püriit näitab, et lühiajaliselt esinesid apatiidi settimise ajal ka sulfiidsed-anoksilised perioodid. Selline redoks-dünaamika viitab varem eeldatud mehhanismile, kus (sub)oksiliste tingimuste ajal väävlibakterid akumuldeerivad fosfaati ning lühiajaliste sulfiidsete episoodide ajal seotud fosfor vabastatakse pooriruumi, sobivatel nukleatsioonipindadel toimub aga apatiidi sadenemine. Samas viitavad apatiiti seotud sulfaadi $\delta^{34}\text{S}$ väärtused, et sulfaat pärineb peamiselt mereveest ning vaid osaliselt bakterite poolt settes oksüdeeritud sulfiidist. Seda järeldust toetavad ka apatiiditerade keskosadest mõõdetud Ce/Ce* ja Y/Ho suhted, mis on sarnased tüüpilise merevee väärtustega. Kokkuvõtvalt võib väita, et fosfogeneesi levikut

nii settes kui šelfil kontrollivad (I) domineerivalt suboksiline keskkond, koos (II) lühiajaliselt vahelduvate sulfiidsete tingimustega, ning (III) apatiidi nukleerumiseks sobilike orgaaniliste substraatide olemasolu.

REE+Y sisaldused ning nende omavahelised suhted Namiibia fosforiitides ja fosfaatsetes setetes on süstemaatiliselt erinevad ning sõltuvad sette diagenetilisest ning sedimentoloogilisest ajaloost. Noorimate, konkretsiooniliste apatiiditerade keskmis on säilinud algne merevee signaal, kuid terade äärealad on diagenetiliselt muutunud. REE+Y allikaks on suboksiline või sulfiidne poorivesi ning interaktsioonis apatiitsete teradega on terade välispinnal moodustunud paarikümne mikromeetrilise paksusega REE+Y rikastumistsoonid. Geoloogiliselt vanemates ja korduvalt ümberasetatud apatiiditerades on REE+Y sisaldused rikastumistsoonides olulisel määral kõrgemad kui *in-situ* paiknevates terades, mis viitab pikaajalisele REE+Y sidustamisele apatiiti. Kuigi settelises autigeenses apatiidis salvestunud REE+Y mustreid ja elementsuhteid on laialdaselt kasutatud settimisaegse merevee koostise rekonstrueerimiseks, näitab Namiibia apatiitide laiaulatuslik diagenetiline ümberjaotumine, et settelist apatiiti tuleks pidada kaheldavaks paleo-keskkonna arhiiviks.

Sarnaselt süstemaatilistele erinevustele kaasaegsetes Namiibia fosfaatsetes setetes, esineb ka Paleosoilistes Eesti biogeensetes fosforiitides REE+Y sisaldustes suuri erinevusi nii leiukohtade vahel kui fosfaatsete kodade siseselt. Võrreldes retsensente käsijalgsetega, mille REE+Y sisaldused on väga madalad (tüüpiliselt alla 1 mg/kg), on Eesti biogeense fosforiidi kojapoolmed *post-mortem* rikastunud REE+Y suhtes mitu suurusjärku ning REEde summaarne sisaldus küündib üle 2000 mg/kg. Tähelepanuväärselt on REE+Y jaotumine kojasiseselt erinev. Fosforiiti moodustavate käsijalgsete kojapoolmete sisestruktuur koosneb vahelduvatest kompaktsetest ja poorsetest apatiitsetest kihtidest. Neist esimene koosneb peamiselt käsijalgsete elu ajal sekreteeritud nanomeeterskaalas kristallidega skeletapatiidist, mida on hilisem diagenees arvatavasti väga vähesel määral muutnud. Poorsed vahekihid, mis looma eluajal koosnesid orgaanikaapatiidi võrgustikust, koosnevad nüüdseks aga peamiselt autigeensest apatiidist. REE+Y sisaldused kompaktsetes kihtides on märgatavalt kõrgemad kui poorsetes kihtides, mis tuleneb arvatavasti esimeste suuremast eripinnast. Sarnaselt Namiibia apatiidiga on kõige enam rikastunud kojapoolmete äärealad, olenemata apatiidi geneetilisest tüübist. Erinevalt Namiibia apatiidist, kus apatiitsete terade kõrge REE+Y sisaldusega tsoonide ja terade keskosade REE+Y mustrid on erinevad, kandes vastavalt diagenetilisest poorivee ja merevee signaali, siis Eesti biogeense fosforiidi REE+Y mustrid on kojapoolme erinevate osade vahel sarnase diagenetilisest päritoluga, viidates sellele, et diageneesi käigus saavutati pooriruumi ja apatiidi vahel (kvaasi-)tasakaal. Sellele viitab ka asjaolu, et sama leiukoha erinevate kodade REE+Y mustrid ning sisaldused on väga sarnased. Samal ajal on erinevate, tihtipeale vaid üksteisest paarikümne kilomeetri kaugusel paiknevate leiukohtade kodade REE+Y kontsentratsioonid üksteisest enam kui kümme korda erinevad. Selline erinevus on tõenäoliselt seotud algse settekeskkonnaga. Tänapäevastele fosfogeneesi piirkondadele, mida iseloomustavad (süva-)tõusuhoovused ning kõrge primaarproduksioon, nagu näiteks kaasaegsele Namiibia

šelfile, on iseloomulikud dünaamilised redokstingimused ehk *poikiloxia*. Nendes tingimustes kontrollib REE+Y sisaldusi poorivees redokskeskond, mõjutades nii REE+Y sissekannet ja/või pooriruumi vabastamist. Eesti fosforiidi REE+Y sisalduste variatsiooni võis põhjustada Namiibia rannikule sarnane dünaamiline varajase diageneesi redokskeskond, misjuhul kõrged kontsentratsioonid on seotud domineerivate anoksiliste tingimustega ning madalad kontsentratsioonid on iseloomulikud aladele, kus domineerisid (sub)oksilised tingimused.

ACKNOWLEDGEMENTS

I wish to express my sincerest gratitude to Aivo Lepland, Liisa Lang and Kalle Kirsimäe, without whom completing this thesis would not have been possible. I would also like to thank all my co-authors for their contribution throughout the years. I am grateful for the support from all of my colleges at the Department of Geology in Tartu. Furthermore, I would like to thank the Regional Graduate Network in Oceanography Discovery and the captain and crew of R/V Mirabilis for access to the Namibian phosphorite coring sites. Financial support from Estonian Research Council (PUT696, PRG447, RESTA19) is gratefully acknowledged.

Lastly, I would like to thank my wife Liina, who has been my biggest supporter throughout this journey.

PUBLICATIONS

CURRICULUM VITAE

Name: Kaarel Lumiste
Date of birth: 05.07.1992
Address: Department of Geology, University of Tartu,
Ravila 14A, 50411 Tartu, Estonia
Contact: +372 53499049
E-mail: kaarel.lumiste@ut.ee

Education

2017–... University of Tartu, Department of Geology, PhD student in geology
2015–2017 University of Tartu, MSc in geology
2011–2014 University of Tartu, BSc in geology

Professional employment

2021–... Geologist, The Geological Survey of Estonia
2017–... Junior Research Fellow of Geology, University of Tartu,
Department of Geology

Field of research:

Geochemistry, Geobiology, REE+Y, Phosphogenesis

Publications

1. Mänd, K., Kirsimäe, K., Lepland, A., Crosby, C.H., Bailey, J. V., Konhauser, K.O., Wirth, R., Schreiber, A., **Lumiste, K.**, 2018. Authigenesis of biomorphic apatite particles from Benguela upwelling zone sediments off Namibia: The role of organic matter in sedimentary apatite nucleation and growth. *Geobiology* 1–19.
2. **Lumiste, K.**, Mänd, K., Kirsimäe, K., Bailey, J., Paiste, P., Lang, L., Lepland, A., 2019. REE + Y uptake and diagenesis in Recent sedimentary apatites. *Chem. Geol.* 525, 268–281.
3. **Lumiste, K.**, Mänd, K., Bailey, J., Stüeken, E.E., Paiste, K., Lang, L., Sepp, H., Lepland, A., Kirsimäe, K., 2021b. Constraining the conditions of phosphogenesis: Stable isotope and trace element systematics of Recent Namibian phosphatic sediments. *Geochim. Cosmochim. Acta* 302, 141–159.
4. Mänd, K., Lalonde, S. V., Paiste, K., Thoby, M., **Lumiste, K.**, Robbins, L.J., Kreitsmann, T., Romashkin, A.E., Kirsimäe, K., Lepland, A., Konhauser, K.O., 2021. Iron isotopes reveal a benthic iron shuttle in the palaeoproterozoic zaonega formation: Basinal restriction, euxinia, and the effect on global palaeoredox proxies. *Minerals* 11.
5. **Lumiste, K.**, Lang, L., Paiste, P., Lepland, A., Kirsimäe, K., 2021. Heterogeneous REE+Y distribution in Early Paleozoic shelly phosphorites: implications for enrichment mechanisms Manuscript submitted to *Chemical Geology*.

ELULOOKIRJELDUS

Nimi: Kaarel Lumiste
Sünniaeg: 05.07.1992
Aadress: Geoloogia osakond, Tartu Ülikool,
Ravila 14A, 50411 Tartu, Eesti
Kontakt: Tel. +372 53499049
E-post: kaarel.lumiste@ut.ee

Haridus

2017–... Tartu Ülikool, geoloogia osakond, geoloogia doktorant
2015–2017 Tartu Ülikool, MSc geoloogia
2011–2014 Tartu Ülikool, BSc geoloogia

Teenistuskäik

2021–... Eesti Geoloogiateenistus, geoloog
2017– Tartu Ülikool, Geoloogia osakond, geoloogia nooremteadur

Teadustöö põhisuunad:

geokeemia, geobioloogia, REE+Y, fosfogenees

Publikatsioonid

1. Mänd, K., Kirsimäe, K., Lepland, A., Crosby, C.H., Bailey, J. V., Konhauser, K.O., Wirth, R., Schreiber, A., **Lumiste, K.**, 2018. Authigenesis of biomorphic apatite particles from Benguela upwelling zone sediments off Namibia: The role of organic matter in sedimentary apatite nucleation and growth. *Geobiology* 1–19.
2. **Lumiste, K.**, Mänd, K., Kirsimäe, K., Bailey, J., Paiste, P., Lang, L., Lepland, A., 2019. REE + Y uptake and diagenesis in Recent sedimentary apatites. *Chem. Geol.* 525, 268–281.
3. **Lumiste, K.**, Mänd, K., Bailey, J., Stüeken, E.E., Paiste, K., Lang, L., Sepp, H., Lepland, A., Kirsimäe, K., 2021b. Constraining the conditions of phosphogenesis: Stable isotope and trace element systematics of Recent Namibian phosphatic sediments. *Geochim. Cosmochim. Acta* 302, 141–159.
4. Mänd, K., Lalonde, S. V., Paiste, K., Thoby, M., **Lumiste, K.**, Robbins, L.J., Kreitsmann, T., Romashkin, A.E., Kirsimäe, K., Lepland, A., Konhauser, K.O., 2021. Iron isotopes reveal a benthic iron shuttle in the palaeoproterozoic zaonega formation: Basinal restriction, euxinia, and the effect on global palaeoredox proxies. *Minerals* 11.
5. **Lumiste, K.**, Lang, L., Paiste, P., Lepland, A., Kirsimäe, K., 2021. Heterogeneous REE+Y distribution in Early Paleozoic shelly phosphorites: implications for enrichment mechanisms Manuscript submitted to *Chemical Geology*.

DISSERTATIONES GEOLOGICAE UNIVERSITATIS TARTUENSIS

1. **Пэп Мянник.** Конодонты в верхнеордовикских и нижнесилурийских отложениях Эстонии. Тарту, 1992, 355 с.
2. **Elvi Tavast.** Fennoskandia kilbi lõunanõlva ja sellega piirnevate alade alus- põhja reljeef. Tartu, 1992, 357 lk.
3. **Kaarel Orviku.** Characterisation and evolution of Estonian seashores. Tartu, 1992, 19 p.
4. **Анатолий Молодьков.** ЭПР-анализ скелетного вещества моллюсков в хроностратиграфических исследованиях позднего кайнозоя. Тарту, 1992, 33 с.
5. **Jaan Lutt.** Late- and postglacial deposits on the Estonian shelf. Tartu, 1993, 31 p.
6. **Reet Karukäpp.** Gotiglatsiaalne morfogenees Skandinaavia mandriliustiku kagusektoris. Tartu, 1997, 181 p.
7. **Argo Jõelett.** Geothermal studies of the Precambrian basement and Phanerozoic sedimentary cover in Estonia and Finland. Tartu, 1998, 125 p.
8. **Jüri Nemliher.** Mineralogy of Phanerozoic skeletal and sedimentary apatites: an XRD study. Tartu, 1999, 134 p.
9. **Kalle Kirsimäe.** Clay mineral diagenesis on the Lower Cambrian “Blue Clay” in the northern part of the Baltic Paleobasin. Tartu, 1999, 113 p.
10. **Jüri Plado.** Gravity and magnetic signatures of meteorite impact structures. Tartu, 2000, 87 p.
11. **Olev Vinn.** Morphogenesis and phylogenetic relationships of Clitambonitidines, Ordovician Brachiopods. Tartu, 2001, 127 p.
12. **Leho Ainsaar.** The middle Caradoc facies and faunal turnover in the late Ordovician Baltoscandian palaeobasin: sedimentological and carbon isotope aspects. Tartu, 2001, 109 p.
13. **Oive Tinn.** Early Ostracode evolution and Palaeoenvironmental application in the Ordovician of Baltoscandia. Tartu, 2002, 145 p.
14. **Maris Rattas.** Subglacial environments in the formation of drumlins — The case of the Saadjärve Drumlin Field, Estonia. Tartu, 2004, 117 p.
15. **Ene Kadastik.** Upper-Pleistocene stratigraphy and deglaciation history in northwestern Estonia. Tartu, 2004, 129 p.
16. **Helje Pärnaste.** Early Ordovician trilobites of suborder Cheirurina in Estonia and NW Russia: systematics, evolution and distribution. Tartu, 2004, 138 p.
17. **Mari-Ann Mõtus.** Silurian (Llandovery-Wenlock) tabulate corals of Baltoscandia: taxonomy, palaeoecology, distribution. Tartu, 2005, 167 p.
18. **Alar Rosentau.** Development of proglacial lakes in Estonia. Tartu, 2006, 114 p.
19. **Evelin Verš.** Development of impact-induced hydrothermal system at Kärdda impact structure. Tartu, 2006, 96 p.

20. **Sigitas Radzevičius.** The genus *Pristiograptus* in wienlock of East Baltic and the Holy Cross Mountains. Tartu, 2007, 133 p.
21. **Andres Marandi.** Natural chemical composition of groundwater as a basis for groundwater management in the Cambrian-Vendian aquifer system in Estonia. Tartu, 2007, 116 p.
22. **Eve Niinemets.** Vegetation and land-use history of the Haanja Heights (SE-Estonia) during the holocene. Tartu, 2008, 146 p.
23. **Kalle-Mart Suuroja.** Geology and lithology of the early palaeozoic marine impact structures Kärddla and Neugrund (Estonia). Tartu, 2008, 234 p.
24. **Rutt Hints.** Early diagenesis of Ordovician and Silurian Bentonites in the Northern Baltic Palaeobasin. Tartu, 2009, 90 p.
25. **Peeter Somelar.** Illitization of K-bentonites in the Baltic Basin. Tartu, 2009, 118 p.
26. **Ulla Preeden.** Remagnetizations in sedimentary rocks of Estonia and shear and fault zone rocks of southern Finland. Tartu, 2009, 121 p.
27. **Kati Tänavsuu-Milkeviciene.** Transgressive to regressive turnaround in the Middle Devonian Baltic Basin. Tartu, 2009, 106 p.
28. **Valle Raidla.** Chemical and isotope evolution of groundwater in the Cambrian-Vendian aquifer system in Estonia. Tartu, 2010, 134 p.
29. **Kadri Sohar.** Quaternary ostracods from Estonia and their application in palaeoenvironmental reconstruction. Tartu, 2010, 140 p.
30. **Kristjan Urtson.** Stepwise melt transport and accumulation: analogue and numerical modelling approach. Tartu, 2011, 83 p.
31. **Marko Kohv.** Landslides in clayey soils of western Estonia. Tartu, 2011, 116 p.
32. **Nele Muttik.** Post-impact alteration of impactites: Ries crater, Germany. Tartu, 2011, 78 p.
33. **Annette Sedman.** Strength and self-cementing properties of oil shale retorting wastes. Tartu, 2013, 82 p.
34. **Arkady Tsyrunnikov.** Complex seismo-acoustic and lithological study of the Lateglacial and postglacial sediments northern Gulf of Riga, eastern branch of the central Baltic Sea. Tartu, 2013, 102 p.
35. **Marge Uppin.** Geological sources and hydrochemistry of fluoride and boron in Silurian-Ordovician aquifer system. Tartu, 2013, 86 p.
36. **Peeter Talviste.** Temporal changes in weak natural and artificial soils – influence on geotechnical characteristics. Tartu, 2014, 204 p.
37. **Katrin Lasberg.** Chronology of the Weichselian Glaciation in the south-eastern sector of the Scandinavian Ice Sheet. Tartu, 2014, 100 p.
38. **Sirle Liivamägi.** Neoproterozoic Baltic paleosol: geology and paleoenvironmental interpretation. Tartu, 2015, 94 p.
39. **Lauri Joosu.** Petrography and the rare earth element composition of apatite in 2 Ga Onega and Pechenga basins, Russia: the environmental settings for phosphogenesis. Tartu, 2015, 139 p.
40. **Liisa Lang.** Baculate shell structure in Early Palaeozoic linguliform brachiopods. Tartu, 2015, 114 p.

41. **Päärn Paiste.** Geopolymeric potential of the Estonian oil shale processing waste. Tartu, 2017, 125 p.
42. **Mikk Gaškov.** Stable isotope and fluid inclusion evidence of multistage fluidal activity in Baltic paleobasin: Silurian carbonate sequence in Kalana, Estonia. Tartu, 2017, 104 p.
43. **Viirika Mastik.** Silurian noncalcified macroscopic algal fossils from the Kalana *Lagerstätte*, Estonia. Tartu, 2018, 91 p.
44. **Kairi Põldsaar.** Soft-sediment deformation and gravity flow structures in the Lower Palaeozoic successions of the Baltic Basin. Tartu, 2019, 105 p.
45. **Timmu Kreitsmann.** Application of carbon isotope and rare earth elements as recorders of environmental conditions in the aftermath of the Paleoproterozoic Lomagundi-Jatuli Event. Tartu, 2020, 163 p.
46. **Triine Nirgi.** Holocene relative shore-level changes and geoarchaeology of the prehistoric sites in western Estonia. Tartu, 2020, 161 p.
47. **Kristjan Leben.** Long-term diagenetic transformation and carbon sequestration potential of Ca-rich oil shale ash waste deposit sediments. Tartu, 2021, 117 p.
48. **Karin Truuver.** Ostracod associations of the ordovician–silurian boundary interval in baltoscandia. Tartu, 2021, 132 p.